Title
Dynamics and Stability of Thermal Flying-height Control Sliders in Hard Disk Drives

Author
Zheng, Jinglin

Publication Date
2012

Peer reviewed|Thesis/dissertation

Dynamics and Stability of Thermal Flying-height Control Sliders in Hard Disk Drives

by

Jinglin Zheng

A dissertation submitted in partial satisfaction of the
requirements of the degree of
Doctor of Philosophy
in
Engineering - Mechanical Engineering
in the
Graduate Division
of the
University of California, Berkeley

Committee in charge:

Professor David B. Bogy, Chair
Professor Tarek I. Zohdi
Professor Jon Wilkening

Spring 2012

Dynamics and Stability of Thermal Flying-height Control Sliders in Hard Disk Drives

Jinglin Zheng

Abstract

Dynamics and Stability of Thermal Flying-height Control Sliders in Hard Disk Drives

by

Jinglin Zheng

Doctor of Philosophy in Engineering - Mechanical Engineering
University of California, Berkeley

Professor David B. Bogy, Chair

As a recent development to further reduce the flying height of a magnetic head in hard disk drives (HDDs) to nanometers, thermal flying-height (TFC) control technology is now widely applied in the HDD industry because it enables consistent read/write spacing, increased storage density and improved HDD reliability. The fast development of TFC technology presents new challenges to head designers because of the complicated structure of a TFC head, the thermo-mechanical-coupling effects and tribology issues arising at nanometer read/write spacing.

A steady-state TFC solver dedicated to obtaining the steady-state flying attitude of a TFC slider is developed in this thesis. This solver uses a finite volume based solver (CML static solver) to solve the generalized Reynolds equation and obtain the pressure and spacing fields in the air bearing and a commercial coupled-field solver (ANSYS) to obtain the stress and strain fields due to internal heating. An iterative procedure is adopted to consider the cooling effect of the air bearing on the heater-induced protrusion. Accuracy of the solver is verified by drive-level magnetic tests on several combinations of air bearing and heater designs.

TFC sliders' performances under different ambient conditions are investigated based on the TFC solver. It is found that the thermal actuation efficiency of a TFC slider increases with altitude because of the weakened cooling and reduced air bearing stiffness at the transducer area at a higher altitude. In addition, a TFC slider maintains a more consistent read/write spacing at different humidity levels, compared with a non-TFC slider, because the thermal actuation is able to compensate part of the pressure loss caused by water condensation. A TFC slider's flying height in air-helium mixtures is shown to be a highly nonlinear function of the fraction of helium in the gas mixture due to the combined effects of the gas mean free path, viscosity and heat conductivity. These results provide general guidelines for heater and ABS designers to reduce a TFC slider's sensitivity to ambient conditions and improve HDD reliability.

A touchdown numerical model for predicting TFC sliders' dynamics at touchdown and over-pushed conditions is developed and implemented based on the CML dynamic simulator. It extends the solution of the time-varying generalized Reynolds equation to near-contact and contact conditions using a statistical multi-asperity approach. Various interfacial forces are considered by use and further development of a sub-boundary lubrication model to capture important tribological effects occurring at touchdown. This model is able to predict a TFC slider's unstable dynamics at the beginning of touchdown, which has been discovered in

many related experimental studies. The effects of different head-disk interface factors are investigated using this numerical model. It is found that the suspension is actively involved in the TFC slider's bouncing vibrations and has a significant influence on the excited second air bearing pitch mode. It is also shown that adhesion force serves as an essential factor in exciting the second air bearing mode whereas other interfacial forces only affect details of the slider's bouncing behaviors. By changing the interfacial properties, namely, the interface roughness and lubricant thickness, the variation of interfacial forces with spacing reduction differs, which leads to very different touchdown patterns. With a rougher interface profile the slider smoothly transfers from a flying stage to a sliding stage. With a smoother interface profile the slider experiences a flying-bouncing-sliding transition. With the smoothest interface the slider goes through a flying-bouncing-surfing-sliding transition.

The touchdown behaviors predicted by the numerical simulator are correlated with experiments conducted on industry-provided head parts with the same ABS and suspension design. Similar touchdown stages and excited modes are also discovered in the experiments. Though experiments showed a slider spectrum with richer frequency components, the modes missed from the numerical simulations are recovered by conducting a harmonic analysis on a full HGA model with air bearing included.

The different touchdown dynamic patterns predicted here result in significant differences in the successful touchdown detection, which is very important for realizing reliable read/write operations, and therefore this work provides guidelines for head disk interface (HDI) optimization. The general approach proposed here is also applicable to studies on the effects of other important HDI factors, such as air bearing geometric features, heater-induced protrusion profiles, and suspension design parameters, and on the slider's touchdown dynamics behaviors, which will assist in obtaining solutions to performance and reliability issues in current hard disk drives.

To my parents, sisters and Qin

Acknowledgements

I would like to express my sincere gratitude to my research advisor, Professor David B. Bogy, for giving me all kinds of freedom and encouragement which made my Ph.D. program a smooth and enjoyable one. Several other professors have contributed graciously their time and wisdom on my behalf, including Professor David J. Steigmann, Professor Tarek I. Zohdi, Professor Oliver O'Reilly, and Professor Jon Wilkening. I also would like to thank the engineers in the ABS/Tribology group in Western Digital where I worked as a summer intern. Dr. Shuyu Zhang, Dr. Wentao Yan, Dr. Yong Hu and Dr. Bill Sun have given me professional advice and support throughout my internships there. It has been a great pleasure to work with my colleagues at CML: Jia-Yang Juang, Du Chen, Liang Pan, Nan Liu, Ning Li, Sripathi Vangipuram Canchi, Rahul Rai, Liping Li, Joanna Bechtel, Shaoming Xiong, Yung-kan Chen, Alejandro Rodriguez, Jia Zhao, Yuliang Liu and Dequan Shi. I want to give special thanks to Brendan Cox and Dolf Mardan for helping me with the computer setups required for the work. I would also like to thank the entity that is the University of California at Berkeley which has exposed me to so many different ideas, cultures, opportunities, and resources. Finally I have to thank my parents, sisters and my husband for their love and support. The work is supported by the Computer Mechanics Laboratory at the University of California, Berkeley and supported in part by the Information Storage Industry Consortium (INSIC).

Contents

List of Figures

List of Tables

Chapter 1

Introduction

1.1 Modern Magnetic Hard Disk Drives

Magnetic hard disk drives (HDD) were first introduced by IBM in 1956 and have become the dominant data storage device since early 1960s. They are now widely used in computers ranging from mainframes to laptops because of the large storage capacity, fast accessing speed, low cost per megabyte and high reliability [1].

The main components in modern hard disk drives are shown in Figure 1.1. A typical hard disk drive includes: a platter which is a flat circular disk and holds the magnetic data, a spindle to hold the platters, a read/write head which magnetizes a local region on the disk and reads data from or writes data to the disk, an actuator arm actuated by a voice coil motor to position the read/write head above the spinning disk, and interfaces through which the hard disk drive communicates with the computer processors.

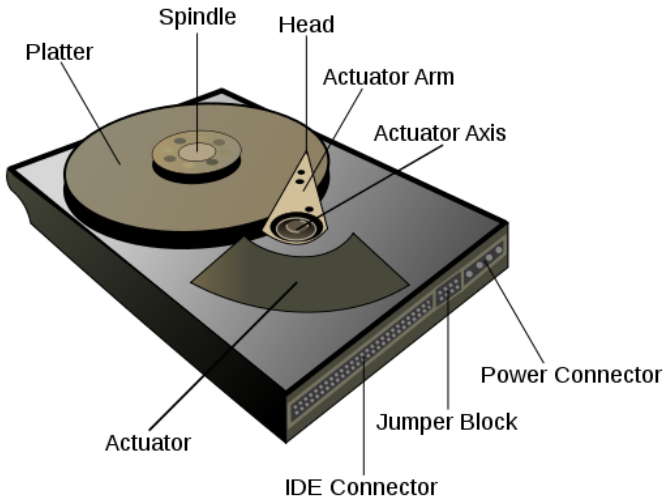

Figure 1.1 Main components of a magnetic hard disk drive (http://en.wikipedia.org/wiki/File:Hard_drive-en.svg)

As shown in Figure 1.2, the areal density of magnetic recording in HDDs has been increasing dramatically over the past decades. Because the increase of areal density requires the magnetic data bits to pack closer to each other, the physical spacing or flying height of the magnetic head has to be reduced accordingly, as shown in Figure 1.3, in order for reliable read/write operations. The physical spacing in current commercial HDDs is below 3 nm.

The magnetic head in modern HDDs is kept only nanometers away from the disks by an ultra-thin gas film which is referred to as air bearing. By carefully designing the pattern at the bottom surface (air bearing surface or ABS) of the air bearing slider bearing all the read/write transducers, a desirable air bearing pressure field is maintained in the

clearance between the head and disk (head disk interface or HDI) which keeps the slider at a preferred attitude for read/write operations.

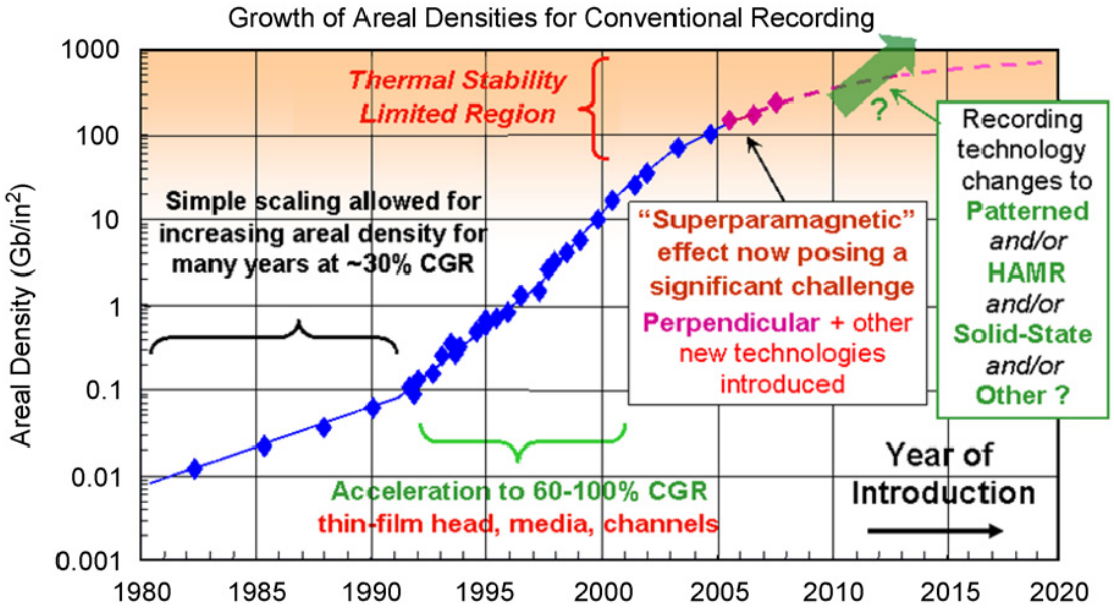

Figure 1.2 The increase of areal density in hard disk drives [2].

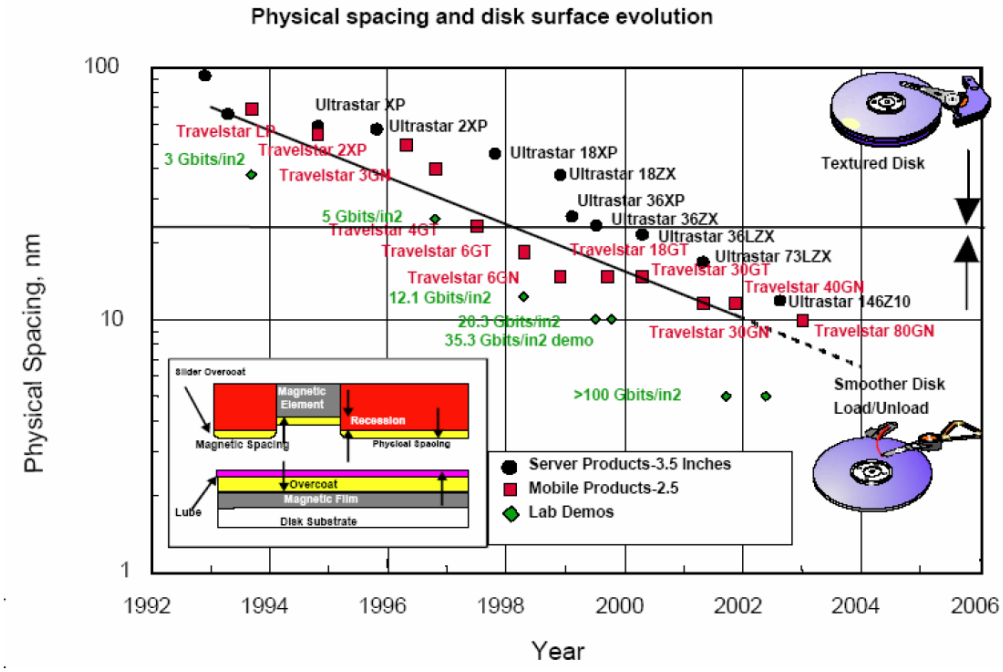

Figure 1.3 The reduction of physical spacing in hard disk drives (http://www.hitachigst.com)

1.2 Thermal flying-height control technology

Thermal flying-height control (TFC) technology is now widely used in state-of-the-art hard disk drives as an effective method to reduce the head-disk spacing and improve

the drive performance and reliability [3]. The TFC concept involves imbedding a separate heater into the read/write head [4, 5], as shown in Figure 1.4. This separate heater is turned on during read/write operations so that a bulge shape protruding toward the recording disk is formed at the read/write transducer area. This localized protrusion can bring the transducers closer to the recording disk by several nanometers, but in the meantime, it modifies the geometry of ABS, resulting in changes in the slider's flying attitude, as shown in Figure 1.5. One advantage of the TFC technology is that the heater is only turned on during read/write operations, thus the slider is flying well above the disk at other times. Even when the heater is on, this highly localized protrusion keeps other parts of the slider far enough from the disk to avoid any destructive head-disk contact. Furthermore, the heater element provides one more degree of freedom to adjust the head-disk spacing. During write operations an additional protrusion is formed locally because of the write current applied to the write element which also causes spacing variations. However, by reducing the TFC heater power a consistent spacing can be achieved even during the write operations [6-10].

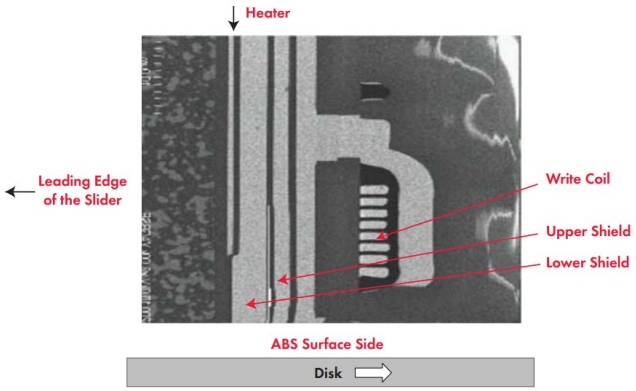

Figure 1.4 Cross-section of a TFC head structure [4].

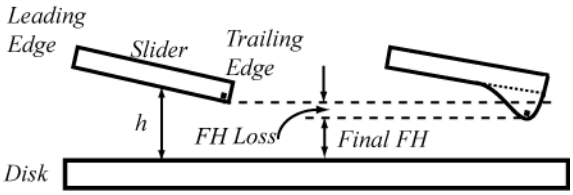

Figure 1.5 The operating principle of a TFC slider. The black square near the trailing edge indicates the location of the read/write transducers. When power is supplied to the heater, which is near the transducers and not shown in the figure, the slider deforms locally near the transducers and the air gap thickness underneath the transducers decreases. The flying height (FH) loss refers to the difference between the initial flying height at the transducer of the undeformed slider and the final flying height at the transducer of the deformed slider. Since the pressure distribution changes with the ABS profile, the slider's deformation also induces its own rotation and translation compared to its undeformed state.

1.3 Motivation and organization of the dissertation

The aim of the research presented here is to develop and apply numerical models to investigate the steady-state and dynamic performance of TFC sliders under heater actuations at flying, touchdown and over-pushed states. The general approach developed

here can be used to conduct parametric studies on various HDI factors to understand the mechanisms working behind the behaviors of a TFC head. The results presented here should be of practical importance for HDD engineers to improve air bearing, heater and interface designs for improved HDD performance and reliability.

The dissertation is organized as follows. Chapter 2 develops a numerical approach for a TFC slider's steady-state flying attitude solution by integrating a finite volume solver for the steady-state generalized Reynolds equation and a coupled-field finite element solver for thermal-stress analysis on the head structure through an iterative procedure. Chapter 3 investigates the performance of a TFC slider under different ambient conditions and in the air-helium mixtures using the steady-state numerical model. Chapter 4 extends the TFC slider dynamics solution from flying to touchdown and over-pushed conditions by modeling the tribological effects at extremely small clearances and continuing solving the air bearing pressure at near-contact and contact conditions. Chapter 5 investigates the effects of various HDI factors, including suspension mass and stiffness, adhesion, friction and electrostatic forces on a TFC slider's touchdown behavior. Chapter 6 explores possible touchdown dynamic patterns that can be achieved with different HDI properties and correlates numerical results with experiments. Chapter 7 gives a final summary and conclusion of the research presented in this dissertation.

Chapter 2

Numerical solution of a TFC slider's steady-state flying attitude

2.1 Introduction

The application of the TFC technology presents new challenges to the numerical solution of a slider's steady-state performance. On the one hand, the deformed air bearing surface results in a different pressure field in the HDI and causes rotations and translations of the slider. On the other hand, the pressure and spacing fields affect the heat dissipation at the air bearing surface and thus have an impact on the ABS deformation. In order to obtain a steady-state solution of a TFC slider, the heat transfer at the air bearing surface has to be characterized and the coupling between the air bearing pressure and the heater-induced protrusion has to be addressed appropriately [11-15].

The first heat transfer model for the head disk interface was proposed by Zhang and Bogy, in which the Navier-Stokes equation was solved using discontinuous boundary conditions to obtain an analytical formula for the heat flux at the air bearing surface [16]. It is shown that heat conduction dominates the heat exchange process wherever the temperature difference between the slider and disk is not zero [16-18]. Thus, the heat conduction formula is applicable to the TFC case. This model was further improved by Chen, Liu and Bogy by inclusion of the boundaries, namely, the slider and the disk, in the calculations of the air molecules' mean free path [19].

The pioneering work of considering the coupling between the flying-attitude solution and the protrusion solution was done by Juang, Chen and Bogy [12], who proposed an iterative procedure between these two solutions. This approach has been proved by experiments to give good predictions of a TFC slider's flying height [13]. Due to the complicated structure of read/write heads, the deformation solution is usually completed in ANSYS, a commercial finite element software which allows input of a complicated 3-D structure consisting of different materials. The air bearing pressure solution is usually done in the CML air bearing program, which uses a finite volume approach and allows input of complicated air bearing surface designs. Therefore, the iterative procedure requires several manual switches between different softwares for convergence, which is a repeated and costly process.

In this chapter, an integrated TFC solver packaged in the form of ANSYS macros is developed to give an accurate and efficient solution of the TFC steady-state problem. The flying height reduction at the read transducer on several air bearing and heater design combinations predicted by the TFC solver is shown to be in good agreement with experiment data. This chapter is organized as follows. Section 2.2 briefly reviews the finite volume approach for solving the steady-state generalized Reynolds equation and obtaining the air bearing pressure distribution. Section 2.3 reviews the heat transfer model prescribing the heat flux at the air bearing surface. Section 2.4 outlines the procedure of solving for the heater-induced protrusion in ANSYS. The integrated

iterative approach is presented in Section 2.5 and a comparison between numerical predictions and measured data are given in Section 2.6.

2.2 The steady-state generalized Reynolds equation

The governing equation for the air bearing between the head and disk is the steady-state generalized Reynolds equation which can be written in the following non-dimensional form [20, 21]:

$$\frac{\partial}{\partial X}[\hat{Q}PH^3\frac{\partial P}{\partial X}-\Lambda_x PH]+\frac{\partial}{\partial Y}[\hat{Q}PH^3\frac{\partial P}{\partial Y}-\Lambda_y PH]=0 \tag{2.1}$$

where $X = x / L$ is the x coordinate (along the slider's length direction) normalized by the slider's length L, $Y = y / L$ is the y coordinate (along the slider's width direction) normalized by L, $P = p / p_a$ is the air bearing pressure normalized by the ambient pressure p_a, $H = h / h_m$ is the spacing normalized by an initial spacing at the slider's trailing edge center h_m, Λ_x and Λ_y are the bearing numbers in the x and y directions and are defined by:

$$\Lambda_x=\frac{6\mu UL}{p_a h_m^2},\Lambda_y=\frac{6\mu VL}{p_a h_m^2} \tag{2.2}$$

where μ is the viscosity of the air, U and V are the sliding velocities in the x and y directions. Because the head-disk spacing in current hard disk drives is only several nanometers, which is small compared with the mean free path of the air molecules, we can no longer assume the no-slip boundary condition. A Poiseuille flow factor $\hat{Q}$ is introduced which reflects the type of the slip boundary conditions applied. Here we use the slip correction developed by Fukui and Kaneko [22, 23] which was based on the linearized Boltzmann equation and was demonstrated to be applicable to nanometer spacings [24] :

$$\hat{Q}=f(\frac{K_n}{PH}) \tag{2.3}$$

where $K_n = \lambda / h_m$ is the Knudsen number and f is given by Fukui and Kaneko [23] .

We use the CML static solver, which uses a control volume approach [25] combined with an alternating direction line sweeping method and multi-grid method for acceleration, to solve (2.1) for a given flying attitude (nominal flying height, pitch and roll) [26]. In order to obtain the slider's flying attitude at a given suspension load, the procedure starts from solving (2.1) using a guessed flying attitude. Then a Quasi-Newton iteration method [27], which has the advantage of calculating the full Jacobian matrix only once, is applied to search for the new flying attitude. The iteration continues by updating the Jacobian matrix without full re-evaluation, until the updated flying attitude guarantees the balance between the suspension load and the air bearing pressure.

2.3 Heat flux at the air bearing surface of a flying slider

The first heat transfer model for the head disk interface was proposed by Zhang and Bogy [16], who solved the Navier-Stokes equation with discontinuous boundary conditions and obtained an analytical formula for heat flux q at the air bearing surface:

$$q = -k \frac{T_s - T_d}{d + 2\frac{2-\sigma_T}{\sigma_T}\frac{2\gamma}{\gamma+1}\frac{1}{\Pr}\lambda} \tag{2.4}$$

where k is the thermal conductivity of the air, T_s is the slider's temperature, T_d is the disk's temperature, d is the local flying height of the slider, σ_T is the thermal accommodation coefficient, γ is the heat capacity ratio of the air, λ is the local mean free path of the air, $\Pr = \nu/\alpha$ is the Prandtl number of the air, ν is kinetic viscosity of the air, and α is thermal diffusivity of the air.

The mean free path λ appearing in equation (2.4) is defined as the average distance traveled by gas molecules between consecutive collisions at the equilibrium state and the gas molecules are assumed to move freely without any boundaries. However, this condition is not satisfied in the slider air bearing case, because the slider and disk put constraints on the air molecules' motions [28]. Chen, Liu and Bogy later proposed a heat conduction model, in which a modified mean free path considering the existence of boundaries is used to substitute the λ term in equation (2.4) [19]. This modified mean free path is obtained by taking an average of the distance each molecule can travel in the gas film existing between the slider and disk and can be written as:

$$\lambda_m = \begin{cases} \lambda(1 - \frac{1}{4}\frac{\lambda}{h}), & h \geq \lambda \\ \lambda(\frac{3}{4}\frac{h}{\lambda} - \frac{h}{2\lambda}\ln(\frac{h}{\lambda})), & h < \lambda \end{cases} \tag{2.5}$$

By replacing the original mean free path term λ in equation (2.4) with λ_m defined in equation (2.5) , a modified model prescribing the heat flux at the air bearing surface is obtained. This model is proved to agree better with the numerical results predicted by the linearized Boltzmann equation, especially for the inverse Knudsen number $D < 1$ case, where D is defined as:

$$D = \frac{\sqrt{\pi}h}{2\lambda} \tag{2.6}$$

However, the difference of these two models in predicting a TFC slider's steady-state flying attitude is proved to be negligible because the local mean free path is inversely proportional to the local pressure and thus is much smaller in the transducer area compared with the ambient mean free path because of the pressure peak at the protruded area. Thus the inverse Knudsen number, even at the minimum FH point, is not so small to induce any significant error [14].

2.4 Protrusion profile due to heater actuation

For a TFC slider, during read/write operations, a power is supplied to the heater embedded in the slider, resulting in a local protrusion around the read/write transducers and a magnetic spacing drop of several nanometers. To solve the protrusion resulting from this thermo-mechanical process, a coupled field analysis on a full finite element model of the slider body, in which structures of the read/write elements, heater and shields are characterized in detail, is needed. The commercial finite element software,

ANSYS, which is widely used in today's hard disk drive industry, is employed for this analysis.

Although the temperature and stress fields are coupled in this problem, the major effect is the temperature rise in the slider body that causes the slider's deformation. Thus a sequential method, which uses the temperature field solved from a thermal analysis as an input to the subsequent structural analysis, is considered to be an appropriate choice [29].

During the solution for the temperature field in the slider body, the disk temperature is assumed to be constant and equal to the ambient temperature. Thus a film coefficient h_{film} can be defined from (2.4) :

$$h_{film} = \frac{k}{d + 2\dfrac{2-\sigma_T}{\sigma_T}\dfrac{2\gamma}{\gamma+1}\dfrac{1}{\Pr}\lambda} \tag{2.7}$$

The flying height h and air bearing pressure p for calculating the local λ in (2.7) are obtained by solving (2.1). h_{film} varies with the location (x, y) and is applied as a boundary condition at the air bearing surface for the thermal analysis. The temperature field solved from the thermal analysis is then imported as an input to the subsequent structural analysis. In the meantime, the degrees of freedom of the nodes in the finite element model are switched from temperature to displacements (*ux*, *uy*, *uz*). The displacement in the flying height direction (*uz*) at the air bearing surface, i.e., the protrusion geometry, can be obtained from the results of this structural analysis.

2.5 An integrated iterative approach for a TFC slider's steady-state flying attitude

The major difficulty of solving the steady-state TFC problem is the coupling relation between the air bearing pressure and the heater-induced protrusion geometry. Juang, Chen and Bogy were the first to apply an iterative procedure to this problem [12]. The CML air bearing program is first used to solve the slider's flying attitude and the air bearing pressure. Then the cooling coefficient at the air bearing surface is calculated according to equation (2.7) and used as thermal boundary conditions in the finite element model of the slider built in ANSYS. A coupled-field analysis is conducted to obtain the protrusion on the air bearing surface. This protrusion profile is then used to update the original air bearing geometry and obtain a new flying attitude and air bearing pressure solution. This iteration continues until the flying attitude solution is converged. This iterative procedure is proved experimentally to give good predictions of a TFC slider's steady state flying attitude under a given actuation power [13]. However, it requires designers to manually switch between different softwares which makes the solving procedure inefficient and tedious.

In this section an integrated TFC solver written in APDL (ANSYS Parametric Design Language) and packaged in macros directly executable from ANSYS is developed. The CML and ANSYS solvers are iteratively called in this solver so that repeated GUI (Graphic User Interface) operations and manual switches between solvers can be avoided.

As an improvement to the original approach, which uses a uniform heat generation rate in the heater body, an electrical analysis is conducted before the thermal analysis in the current TFC solver, which uses the voltage applied across the heater pads to calculate the distribution of heat generation rate inside the heater body. In this way, the non-uniform heat generation caused by the irregular heater shape is also well captured, which should be useful for heater geometry optimizations.

The numerical process of the TFC solver is summarized in the flowchart shown in Figure 2.3. The heat flux model is implemented at the end of the air bearing solving procedure. The top surface of the slider is glued to the suspension and an equivalent film coefficient of 2000 $W/m^2 \cdot K$ is applied. A film coefficient of 100 $W/m^2 \cdot K$ is used for the other four sides of the slider. At the end of the structural analysis, the displacement solutions defined on ABS nodes of the FE model are mapped onto a rectangular mesh consistent with the CML-defined ABS mesh and exported to the air bearing program. The solution is usually convergent in 3-4 iterations. A detailed manual of the TFC solver is attached as an appendix to the dissertation.

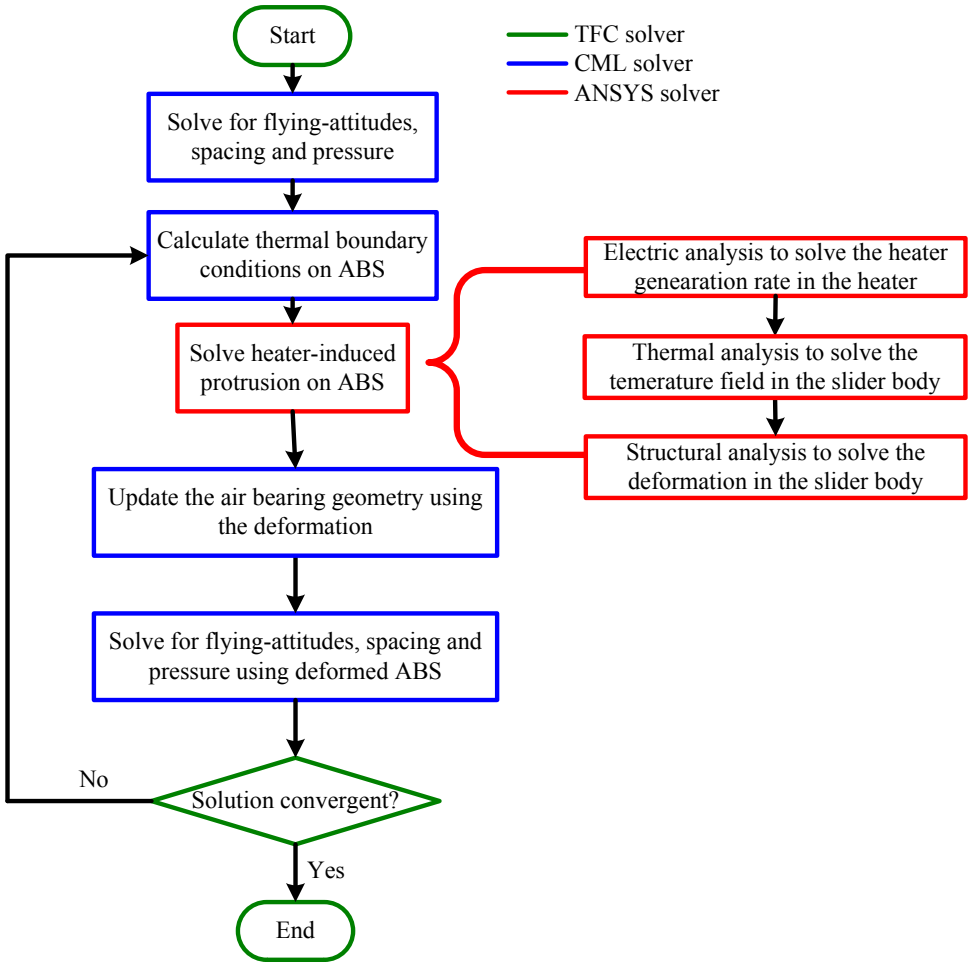

Figure 2.1 Flow chart of a TFC steady-state analysis. The iterative calls of CML and ANSYS solvers and convergence controls are implemented in the TFC solver. The solution is usually convergent in 3-4 iterations.

2.6 Accuracy of the numerical solution

To verify the accuracy of the numerical method, we compared the numerical prediction of the flying height drop at the read transducer with the measured data. The measurements utilized the read-back signal of the magnetic head operating in commercial hard disk drives. The read-back signal is converted to the FH changes at the read transducer by applying the Wallace spacing loss theory [30]. Specifically, the magnetic spacing variation due to the thermal actuation can be calculated by [31]:

$$\bar{d}_1 - \bar{d}_2 = -\frac{rm}{f} \ln \frac{E(\bar{d}_1)}{E(\bar{d}_2)} \tag{2.8}$$

where $\bar{d}$ is the magnetic spacing at a specific actuation power, m is the disk rotating speed, r is the track radius, f is the recording frequency, E is the amplitude of the readback voltage, which varies with the magnetic spacing . The FH change at the read transducer is equal to the magnetic spacing change, so we can calculate the FH change at the read transducer between any two actuation powers by applying (2.8). In experiments, the actuated FH at a specific actuation power is measured repeatedly and the average value is taken to compare with the simulation result. The standard deviation σ of the measured actuated FH varies with the actuation power. However, σ of the measured actuated FH is within 5% of the average actuated FH.

The experiment data was supplied by Western Digital Corporation (unpublished) and several different commercial magnetic head designs were subject to this study. Figure 2.2 and Figure 2.3 show the simulated and measured flying height drops at the read transducer as a function of the normalized heater power for two different air bearing and heater design combinations. The numerical predictions obtained by the TFC solver are shown to be in good agreement with the experimental results with a maximum relative error less than 5%. The same studies are repeated on several different air bearing and heater design combinations, and the relative errors between the simulated and measured data are in general within 15% and in most cases less than 5%.

2.7 Summary and conclusion

A TFC solver designed for solving the steady-state flying attitude of a TFC slider is developed and implemented in this chapter. The solver is implemented in APDL and packaged as macros directly executable in ANSYS. The air bearing pressure and spacing fields in the head disk interface are solved using a CML Reynolds equation solver and the protrusion geometry due to heater actuation is solved using an ANSYS coupled-field solver. The air bearing's cooling effect on the heater-induced protrusion is modeled by prescribing the location-varying film coefficient at the air bearing surface. The coupling between the pressure and spacing fields with the temperature and strain fields is treated using an iterative procedure. This solver avoids manual switching between different softwares, repeated GUI operations and solutions mappings on different meshes and thus realizes an efficient solution to the TFC problem. Several different air bearing and heater design combinations are then subject to both simulation and experimental studies. Simulations and experiments are in good agreement with each other, with a relative error less than 15% in general and less than 5% in most cases.

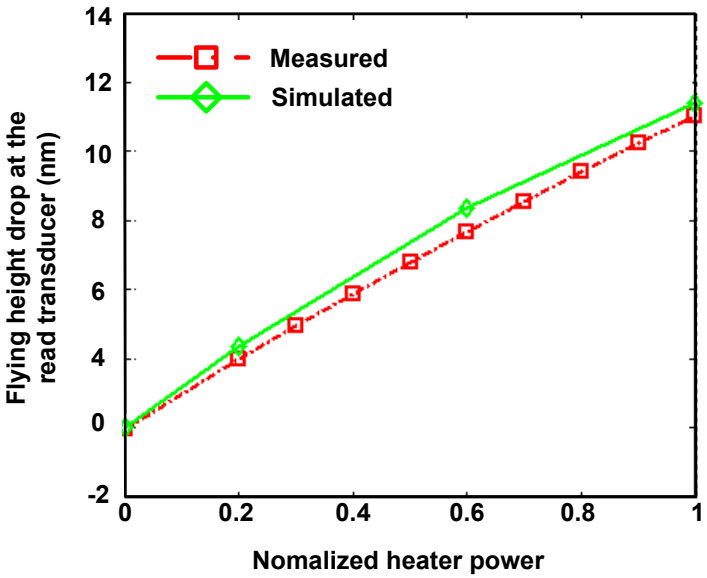

Figure 2.2 Flying height drop at the read transducer as a function of the normalized heater power. Both measured and simulated data are shown where the relative error between the simulated data and measured data is less than 5%.

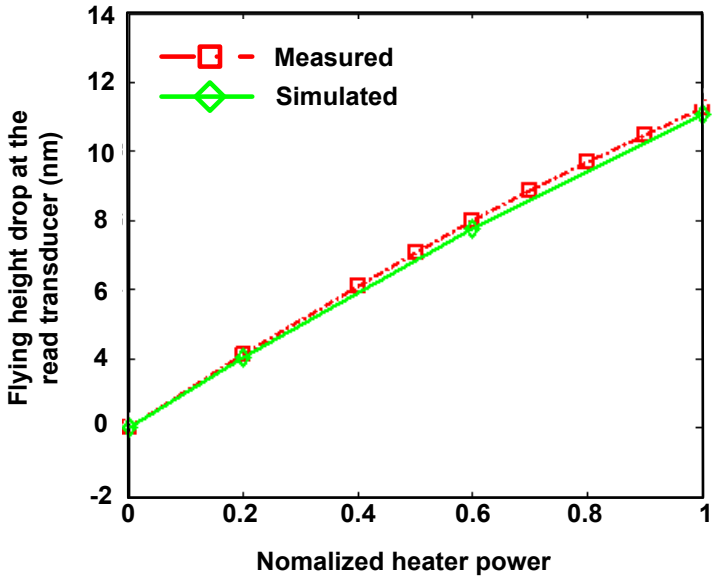

Figure 2.3 Flying height drop at the read transducer as a function of the normalized heater power. Both measured and simulated data are shown where the relative error between the simulated data and measured data is less than 5%.

Chapter 3

Ambient effects on a TFC slider's steady-state performance

3.1 Introduction

As the dominant data storage device in the past decades, today's hard disk drive is widely used in general purpose computers, which work in a wide variety of ambient conditions. Modern HDDs are equipped with an air filter which equalizes the atmospheric pressure and humidity between the HDD enclosure and its outside environment. During operation the inside temperature of HDDs can rise to as high as 100^{o}C. These ambient factors can significantly change the properties of the gas being dragged into the gap between the flying head and disk, and they can critically affect the performance of the flying head.

Cha et. al. [32] investigated both numerically and experimentally the effects of ambient temperature and pressure on a slider with a flying-height on the order of 50 nm They found that the increases in the air viscosity μ and mean free path λ at raised temperatures have offsetting effects and result in very limited change in the slider's flying height (~1 nm for 17 ^{o}C change in temperature). They also showed that the slider's flying-height can drop by ~15 nm for 10 kft change in altitude. More recently, a non-TFC slider's flying height sensitivity to temperature changes in a humid environment was investigated [33, 34]. It is found that the slider's flying height can drop substantially in a humid environment at 60 ^{o}C ambient temperature, and the numerical model agrees well with experimental results. Though these works have proved the significant effects of ambient conditions on the flying slider's performance, so far no work has been reported on a TFC slider's response to ambient conditions. However, ambient conditions affect in a more complicated way in the TFC case because they affect not only the air bearing pressure but the protrusion geometry as well. Both factors make significant contributions to a slider's flying height and are actually coupled together. This makes it difficult to extend the conclusions on non-TFC sliders to the TFC case. Further, with the application of TFC technology, the physical spacing in HDDs is pushed to below 5 nm, and a flying height fluctuation of several angstroms can potentially cause head-disk contacts or even head crashes. Thus, understanding TFC sliders' response to ambient conditions has become an important issue for today's HDD reliability.

Considering the potential damage that can be caused by ambient changes, a hermetically sealed HDD seems to be another appealing choice to resolve most of the problems encountered with low pressure, temperature variations, high humidity environments, etc. Also, it provides the option of filling the HDD with the inert gas Helium, which has the potential to reduce the temperature rise inside HDDs during operation and protect the head and disk from corrosion [35-38] . However, providing a seal well maintained across a wide temperature and pressure range is a challenge, and for Helium gas, it is even more difficult because of its small density. In consideration of performance and cost, a drive filled with air-helium mixtures might be a feasible solution [36, 37].

In this chapter we investigated the static performance of TFC sliders under ambient conditions and in air-helium mixtures, using the numerical approach developed in Chapter 2. A part of the numerical results is compared with experimentally measured data, in order to validate the approach presented here. We also look into the mechanism working behind the TFC sliders' responses to ambient changes in order to provide general guidelines for air bearing and heater designers to improve read/write head performance and reliability. The chapter is organized as follows. Sections 3.2 and 3.3 investigate a TFC slider's static performance at different ambient pressures, humidity levels and temperatures. Section 3.4 focuses on its performance in air-helium mixtures.

3.2 TFC sliders at different ambient pressures

When a HDD is subject to applications at high altitudes, the air bearing's load capacity and cooling capability changes with the reduced ambient pressure p_0 and increased mean free path λ. In this section, we use the numerical model developed in Chapter 2 to obtain the steady state flying height of a TFC slider at a given actuation power and compare it with the heater-turned-off case to get the actuated FH, for a specified altitude. Specifically, the ambient pressure p_0 and mean free path λ used for solving the generalized Reynolds equation are modified according to the specified altitude. The local mean free path λ for calculating the air bearing cooling coefficient is given by [39]:

$$\lambda = \frac{2^{1/2} R^* T}{2\pi N_A \sigma^2 p(x,y)} \tag{3.1}$$

where $R^* = 8.31432$ *J/(mol·K)* is the gas constant, T is the ambient temperature and is set to 298K in this investigated case, $N_A = 6.02213\times10^{23}$ is the Avogadro constant, $\sigma = 3.65\times10^{-10}$ m is the effective collision diameter of the air molecules, $p(x,y)$ is the pressure at a local point (x, y) in the air bearing.

The TFC actuated FH at the read transducer is measured by operating the HDD in an altitude chamber and measuring the read-back signal [40]. The experiment data was supplied by Western Digital Corporation (unpublished). Simulations and experiments were conducted using an industry designed femto-sized (0.85 mm × 0.7 mm × 0.23 mm) TFC slider for two altitudes: sea level and 3 km altitude, and the results are shown in Figure 3.1. Numerical predictions agree very well with experiments and both indicate an increase in actuated FH at a higher altitude (or lower ambient pressure).

For a TFC slider, the local flying height at the transducer location, which is most important, is determined by two factors. One is the heater-induced protrusion at the transducer location. The other is how much the slider is being pushed back due to the pressure peak induced by the local protrusion. The latter is commonly evaluated using the pushback factor α, which is defined as

$$\alpha = 1 - \frac{\text{actuated flying height}}{\text{heater induced protrusion}} \tag{3.2}$$

These two factors, namely, the heater-induced protrusion and the pushback factor, are always combined together in measurements; however, with numerical simulations, we

can conveniently look at these two factors separately and gain some insight into the causes.

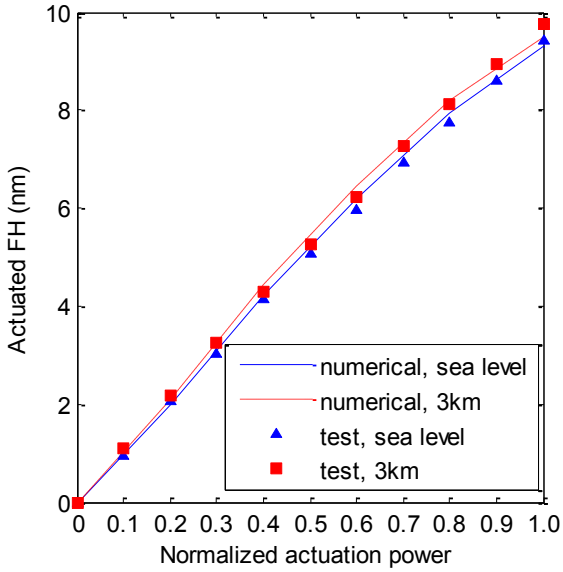

Figure 3.1 Actuated FH as a function of the normalized actuation power for an industry designed femto-sized TFC slider. Numerical and experimental results are shown for two altitudes: sea level and 3 km. Numerical predictions agree very well with experiments. Both indicate an increase in actuated FH at a higher altitude (lower ambient pressure).

3.2.1 Effects of ambient pressure on the TFC protrusion

Figure 3.2 shows the simulated TFC protrusion along a line parallel to the y-direction (slider width direction) and passing through the read transducer ($x = x_{\text{transducer}}$). The curves are obtained with a normalized actuation power of 1. Results of sea level and 4 km altitude are shown. The location of the read transducer is indicated in the figure. The protrusion is larger at the higher altitude, which suggests that more heat is dissipated at the air bearing surface for this case.

In Figure 3.3, we show the air bearing cooling coefficient h_{film} along the line parallel to the slider's width direction and passing through the read transducer with a normalized actuation power of 1 at two altitudes: sea level and 4 km. An obvious difference can be observed at the transducer location, showing less cooling at the higher altitude.

Referring to equation (2.7), the air bearing cooling coefficient h_{film} is determined by the local FH d and mean free path λ, both varying with altitude. On the one hand, the local d at the transducer area is smaller (usually, but not always) at higher altitudes, and this enhances the heat dissipation, as predicted by equation (2.7). On the other hand, the pressure at the transducer area is smaller at the higher altitude, as shown in Figure 3.4, which increases the local mean free path λ, as shown in equation (3.1), and this reduces the local cooling coefficient h_{film}, as predicted by equation (2.7). Altitude-induced changes in d and λ at the transducer area have offsetting effects on the cooling coefficient h_{film}, however, the effect of increased λ apparently dominates in the investigated case. Physically, the increase in λ means fewer molecules exist in the head disk interface. As a

result, fewer molecules are available for providing heat exchanges between the slider and disk, which leads to an increased protrusion.

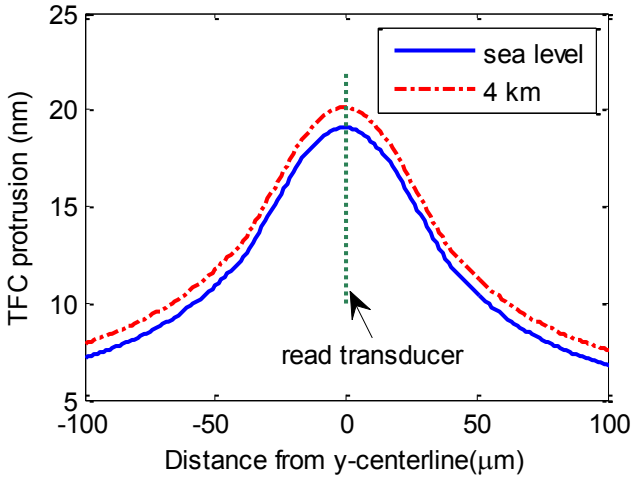

Figure 3.2 the TFC protrusion along the line parallel to the slider's width direction and passing through the read transducer with a normalized actuation power of 1 at two altitudes: sea level and 4 km. The location of the read transducer is indicated in the figure. The protrusion is larger for the 4 km case.

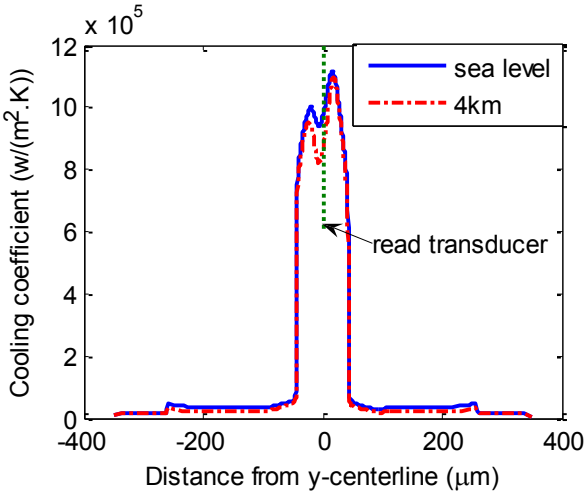

Figure 3.3 The air bearing cooling coefficient h_{film} along the line parallel to the slider's width direction and passing through the read transducer with a normalized actuation power of 1 at two altitudes: sea level and 4 km. The location of the read transducer is indicated in the figure. The cooling coefficient h_{film} is smaller for the 4 km case.

3.2.2 Effects of ambient pressure on the pushback factor

Pushback is a response of the air pressure to the protruded air bearing surface, thus a change in the pushback factor is actually a combined effect of the altitude, as well as the protrusion. To separate the effect of the protrusion and look at the altitude-induced pushback change alone, we apply the same protrusion profile, which is the protrusion profile obtained in the sea level case, on the slider flying at sea level and 4km respectively. As shown in Figure 3.5, the pushback factor goes up with increasing

actuation powers, and experiences higher values at sea level than at 4 km given the same protrusion. This result implies that the pressure change due to the TFC protrusion is smaller at higher altitude than at sea level. Thus it requires less pushback to regain the equilibrium at altitude [41]. To verify this, we fix the slider at 12 nm FH at its trailing edge center, with 90 μrad pitch angle and 0 roll angle, then we modify the air bearing surface with sea level protrusions at increasing actuation powers. As shown in Figure 3.6, the rate of change in the air bearing force with increasing actuation power is higher at sea level, showing a stronger stiffening response of the air bearing. Accordingly, to balance the suspension load, the air bearing has to push the slider up farther so that the increase in the air bearing force can be compensated.

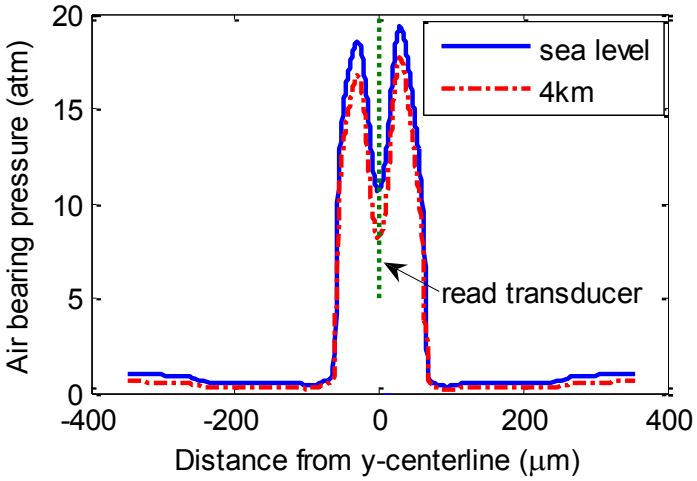

Figure 3.4 The air bearing pressure along the line parallel to the slider's width direction and passing through the read transducer with a normalized actuation power of 1 at two altitudes: sea level and 4 km. The location of the read transducer is indicated in the figure. The pressure at the read transducer is lower for the 4 km case.

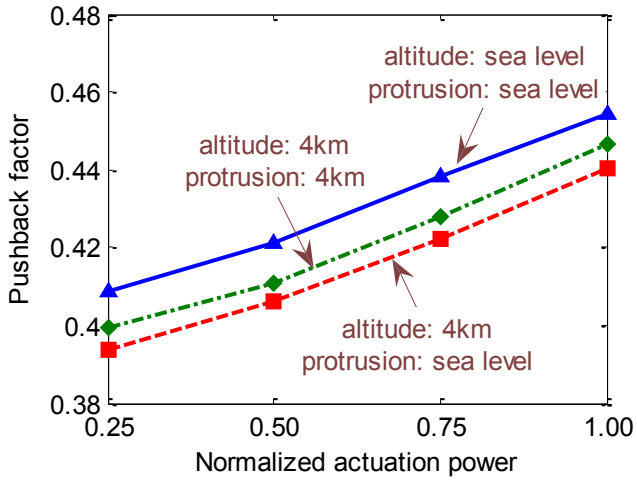

Figure 3.5 The pushback factor as a function of the normalized actuation power. Three cases are investigated: (i) the slider flying at sea level with the protrusions obtained at sea level; (ii) the slider flying at 4km with the protrusions obtained at 4km; (iii) the slider flying at 4km with the protrusions obtained at sea level.

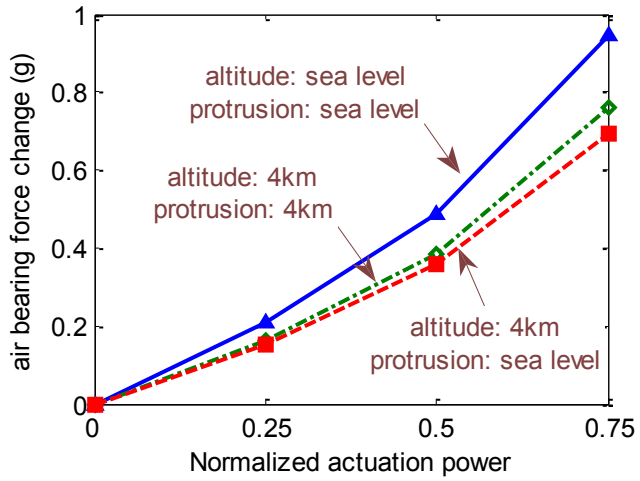

Figure 3.6 the air bearing force change as a function of the normalized actuation power. Three cases are investigated: (i) the slider flying at sea level with the protrusions obtained at sea level; (ii) the slider flying at 4km with the protrusions obtained at 4km; (iii) the slider flying at 4km with the protrusions obtained at sea level.

On the other hand, if the 4 km protrusion is used for the slider flying at 4 km altitude as in Figure 3.5, the resultant pushback factor is higher compared with the sea level protrusion/4 km altitude case. This is reasonable as we have shown in 3.2.1 that the 4 km protrusion is larger, so stronger pushback is expected. In addition, the pushback factor is still lower compared with the sea level protrusion/sea level altitude case. This indicates that the altitude-induced change in the air bearing pressure is the dominating factor in determining the pushback factor. Figure 3.6 also shows the fixed-altitude simulation results for the 4 km protrusion / 4 km altitude case. The result is consistent with Figure 3.5 as the rate of change in the air bearing force for the 4 km protrusion / 4 km altitude case is higher than the sea level protrusion / 4 km altitude case, but lower than the sea level protrusion / sea level altitude case.

In the proceeding paragraphs, we analyzed the variation of the TFC protrusion and pushback factor under altitude changes. The increased protrusion and reduced pushback factor both contribute to the increased actuated FH at higher altitudes. To quantify these two contributions, we compare the actuated FH of the following four cases: (a) the slider flying at sea level with sea level protrusions; (b) the slider flying at sea level with 4 km protrusions; (c) the slider flying at 4 km with sea level protrusions; (d) the slider flying at 4 km with 4 km protrusions. A comparison between (a) and (b) reveals how much the variation in the TFC protrusion alone affects the actuated FH. A comparison between (a) and (c) tells us the effects of reduced pushback on the actuated FH. The difference between (a) and (d) is the combined effects of these two. In Figure 3.7, the curves for cases (b) and (c) almost overlap, showing that the two factors have roughly equivalent effects for this investigated design.

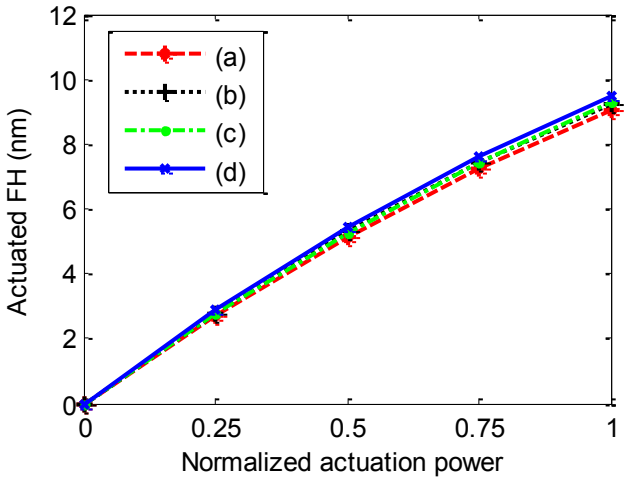

Figure 3.7 The actuated FH as a function of the normalized actuation power for: (a) the slider flying at sea level with sea level protrusions; (b) the slider flying at sea level with 4 km protrusions; (c) the slider flying at 4 km with sea level protrusions; (d) the slider flying at 4 km with 4 km protrusions.

3.3 TFC sliders at different humidity levels

Due to the heater-induced protrusion, the air bearing pressure, especially at the protruded area, can be raised to twenty or even thirty times the ambient pressure. This compression effect leads to super saturation of the water vapor existing in the gas film, which is brought in through the air filter. As a consequence, the water molecules condense in the air bearing until the partial pressure of water vapor in the gas film is reduced to the saturation vapor pressure. Due to this effect, the air bearing pressure decreases which requires the slider to adjust its flying attitude so that the balance with the suspension load can be maintained.

To look into the response of a TFC slider to ambient humidity changes, we employ the numerical model proposed by Zhang et. al., which has been verified by experiments to give good predictions of the flying-height drop due to water condensation [34]. Specifically, for a slider operating in a humid environment with a relative humidity level *RH*, the water vapor pressure in the air bearing can be written as:

$$p_{vapor} = p_{sat} \cdot RH \tag{3.3}$$

where p_{vapor} is the partial pressure of water vapor in the air bearing, p_{sat} is the saturation pressure of the water vapor. Here we assume that the p_{sat} is a function of temperature, and p_{vapor} and p_{sat} are uniform throughout the air bearing. p_{sat} at any given temperature can be calculated from the empirical formula by Goff and Gratch [42].

The air is compressed as it is dragged through the head disk spacing. Accordingly, the water vapor pressure p_w in the air bearing increases proportionally with the air bearing pressure p:

$$p_w = p_{vapor} \cdot \frac{p}{p_0} \tag{3.4}$$

where p_0 is the ambient pressure.

Condensation occurs whenever p_w is greater than p_{sat}, thus the pressure loss due to water condensation can be written as:

$$\Delta p = p_w - p_{sat} \tag{3.5}$$

Combining (3.3), (3.4), and (3.5), we can further write Δp as:

$$\Delta p = p_{sat}(RH \cdot \frac{p}{p_0} - 1) \tag{3.6}$$

To get the total air bearing force acting on the slider, the air bearing pressure p is integrated over the entire air bearing surface. Whenever p_w is greater than p_{sat}, the original air bearing pressure obtained by solving the generalized Reynolds equation is reduced by Δp. An iterative procedure is employed until this adjusted air bearing force is balanced with the applied suspension load.

We first look at the flying height of the slider when the TFC heater is off. Figure 3.8 shows the transducer's flying height as a function of the relative humidity for two ambient temperatures: 25°C and 50°C. The flying height decreases with increasing relative humidity because the pressure loss due to water condensation is greater in higher humidity levels, as shown by (3.6). As a consequence, the slider has to fly lower so that the loss in pressure can be compensated by further compression of the air film. It is also noticed that the flying height in a higher ambient temperature is lower than that in a lower temperature for the same humidity level. Ambient temperature affects the load capacity of the air bearing mainly through two parameters: the viscosity μ and the mean free path λ. Both increase with the ambient temperature, however, the increase in μ increases the load capacity of the air bearing, whereas the increase in λ reduces the load capacity. Which effect becomes dominant varies with the specific air bearing design and for this case, the increase in λ overwhelms. Further, Figure 3.8 also shows that the flying-height drops more with increasing *RH* at a higher ambient temperature. The flying-height drops by 0.49 nm for the 20 °C case, but by 2.81 nm for the 50 °C case, when *RH* is increased from 0 to 100%. It is considered to be mainly due to the fact that p_{sat} increases exponentially with temperature and this results in a greater Δp.

Figure 3.8 shows the transducer's flying height as a function of *RH* when 100 mW power is applied to the TFC heater, for the 25 °C and 50 °C cases. The general trend is very similar to the result for the heater-turned-off case. However, the flying-height drop due to *RH* increase is smaller, for both cases. The flying-height drop is 0.40 nm for the 25 °C case and 2.14 nm for the 50 °C case. This comparison reveals an interesting fact that TFC sliders have the capability of suppressing the FH fluctuations due to ambient humidity changes. And this can be explained from the variation in heater-induced protrusion when the TFC power is on.

Figure 3.10 shows plots of the heater-induced protrusion along the slider's y-centerline, showing that the protrusion decreases with increasing relative humidity. The water condensation leads to flying-height drop, especially at the transducer area, where the compression ratio of the air film, p/p_0 is highest. The spacing reduction enhances heat conduction and results in a smaller protrusion, which cancels out a small part of the FH loss due to water condensation. As shown in Figure 3.10, such an effect grows with relative humidity.

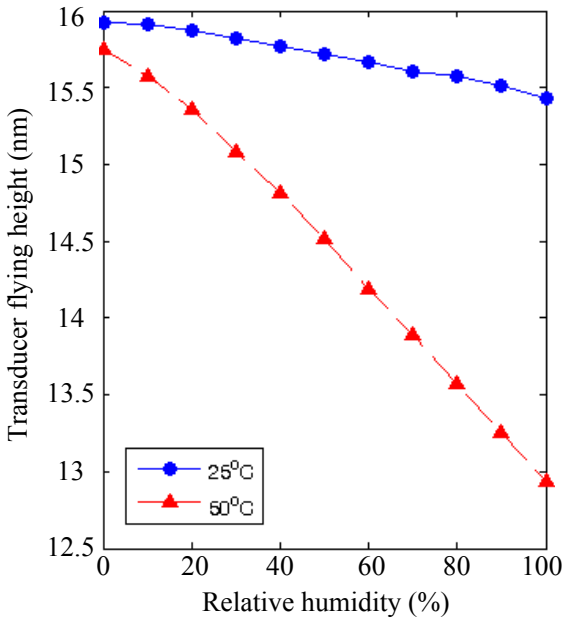

Figure 3.8 Transducer's flying height of the investigated slider as a function of relative humidity for two ambient temperatures (25°C and 50°C) when the heater is off. For both cases, flying height decreases with the increase in relative humidity and the FH drop is greater with a higher ambient temperature.

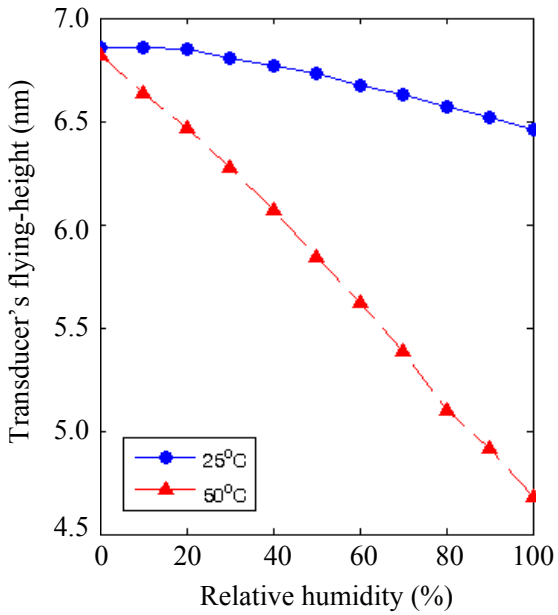

Figure 3.9 Transducer's flying height of the investigated slider as a function of relative humidity for two ambient temperatures (25°C and 50°C) under 100 mW TFC actuation. The general trend is very similar to the heater-off case, but the flying-height drop with increasing humidity levels is smaller, compared to the heater-off case.

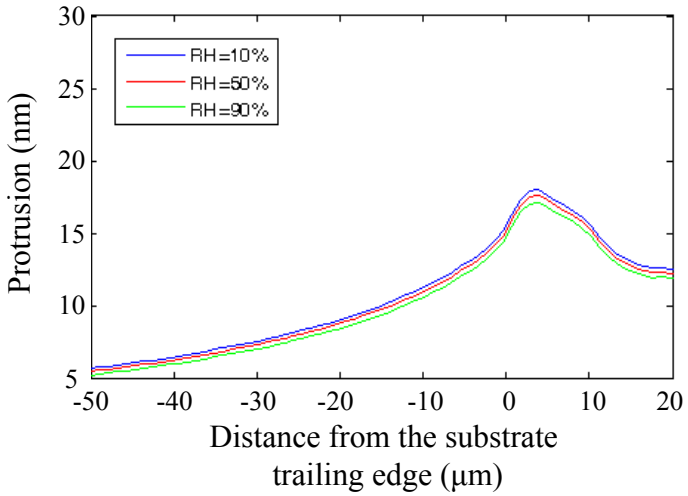

Figure 3.10 Heater-induced protrusion along the slider's y-centerline when the ambient temperature is 50 ^{o}C. Three cases are shown: *RH* = 10%, 50% and 90%. Protrusion decreases with increasing relative humidity.

This "self-tuning" capability of a TFC slider can also be seen from Figure 3.11. The flying-height loss at the transducer's location is shown as a function of the TFC actuation power, for two cases: dry air and *RH* = 80% air. At a lower actuation power, say 20 mW, the flying height loss is the same for both the dry air and humid air. However, the humid air curve deviates from the dry air curve, as we increase the actuation power, showing the TFC slider is sacrificing part of its actuation efficiency to compensate the flying-height loss due to the water condensation. Such an effect gets stronger at a higher actuation power. Therefore, a TFC slider tends to perform more reliably in terms of the consistence of read-write spacing, compared with a non-TFC slider.

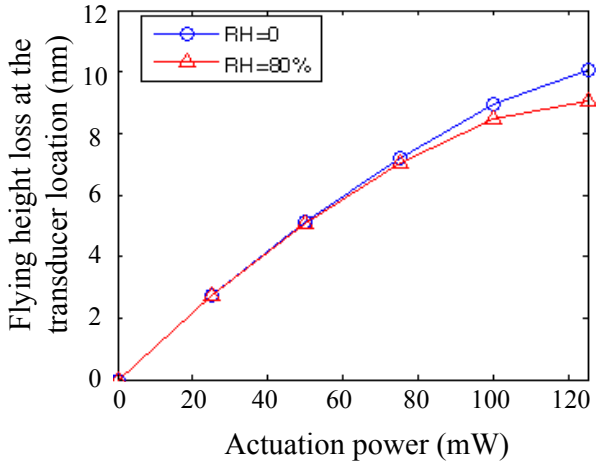

Figure 3.11 Flying-height loss at the transducer's location as a function of the TFC actuation power. Two cases are shown: *RH* = 0 and *RH* = 80%.

3.4 TFC slider at air-helium mixtures

This work was completed jointly with Dr. Nan Liu [37], who completed the numerical modeling of air-helium mixture properties.

As can be seen from equations (2.1) and (2.4), several physical properties of the air-helium mixture are required for the iterative solving procedure of a TFC slider, including the mean free path λ, the viscosity μ, the thermal conductivity k, heat capacity C_p, C_v and density ρ. Due to the distinctive natures of the two gases, the physical properties of the mixture is expected to be quite different from that of either pure air or pure helium and this has to be addressed properly. The mean free path λ in the gas mixture can be written as [43]:

$$\lambda = \frac{\alpha}{\sqrt{2}\pi d_H^2 n\alpha + \pi d_{HA}^2 n(1-\alpha)\sqrt{1+\frac{M_H}{M_A}}} + \frac{1-\alpha}{\sqrt{2}\pi d_A^2 n(1-\alpha) + \pi d_{HA}^2 n\alpha\sqrt{1+\frac{M_A}{M_H}}} \tag{3.7}$$

where d is the diameter of gas molecule, n is the number density, or the number of molecules per unit volume, $d_{HA} = (d_H+d_A)/2$, M is the molecular weight, α is the percentage of the helium in the gas mixture, and the subscripts H and A refer to the values of helium and air respectively. The viscosity μ is calculated by the method of Reichenberg and the thermal conductivity k is calculated by Wassiljewa's formula [44]. These two methods require the critical pressure and critical temperature of air and helium. For the other quantities, namely, C_p, C_v and ρ, their values can be obtained by linear interpolation, for example, $\rho = \alpha\rho_H + (1 - \alpha)\rho_A$ where, and ρ_H and ρ_A are the densities of helium and air, respectively. Table 3.1 lists the physical properties of air and helium required for above calculation. They are taken from [45] and [46].

Table 3.1 Physical properties of air and helium. All the values, except the critical temperature and critical pressure, are for the temperature 300K. Note that 1Poise=0.1Ns/m^2 and 1bar=10^5Pa.

Physical properties	Air	Helium
Molecular diameter (nm)	0.366	0.215
Molecular Weight M (g/mol)	28.966	4.003
Density ρ (kg/m^3)	1.164	0.160
Viscosity (μPoise)	186	200
Heat conductivity k (W/(K·m))	0.0262	0.1567
Heat capacity C_ρ (J/(mol·K))	29.15	20.786
Heat capacity C_v (J/(mol·K))	20.80	12.522
Critical temperature T_c (K)	132.5306	5.19
Critical pressure P_c (bar)	37.86	2.27

Figure 3.12 shows the normalized mean free path, viscosity and thermal conductivity varying with the fraction of helium in the gas mixture. Both the mean free path and heat conductivity increase with α, and the rate of change also increases with α. However, viscosity increases with α until α reaches around 0.8, and then it starts decreasing rapidly. Generally speaking, an increase in the mean free path results in fewer molecules existing in the head-disk interface, and this leads to two effects on the TFC slider. On the one

hand, fewer molecules exist to provide the supportive force, resulting in reduced load capacity of the air bearing. On the other hand, fewer molecules are available to provide the energy exchange, resulting in reduced heat dissipation at the protruded area and a change of the bulge shape of the TFC slider. The increase in the heat conductivity mainly enhances the air bearing cooling, thus it can offset the effect on the TFC bulge profile by an increased mean free path. An increase in the viscosity tends to increase the air bearing load capacity, thus it also offsets the effect by an increased mean free path.

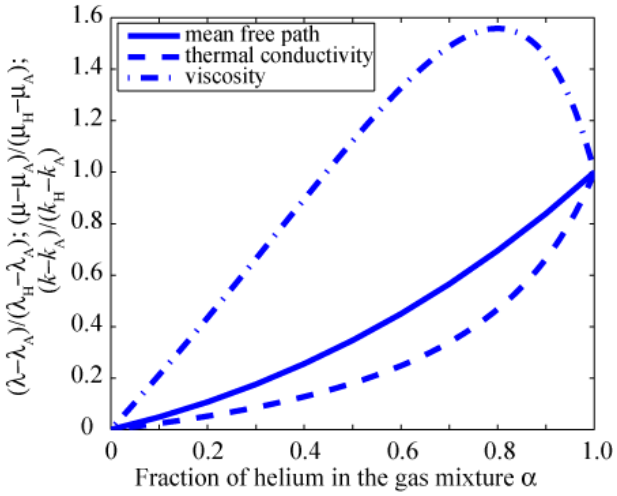

Figure 3.12 the Normalized mean free path λ, viscosity μ and heat conductivity k as a function of the fraction of helium in the air-helium mixture. The normalization ensures that all three variables equal to 0 when α = 0 and equal to 1 when α = 1, so that the rate of change of each variable can be compared.

Figure 3.13 shows the transducer's flying height as a function of the fraction of helium in the gas mixture when the TFC heater is turned off. In this case, the transducer's flying height is determined by λ and μ. For a small α, both the mean free path and viscosity increase with α with an almost constant rate, resulting in offsetting effects on the air bearing's load capacity. Thus the flying-height change at a small α is almost negligible. The rate of change in the mean free path λ then increases, leading to an overall decrease in the air bearing's load capacity and the transducer's flying height. As α exceeds 0.8 and approaches 1, the viscosity starts decreasing with α and this results in an abrupt drop in the transducer's flying height.

When power is applied to the TFC heater, the transducer's flying height also becomes dependent on the local protrusion. According to equation (2.4), the heat flux q at the air bearing surface can be estimated by

$$q \sim -k\frac{T_s - T_d}{d + C\lambda}$$

where the coefficient C is on the order of 1, because the Prandtl number and the heat capacity ratio are both on the order of 1, and the thermal accommodation coefficient is close to 1. The mean free path λ at the transducer area is inversely proportional to the local pressure, which is usually several tens of atms and thus on the same order as the local flying height d. As α increases from 0 to 1, the heat conductivity k changes by 500%, which is much larger compared with the change in d. Thus, the change in heat

conductivity dominates the heat dissipation at the transducer area, resulting in a decrease in the protrusion at the transducer location, as can be seen from Figure 3.14. Accordingly, the flying height loss at the transducer also decreases with α, as shown in Figure 3.15.

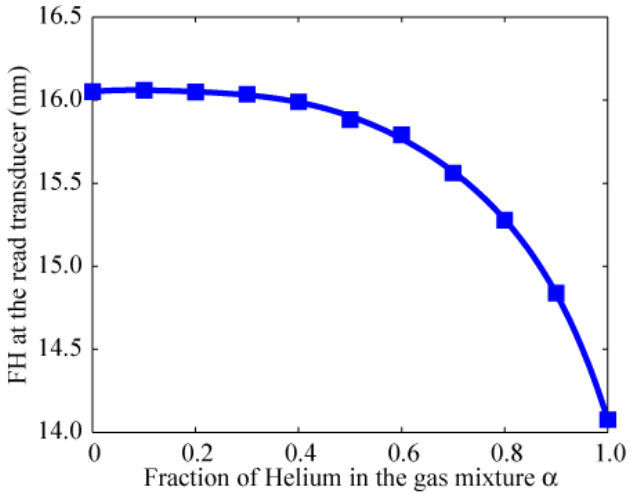

Figure 3.13 the Transducer's flying-height as a function of the fraction of helium in the gas mixture when the TFC heater is off.

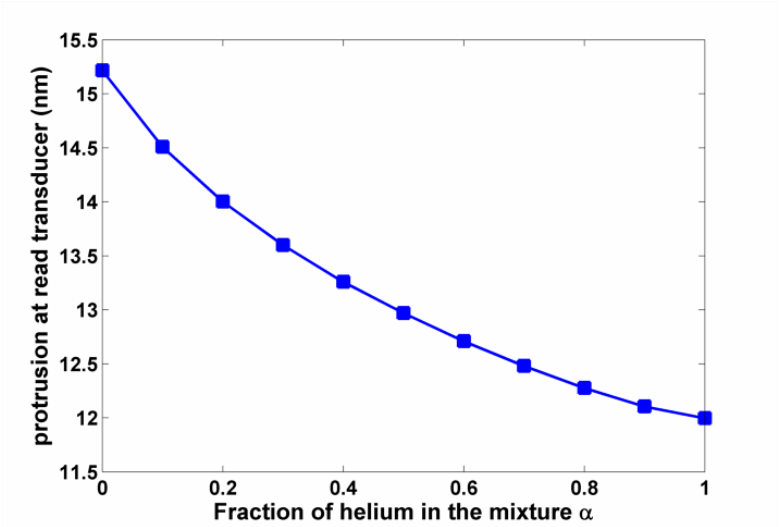

Figure 3.14 the Local protrusion at the transducer's location as a function of the fraction of helium in the gas mixture when a normalized power of 1 is applied to the TFC heater.

The slider's flying height with the heater on, $d_{w/}$, can be calculated by subtracting the the flying height loss d_{loss}, which is shown in Figure 3.15 from the flying height with the heater off, $d_{w/o}$, which is shown in Figure 3.13, i.e., $d_{w/} = d_{w/o} - d_{loss}$. When the fraction of helium is small, $d_{w/o}$ barely changes due to the offsetting effects of increased mean free path and viscosity. On the other hand, the increase in the heat conductivity k results in a reduced d_{loss}, and this leads to the overall increase in $d_{w/}$ in Figure 3.15. However, as α further increases, $d_{w/o}$ starts decreasing when the increase in λ starts dominating and this results in a decreased rate of change in $d_{w/}$ and eventually a decrease in $d_{w/}$. As α exceeds

0.8 and approaches 1, the sign change in the rate of change of μ leads to a rapid drop in $d_{w/o}$ and as a result, $d_{w/}$ decreases faster with α at this stage.

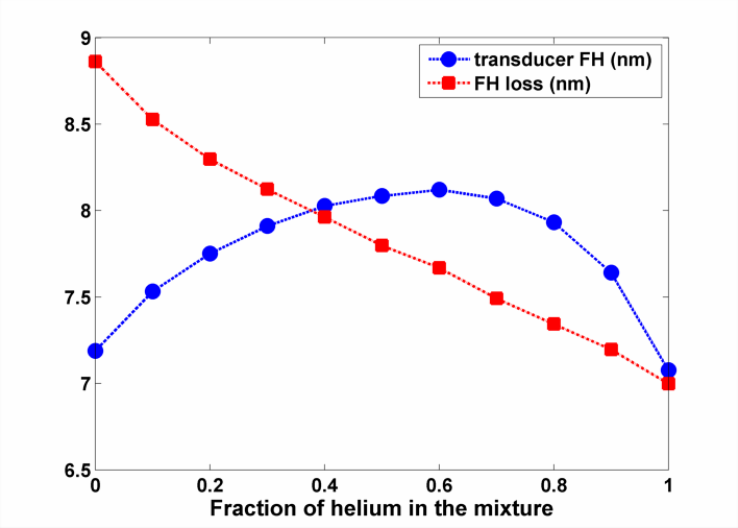

Figure 3.15 Transducer's flying height and corresponding FH loss as a function of the fraction of helium in the mixture when a normalized power of 1 is applied to the TFC heater.

3.5 Summary and conclusion

The effects of altitude, humidity and temperature on TFC sliders are investigated numerically, and they are compared with experimental results in order to testify the validity of the numerical approach. The actuated FH is shown to be greater at an increased altitude due to the increased protrusion and less pushback. The former is caused by the reduced cooling at the transducer area and the latter is associated with the reduced lift force change from the air bearing. It is also discovered that with the TFC heater on, the flying-height change due to humidity fluctuation is reduced and this is attributed to the fact that the TFC protrusion decreases as a response to the local FH drop due to water condensation. Thus a TFC slider tends to perform more reliably in terms of the spacing consistency, compared with a non-TFC slider. A general approach for studying a TFC slider's performance in an air-helium mixture is also proposed here. By applying it to the steady-state solution of a TFC slider, we are able to show that the slider's flying height is a highly nonlinear function of the fraction of helium in the gas mixture α for a given heater power due to the combined effects of the gas mean free path, viscosity and heat conductivity. These results are of practical importance for heater and ABS design in order to reduce the sliders' sensitivities to ambient condition changes and improve the HDI reliability.

Chapter 4

Numerical modeling of a TFC slider at touchdown and over-pushed conditions

4.1 Introduction

The physical clearance between the read-write head and disk in magnetic recording hard disk drives has been continuously decreasing in the past decades in order to meet the ever-increasing demand for higher areal density of stored data [47-51]. With the application of TFC technology current air bearing sliders can fly at a clearance of ~1nm where the slider is subject to increasing interactions with the disk and thus experiences a much more complicated dynamics [52-64].

Some numerical models have been proposed to study a TFC slider's dynamics at near-contact or even contact regions. Ono and Yamane simplified the air bearing slider as a 2-degree-of-freedom (2-DOF) mass-spring system and investigated the dynamic stability of a slider with a small spherical pad at the trailing edge (similar to the TFC protrusion) [65-68]. Based on a similar 2-DOF model, Suh and Polycarpou considered the intermolecular interaction, contact and friction in solving for the slider dynamics, and obtained unstable vibrations of TFC sliders caused by adhesive forces [69-74]. Both models are lumped parameter models, which are capable of a fast solution. However, a 2-D or 3-D lumped-parameter-system is a very rough approximation to the air bearing composed of highly rarified gas in the head disk interface and none of these models are capable of precisely describing the air bearing and interfacial forces' dependence on the air bearing geometry modified by thermal actuation, especially at touchdown and over-pushed conditions. Hua et al. [75-78] studied the slider touchdown dynamics by solving the time-dependent generalized Reynolds equation and including the interfacial forces occurring at touchdown. However the molecular-thin lubricant layer is treated as a soft solid layer that is plastically deformed under contact. So the adhesion due to the lubricant, which is an important boundary lubrication effect, is neglected [79-81]. Another defect associated with this numerical model is that the deformed profiles of solid asperities due to contact are not considered in their interfacial force calculations.

In this chapter we propose a numerical approach, which solves the time-varying Reynolds equation at contact conditions and calculates interfacial forces using a sub-boundary lubrication model [81], to obtain the dynamics of a TFC slider under touchdown and over-pushed conditions. Details of the sub-boundary lubrication model for interfacial force calculations are introduced in section 4.2. The solution of the air bearing pressure generated in the head disk interface is extended to contact in section 4.3. In section 4.4, the dynamics equation of the head-gimbal-assembly is constructed and solved.

4.2 Important interfacial forces at extremely small clearances

The head disk interface at touchdown is composed of not only two rough surfaces, but also an extremely thin lubricant layer (usually several angstroms). The contact

between two rough surfaces is usually modeled using a multi-asperity approach [82, 83]. Greenwood and Williamson were the first to develop a dry contact model by characterizing a single asperity behavior under contact, assuming a statistical distribution of asperity heights and integrating to get the contact force acting on a certain nominal contact area [84]. This model is now widely applied in many engineering areas because of its simplicity and good agreement with experimental data. The contact between two rough surfaces can be considered as the contact between a rigid plane and a nominal flat surface [85]. The nominal flat surface is covered with asperities that have spherical summits and have the same radius of curvature R at their summits. The asperity heights are assumed to distribute randomly and the probability density function of asperity heights is assumed to be $\phi(u)$, which is a Gaussian function with the standard deviation equal to σ_s. Thus the probability that an asperity has a height between u and $u+du$ with regard to its reference plane is $\phi(u)du$. By use of the Hertzian contact theory, the contact force at a single asperity $\bar{F}_c$ can be written as:

$$\bar{F}_c = \frac{4}{3} E\omega^{3/2} R^{1/2} = \bar{F}_c(u-d) \tag{4.1}$$

where E is Hertz elastic modulus of the contact surfaces, $\omega = u - d$ is the interference at the asperity (as shown in Figure 4.1).

When the two planes are separated by a distance d, asperities with a height u greater than d are in contact and have contributions to the contact force. Assuming the total number of asperities to be N, the contact force F_c can be written as:

$$F_c(d) = N \cdot \int_d^\infty \bar{F}_c(u-d)\phi(u)du \tag{4.2}$$

in which N is given by:

$$N = A_n \eta \tag{4.3}$$

where A_n is the nominal contact area, and η is the areal density of asperities.

Here, three parameters are used to describe the topography: the standard deviation of asperity heights σ_s, the curvature of radius of asperities R and the areal density of asperities η. However, it is usually easier to obtain the standard deviation of surface heights σ instead of σ_s in practice. McCool has shown a systematic approach to obtain these topography parameters from the surface profile $z(x)$, assuming $z(x)$ to be a Gaussian random variable [86]. The three spectral moments of $z(x)$ can be written as:

$$\begin{aligned} m_0 &= avg[z^2] \\ m_2 &= avg[(\frac{dz}{dx})^2] \\ m_4 &= avg[(\frac{d^2z}{dx^2})^2] \end{aligned} \tag{4.4}$$

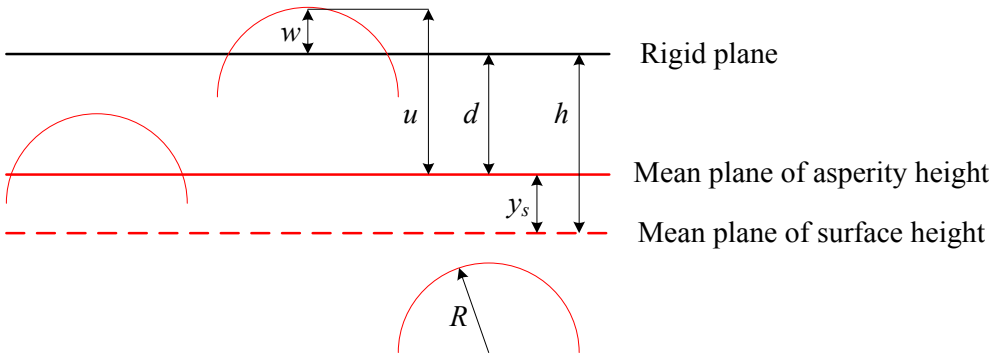

Figure 4.1 Dry contact between a plane and a nominally flat surface. The nominally flat surface is covered with asperities having a spherical summit with a radius of curvature R and asperity height u. The asperity height u is calculated from the mean plane of asperity height, which is dislocated from the mean plane of surface height by y_s. The separation between the plane and the mean plane of asperity height is d, thus for an asperity with a height u greater than d, the interference is calculated as $w = u - d$.

For two contacting rough surfaces 1 and 2, the equivalent composite spectral moments can be written as:

$$\begin{aligned} m_0 &= (m_0)_1 + (m_0)_2 \\ m_2 &= (m_2)_1 + (m_2)_2 \\ m_4 &= (m_4)_1 + (m_4)_2 \end{aligned} \tag{4.5}$$

It is obvious that we can obtain σ as:

$$\sigma = \sqrt{m_0} \tag{4.6}$$

Then the three topography parameters can be calculated by:

$$\begin{aligned} R &= 0.375\sqrt{\frac{\pi}{m_4}} \\ \eta &= \frac{m_4}{6\pi\sqrt{3}m_2} \\ \sigma_s &= \sqrt{\sigma^2 - \frac{3.717\times10^{-4}}{\eta^2 r^2}} \end{aligned} \tag{4.7}$$

The mean plane of asperity heights is offset from the mean plane of surface heights by y_s (Figure 4.1):

$$y_s = 4\left(\frac{\sigma^2}{\pi\alpha}\right) \tag{4.8}$$

where α is called the bandwidth parameter and is given by [81]:

$$\alpha = 2412.74(\sigma R\eta)^2 \tag{4.9}$$

Chang, Etsion and Bogy later extended this model from the pure elastic contact case to the elastic-plastic contact case. Furthermore, they proposed a full model in a series of three papers [87-89], which include the contact load that is related to the true contact area, the intermolecular force (adhesion) that is related to the strength of the bond formed at the interface and the tangential (friction) force needed to shear the contact. This model is later referred to as the CEB model. For the contact load, the Hertz profile is assumed for both elastic and plastic contact. However, a new interference ω' is defined to replace ω in (4.1) when $\omega > \omega_c$:

$$\omega' = \omega(2 - \frac{\omega_c}{\omega}) \tag{4.10}$$

to account for the volume conservation in plastic flow. ω_c in (4.10) is a critical interference corresponding to the inception of plastic deformation, and it is given by:

$$\omega_c = (\frac{\pi KH}{2E})^2 R \tag{4.11}$$

where H is the hardness of the material and K is the hardness coefficient.

The static friction coefficient, μ, in this model is defined as:

$$\mu = \frac{Q}{F_c - F_s} \tag{4.12}$$

where Q is the tangential force necessary to shear the junctions between the contacting asperities and F_s is the adhesion force acting between the contacting surfaces. By using von Mises yield criterion, the tangential force $\bar{Q}$ at a single asperity can be written as:

$$\bar{Q} = \bar{F}_c f(\frac{\omega}{\omega_c}, \nu) \tag{4.13}$$

where ν is the Poisson's ratio and f is dependent on the failure inception location and is given by equation (20) and (25) in Chang, et. al. (1988b) for yielding below the surface and on the surface, respectively. Following the same approach, the total tangential force Q is given by:

$$Q(d) = N\int_d^{d+\omega_c} \bar{Q}(u-d)\phi(u)du \tag{4.14}$$

The adhesion force between two contacting surfaces is assumed to be governed by a Lennard-Jones potential and the attractive pressure is therefore given by [90]:

$$p(Z) = \frac{8}{3}\frac{\Delta\gamma}{\varepsilon}[(\frac{\varepsilon}{Z})^3 - (\frac{\varepsilon}{Z})^9] \tag{4.15}$$

where ε is the intermolecular distance, Z is the separation of the two contacting surfaces and Δγ is the adhesion surface energy, which is defined by:

$$\Delta\gamma = \gamma_1 + \gamma_2 - \gamma_{12} \tag{4.16}$$

where γ_1 and γ_2 are the surface energies of the two mating surfaces before contact, γ_{12} is the energy of the interface between them after contact.

Considering a spherical asperity in contact with a flat, the adhesion force before contact ($u < d$) is the integrated attractive pressure over the spherical profile and can be written as:

$$\bar{F}_s = \frac{8}{3}\pi R\Delta\gamma[(\frac{\varepsilon}{Z_0})^2 - 0.25(\frac{\varepsilon}{Z_0})^8] \tag{4.17}$$

where Z_0 is the shortest distance between the spherical surface and the flat, and is given by:

$$Z_0 = d - u + \varepsilon \tag{4.18}$$

Accordingly, when the spherical asperity comes into point contact with the flat ($u = d$), by substituting $Z_0 = \varepsilon$ into (4.17), we have:

$$\bar{F}_s = 2\pi R\Delta\gamma = F_0 \tag{4.19}$$

When the two surfaces come into contact as shown in Figure 4.2 ($u > d$), the adhesion force equals to the attractive pressure integrated outside the contact region. The deformed profile outside the contact region is Hertzian. Thus, the separation outside the contact region Z is given by:

$$Z(r) = \frac{1}{\pi R}[a(r^2 - a^2)^{1/2} - (2a^2 - r^2)\tan^{-1}(\frac{r^2}{a^2} - 1)^{1/2}] + \varepsilon \tag{4.20}$$

where a is the radius of the contact region and is given by:

$$a = (\omega R)^{1/2} \tag{4.21}$$

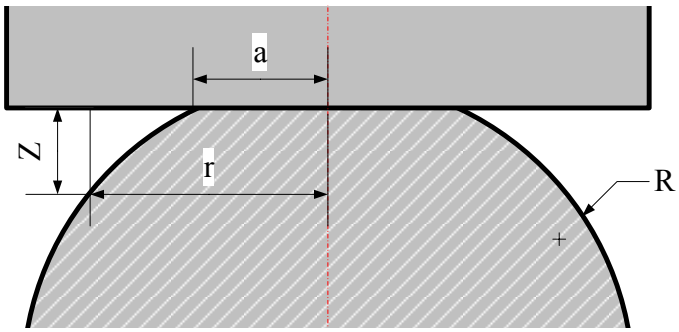

Figure 4.2 Contact between a rigid flat and a spherical asperity. The sphere is deformed under contact and its profile is Hertzian.

Thus the adhesion force occurring between the deformed asperity and the flat is calculated by substituting (4.20) into (4.15) and integrating from a to infinity:

$$\bar{F}_s = 2\pi\int_a^\infty p(Z(r))rdr \tag{4.22}$$

Now by applying the multi-asperity approach, we can write the total adhesion force occurring between the two contacting surfaces as:

$$F_s(d) = N\int_{-\infty}^{\infty} \bar{F}_s(u-d)\phi(u)du \tag{4.23}$$

Stanley et. al. [81] later extended this model to the sub-boundary lubrication case, in which an extremely thin layer of lubricant is applied to the surface for protective purposes. The lubricant layer is assumed to be totally conforming to the solid surface topography, thus it has the same topography parameters, namely, σ, *R*, and η, as the solid surface, and its thickness *t* is much smaller than *R*. When two surfaces come into contact, it is assumed that asperities penetrate and displace the lubricant. Therefore, the contact load and tangential forces remain the same as the dry contact case, i.e., (4.2) and (4.14) remain valid for the sub-boundary lubricated case. For the adhesion force, the lubricant thickness *t* is introduced to rewrite (4.22) as:

$$F_s(d,t) = N\int_{-\infty}^{\infty} \bar{F}_s(u-d+t)\phi(u)du \tag{4.24}$$

Specifically, for the non-contact case ($u < d - t$), the adhesion force at a single asperity is integrated to give:

$$\bar{F}_s = \frac{8}{3}\pi R\Delta\gamma[(\frac{\varepsilon}{Y_0})^2 - 0.25(\frac{\varepsilon}{Y_0})^8] \tag{4.25}$$

where Y_0 is defined as:

$$Y_0 = d - u - t + \varepsilon \tag{4.26}$$

and Δγ is the adhesion energy corresponding to the lubricated surfaces, which is usually smaller than the value for the dry contact case.

When $d - t \le u \le d$, only lubricant-contact occurs in this interface and the sphere asperity is not deformed. For a truncated sphere in contact with a flat, it was shown by Pashley [91] that the integration is equal to that of a sphere in point contact with a flat. Therefore, by substituting $Y_0 = \varepsilon$ into (4.25), we obtain for the lubricant-contact case:

$$\bar{F}_s = 2\pi R\Delta\gamma = F_0 \tag{4.27}$$

For the $u > d$ case, as shown in Figure 4.3, the deformation profile remains the same and the local separation $Y(r)$ is written as:

$$Y(r) = \frac{1}{\pi R}[a(r^2 - a^2)^{1/2} - (2a^2 - r^2)\tan^{-1}(\frac{r^2}{a^2} - 1)^{1/2}] - t + \varepsilon \tag{4.28}$$

Accordingly, the adhesion force is calculated by integrating the adhesive pressure outside the contact region, and it is given by:

$$\bar{F}_s = 2\pi\int_{r_t}^{\infty} p(Y(r))rdr \tag{4.29}$$

Note that the lower limit of this integration is r_t which is the radius where the lubricant layer separates. r_t is obtained by solving the equation:

$$\frac{1}{\pi R}[a(r_t^2 - a^2)^{1/2} - (2a^2 - r_t^2)\tan^{-1}(\frac{r_t^2}{a^2} - 1)^{1/2}] = t \tag{4.30}$$

Here we assume that the volume of the displaced lubricant is negligible, and it does not cause any significant changes in the overall lubricant thickness *t*.

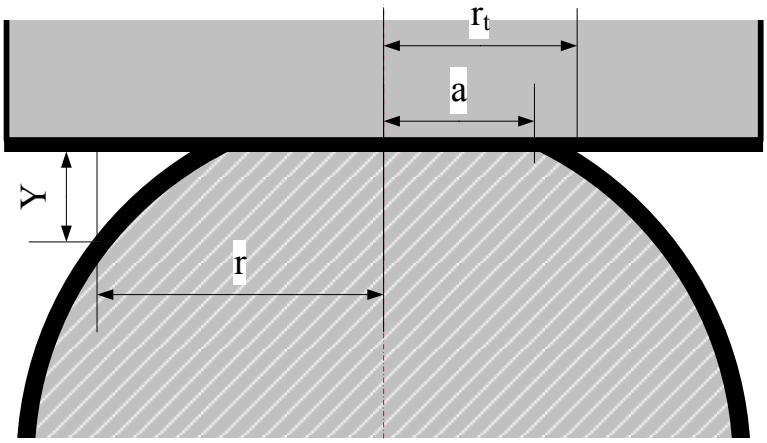

Figure 4.3 Lubricated contact between a rigid flat and a spherical asperity. The sphere is deformed under contact and its profile is Hertzian. The lubricant is conforming to the solid surface. The separation is reduced by t due to the existence of the lubricant layer.

In addition to the contact, adhesion and friction forces arising at small clearances, the electrostatic force also comes into play due to the tribo-charge phenomenon [92, 93]. Because of its attractive nature and fast increase with spacing reduction, the electrostatic force is also considered to have important contributions to the slider's touchdown dynamics. Knigge et. al. [93] experimentally verified that a ~0.5 v potential difference can exist between the head and disk surfaces, which can lead to a significant electrostatic force. The attractive pressure due to electrostatic force is given by:

$$p(Z) = \frac{\varepsilon_0 k_e V^2}{2Z^2} \tag{4.31}$$

where ε_0 and k_e are the permittivity constant and the dielectric constant of the medium between the two surfaces, V is the potential difference between the two surfaces, and Z is the distance between the two surfaces. By integrating $p(Z)$ over a sphere profile, we obtain the electrostatic force between a sphere and a flat as:

$$\bar{F}_{es} = \pi \varepsilon_0 k_e V^2 \frac{R}{d-u-t} \tag{4.32}$$

Assuming that the electrostatic force vanishes at contacting asperities and following the multi-asperity approach as before, we obtain the total electrostatic force as:

$$F_{es}(d,t) = N \int_{-\infty}^{d-t} \bar{F}_{es}(u-d+t)\phi(u)du \tag{4.33}$$

4.3 Air bearing pressure solution at and beyond touchdown

For a flying air bearing slider, the air bearing pressure generated in the head disk interface is governed by the non-dimensional, time-varying Reynolds equation [20]:

$$\frac{\partial}{\partial X}[\hat{Q}PH^3 \frac{\partial P}{\partial X} - \Lambda_x PH] + \frac{\partial}{\partial Y}[\hat{Q}PH^3 \frac{\partial P}{\partial Y} - \Lambda_y PH] = \sigma \frac{\partial}{\partial T}[PH] \tag{4.34}$$

where σ is the squeeze number defined by:

$$\sigma = \frac{12\mu\omega L^2}{p_a h_m^2} \tag{4.35}$$

$\hat{Q}$ is the Poiseuille flow factor which reflects the type of the slip boundary conditions applied. Here we use the slip correction developed by Fukui and Kaneko:

$$\hat{Q} = f(\frac{K_n}{PH}) \tag{4.36}$$

where $K_n = \lambda / h_m$ is the Knudsen number and f is given by Fukui and Kaneko [23].

Hu [94] implemented a numerical approach to solve (4.34) for a flying air bearing slider by discretizing (4.34) using Patankar's control volume method [25]. However, a solution of (4.34) is no longer available when the spacing H becomes zero or negative at contact conditions. Instead of re-formulating the boundary conditions at the contact regions and solving (4.34) at discrete non-contact regions, which can increase the computation cost, we follow an alternative and simpler approach, known as the multi-asperity approach, which we used to model the interfacial forces. Assuming that no air molecules can exist in a clearance less than the diameter of the air molecule ε_0, and calculating h from the mean plane of surface heights of the lubricant layer (because the lubricant also bears pressure), we obtain a modified spacing $\bar{h}$ which considers the asperities' contributions to the head disk clearance and is given by:

$$\bar{h} = \int_{-\infty}^{h-y_s-t-\varepsilon_0} (h - t - y_s - \varepsilon_0)\phi(u)du \tag{4.37}$$

In (4.37) by integrating over the interval $(-\infty, h - y_s - t - \varepsilon_0)$, $\bar{h}$ is always above zero, thus air molecules can always enter into this spacing and provide pressure. By the property of the Gaussian function $\phi(u)$, $\bar{h}$ is equal to h at a larger spacing and approaches zero as h goes to negative infinity. By replacing h with $\bar{h}$ in (4.34), we can solve (4.34) even at negative spacing and simultaneously, the further squeezing of the air film at touchdown can be modeled.

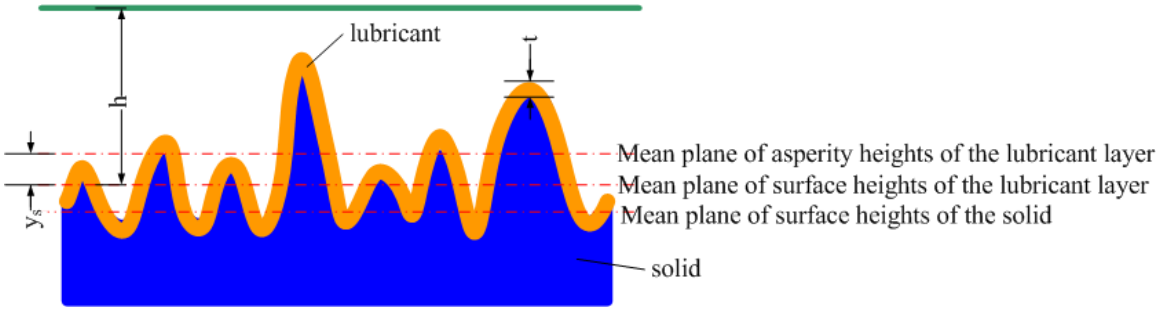

Figure 4.4 Calculation of spacing (flying height) in the head disk interface. The spacing is calculated from the mean plane of surface heights of the lubricant layer, because the lubricant layer also bears pressure.

Now consider a small area $dxdy$ with a spacing h that is already in contact, only at asperities with u less than $(h - y_s - \varepsilon_0 - t)$ will the pressure be generated. To take the pressure loss at higher asperities into account, a coefficient C defined by:

$$C = \int_{-\infty}^{h-y_s-t-\varepsilon_0} \phi(u)du \tag{4.38}$$

is introduced. By the property of the Gaussian function $\phi(u)$, C is roughly equal to 1 at a larger spacing and approaches zero as the spacing goes to negative infinity. The total air bearing force acting on $dxdy$ is then adjusted by C and is given by:

$$F_a = C \cdot p(x,y) \cdot dxdy \tag{4.39}$$

4.4 Inclusion of suspension dynamics

The forces and torques experienced by an air bearing slider during touchdown is schematically shown in Figure 4.5. The dynamics equation of the system at touchdown can be written as:

$$[M]\ddot{\underline{X}} + [C]\dot{\underline{X}} + [K]\underline{X} = \underline{F}_a + \underline{F}_i + \underline{F}_{su} \tag{4.40}$$

where [M], [C] and [K] are the mass, damping and stiffness matrices of the dynamic system, $\underline{X}$ is the displacement vector, $\underline{F}_a$ represents the air bearing forces and moments exerted on the slider, $\underline{F}_i$ denotes the interfacial forces and moments applied on the slider, and $\underline{F}_{su}$ is the preload of the suspension.

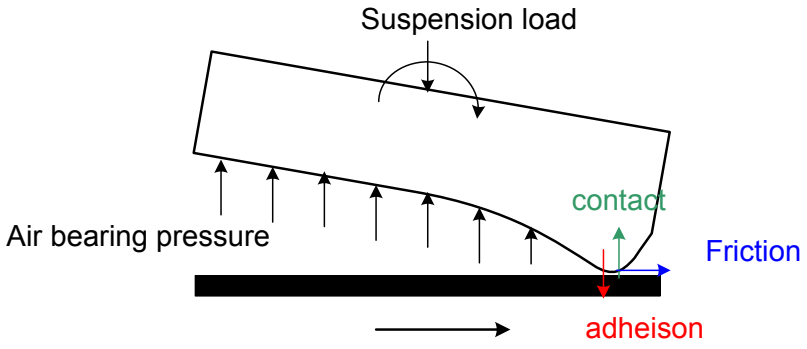

Figure 4.5 Forces and torques acting on a TFC slider during touchdown

The most common approach is to treat the slider as a rigid body having three degrees of freedom, the flying height, pitch and roll. The suspension is usually modeled as a massless spring with the same three degrees of freedom. Accordingly, in (4.40) $\underline{X}=(z,\theta,\varphi)^T$, where z is the vertical displacement of the slider, θ and φ are the pitch and roll angles; $[M]=diag(m, I_\theta, I_\varphi)$ where m is the slider's mass, I_θ and I_φ are the moments of inertia of the slider; $[C]=diag(c_z, c_\theta, c_\varphi)$ where c_z, c_θ, c_φ are the suspension's damping coefficients in the vertical, pitch and roll directions; $[K]=diag(k_z, k_\theta, k_\varphi)$ where k_z, k_θ, k_φ are the suspension's stiffness in the vertical, pitch and roll directions.

However, recent experiments have shown that the suspension can have substantial vibrations during touchdown that interact significantly with the air bearing slider [95, 96]. Thus a simple model that does not consider the suspension mass is not capable of capturing important details of the slider's touchdown dynamics, specifically, the vibration modes of the slider during touchdown. In this section, we expand the simplified suspension model in [97] by using finite element (FE) modeling and reduction techniques.

A three dimensional FE suspension model with a femto-sized slider attached is first reduced to a 250-DOF mass-spring system with a mass matrix $[M]_{red}$ and a stiffness matrix $[K]_{red}$ using the reduction technique [98]. After the reduction process, the vibration modes up to 150 kHz are retained from the original model and the relative error of frequencies is found to be within 10% of the results from modal analysis on the full FE model. Assuming proportional damping, the damping matrix $[C]_{red}$ of this reduced model can be computed as:

$$[C]_{red} = \alpha_1[M]_{red} + \alpha_2[K]_{red} \tag{4.41}$$

where the coefficients α_1 and α_2 are chosen such that the damping values at 10 Hz and 50 kHz are 2%. In this way, the original 3-DOF dynamics equation is now expanded to 250-DOF dynamics equation, which is solved at each time step so that the suspension-slider interactions can be captured throughout the simulation:

$$[M]_{red}\ddot{\underline{X}} + \dot{\underline{X}} = \underline{F}_a' + \underline{F}_i' + \underline{F}_{su}' \tag{4.42}$$

On the right side of (4.42), the suspension preload $\underline{F}_{su}'$ is given. The air bearing lift force $\underline{F}_a'$ is obtained by solving the air bearing pressure using the procedure elaborated in section 4.3 and integrating the pressure over the entire air bearing surface. The interfacial force $\underline{F}_i'$ is obtained by implementing the sub-boundary lubrication model elaborated in section 4.2. The interfacial pressures are calculated at each grid point and integrated over the entire air bearing surface to get $\underline{F}_i'$. In the application it is very time-consuming to carry out all integrations listed in section 4.2 on each grid point. Alternatively, we normalized formulas derived in section 4.2 and then tabulated the interfacial pressure occurring at a certain normalized spacing (d / σ) for a given interface profile, i.e., a given set of {σ, *R*, η, *t*}, before solving (4.42). In the process of solving (4.42), we refer to the pre-calculated table and use linear interpolation and extrapolation to get the interfacial pressure occurring at a grid point. Figure 4.6 shows this table graphically by plotting the normalized interfacial forces (contact, adhesion, electrostatic and friction) against the normalized separation d/σ for the case {σ, *R*, η, *t*} = {0.501 nm, 0.5 μm, 159.68 μm^{-2}, 1.2 nm}. It can be seen that the electrostatic force is the dominant one for a separation *d* greater than 6σ, because compared with other forces the electrostatic force varies with the spacing on the order of $1/d^2$. Below 6σ, the adhesion force starts increasing rapidly as d decreases. The rate of increase goes up, reaches a maximum, remains constant for a while and then decreases. The segment where the adhesion force grows with the fastest rate is between ~5σ and ~3σ, which roughly corresponds to the region where the spherical asperity is contacting with the lubricant layer. When the separation *d* is further reduced below 3σ, the contact and friction forces become dominant due to the occurrence of solid contact. It is also noted that electrostatic force vanishes at very small separation, showing the effect of assuming no potential difference at contacting asperities. More details of the effects of different interface parameters on the interfacial force curves will be discussed in Chapter 6.

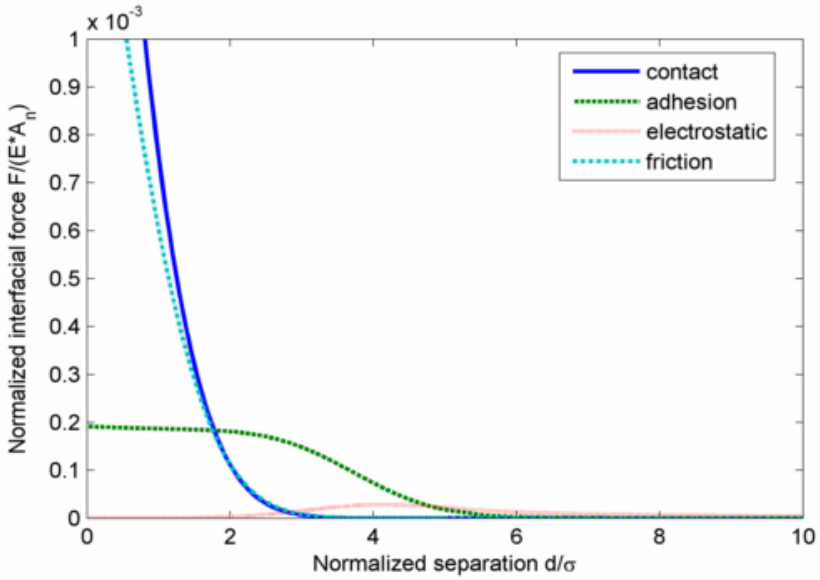

Figure 4.6 Normalized interfacial forces $F/(E \cdot A_n)$ varying with the normalized separation d/σ for the case $\{\sigma, R, \eta, t\} = \{0.501 \text{ nm}, 0.5 \text{ μm}, 159.68 \text{ μm}^{-2}, 1.2 \text{ nm}\}$. The electrostatic force is calculated based on a potential difference of 1 v between the head and disk.

The slider's dynamics is solved by employing the Newmark-beta method [99] because of its high accuracy and less frequency distortion as compared with other commonly used methods [94]. It is noted that the dynamics equation (4.42) is coupled with the generalized Reynolds equation (4.34), which means these two equations have to be solved simultaneously. The numerical procedure starts from estimating the slider's displacement based on the velocities and accelerations of the previous time step. The estimated displacements are used for calculating the external forces acting on the slider, and based on the calculated external forces, we are able to update the slider's displacements at this time step. These updated displacements are then compared with the results from the previous iteration step. The iteration ends when the maximum relative change of displacements is less than a certain number, and these displacements are taken as the displacement solution of the slider at this time step.

To bring the slider from a flying state to touchdown we need a time-varying actuation profile as the input to modify the air bearing geometry at each time step. The protrusion geometry at a given heating power can be obtained by using the approach elaborated in Chapter 2. However, it is costly to conduct a full steady-state TFC analysis for every heating power applied during touchdown. Here we start from a protrusion geometry obtained at a certain heating power and call it the base geometry. A time-varying profile is used as an input to specify how the peak protrusion on the TFC bulge changes with time. Then we simply assume that the protrusion at points other than the peak point increase proportionally with the peak protrusion. The protrusion geometry is updated this way at every time step during the dynamic simulation [97].

The slider is subject to continuous disturbances due to the rotation and the uneven profile of the disk. This disturbance results in energy exchange between the disk and the slider, and it can lead to very different flying height modulation amplitudes during

touchdown, as will be discussed later. To simulate such an effect, a point-by-point disk profile is used as an input and rotated with the disk during the dynamic simulation [100].

4.5 Summary and conclusion

A numerical model for predicting a TFC slider's dynamics at touchdown and over-pushed conditions are developed and implemented in this chapter. The various interfacial forces which are considered to have significant contributions to a slider's touchdown dynamics are modeled by carefully following the asperity approach used in the Greenwood-Williamson contact model. This approach is also applied to treat the head disk spacing loss at contact regions and extend the solution of the generalized Reynolds equation to the touchdown and over-pushed regions. A slider touchdown simulation program is then implemented based on the original CML dynamic simulation program. This simulation program greatly improves the capability of the CML dynamic simulator and makes it possible to correlate numerical results with touchdown experimental studies, which are key studies to guarantee today's magnetic heads' performance with a nanometer clearance. Furthermore, it also makes it possible to conduct various parametric studies regarding ABS features, heater geometries, suspension designs, etc.. These studies should be able to facilitate the design and optimization process for head disk interface engineers.

Chapter 5

Instability of TFC slider touchdown dynamics

5.1 Introduction

Touchdown dynamics of TFC sliders has received much attention because it is concerned with the flying-height limit of flying sliders, and it is also related to the feasibility of a contact recording slider [101-110]. Experiments have shown that TFC sliders often experience relatively large bouncing vibrations at air bearing frequencies when the power supplied to the heating element is increased beyond a critical point, which is usually termed the "touchdown" power. Such vibrations can get damped out when the slider is over-pushed by even higher heating power [71, 95, 96, 111-115].

The phenomenon of bouncing vibrations has been studied extensively using numerical methods. Ono and Yamane used a 2-DOF mass-spring system to approximate the slider air bearing and consider the contact, friction and meniscus forces occurring at near-contact or contact conditions and attributed bouncing vibrations to meniscus force and friction occurring at contact conditions [65, 66]. It is noted that in this model there is no moving waviness applied on the disk thus both meniscus and friction forces are displacement-related forces. Therefore the bouncing vibration seen in this numerical model loses its physical energy source and is probably a numerical phenomenon. This point is also argued in a later paper by Chen and Bogy [116]. Alternatively, Chen and Bogy proposes and proves that bouncing vibrations are forced vibrations by moving disk waviness and roughness. But this numerical model used a non-TFC slider and cannot predict the damping out of bouncing vibrations at over-pushed conditions which are often observed in TFC sliders. By using a 2-DOF mass-spring model similar to Ono's model, considering effects of interfacial forces and including a dynamic micro-waviness, Polycarpou et. al. [71, 74] was able to predict the excitation and damping-out of bouncing vibrations from their numerical simulations and attributed this phenomenon to strong adhesive forces at the near-contact region. However, they did not give any specifics of excited dynamics on the slider at bouncing thus they cannot directly associate their numerical simulations with experiments.

In this chapter we use the numerical simulator developed in Chapter 4 to study a TFC slider's touchdown dynamics. A time-varying heater-induced protrusion profile is used to reduce the slider's flying height and induce touchdown. A full finite element model of a head-gimbal assembly is reduced to a 250-degree-of-freedom (250-DOF) mass-spring system, and the dynamics equation of this system is solved at each time step. Simulation results show similar trends at touchdown to what has been seen in experiments [111, 114]. The inclusion of the suspension dynamics in the numerical model is shown to be important for determining the frequencies and nodal lines of the excited vibration modes during touchdown. Also, different interfacial forces (adhesion, friction, electrostatic) are shown to contribute in quite different ways to the slider's dynamics at touchdown. Section 5.2 gives details about the simulation setup. Section 5.3 discusses a typical

touchdown process of a TFC slider. Effects of suspension mass, stiffness and each interfacial force are discussed in Sections 5.4 and 5.5 respectively.

5.2 Simulation setup

An industry designed femto-sized slider is subject to the TFC touchdown dynamics study [40]. The base geometry of the bulge profile is shown in Figure 5.1 where the peak protrusion is 10 nm. By specifying how the peak protrusion varies with time, this base geometry is scaled proportionally to change the air bearing surface geometry. The disk rotates at 5400 rpm and the slider flies at an inner radius of 18.5 mm. Figure 5.2 shows the point-by-point disk profile used in the current simulation which is a measured profile using LDV (Laser Doppler Vibrometer) and has a length of approximately 18 mm [83]. The roughness parameters as listed in Table 5.1 are taken from [70], where they are based on atomic force microscopy images of slider and disk surfaces.

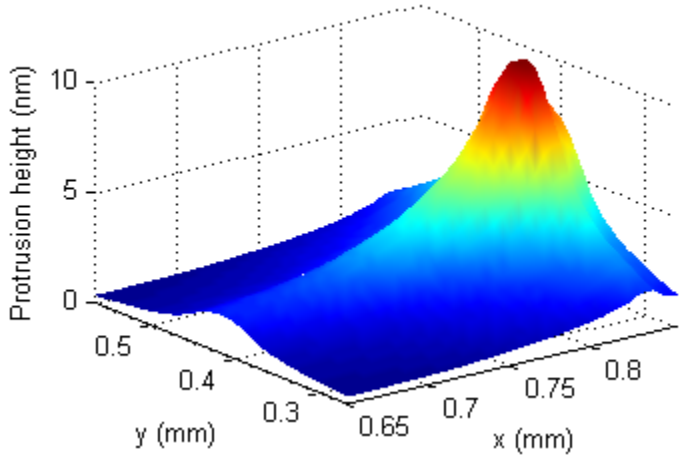

Figure 5.1 Base geometry with a peak protrusion equal to 10 nm for the TFC touchdown dynamics study.

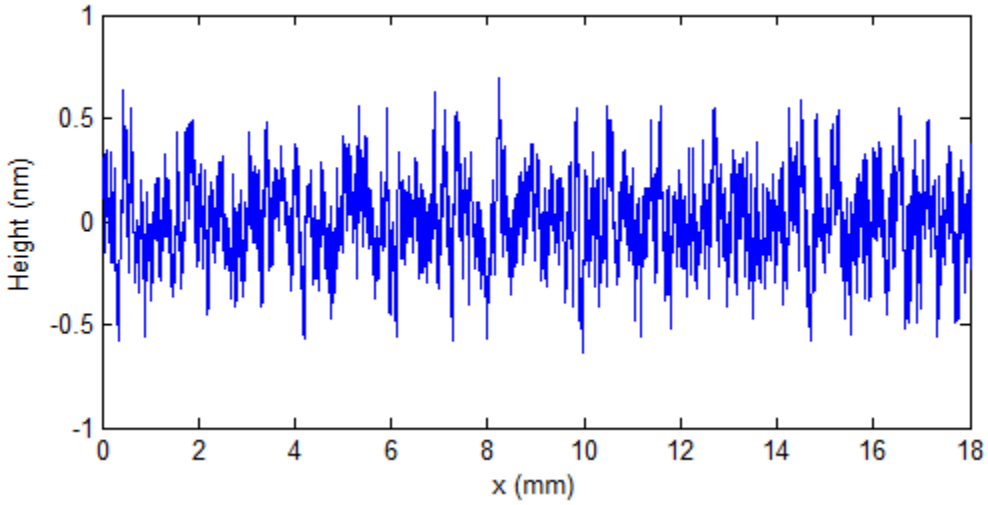

Figure 5.2 Point-by-point disk profile. The total length is approximately 18 mm.

Table 5.1 Interface parameters used for the TFC touchdown dynamics study

Lubricant thickness t (nm)	1.5
Surface adhesion energy $\Delta\gamma$ (N/m)	0.055
Disk Young's modulus (GPa)	280
Slider Young's modulus (GPa)	280
Disk Poisson ratio	0.24
Slider Poisson ratio	0.24
Disk hardness (GPa)	13
Combined standard deviation of surface heights σ (nm)	0.654
Combined mean radius of curvature R (μm)	6.384
Combined asperity density η (μm^{-2})	9.871
Diameter of an air molecule (nm)	0.3
Potential difference between the head and disk (v)	0.5

5.3 Unstable dynamics of a TFC slider at touchdown

As shown in Figure 5.3 a ramping-up actuation signal ranging from 18 nm to 30 nm is applied to actuate the slider from flying to touchdown, and the flying-height modulation at the read transducer location is plotted as a function of time. The vibration amplitude of the slider shows a non-monotonic trend: it starts increasing rapidly at about 1.2 ms, remains high between 1.5 ms and 2 ms, and then gets suppressed under further protrusion. Here, we designate the actuation range where the slider's vibration amplitude becomes obviously larger as the instability region.

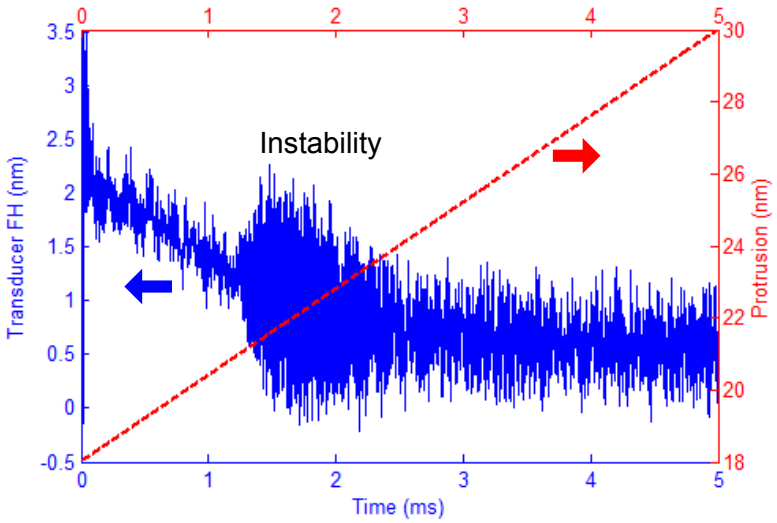

Figure 5.3 Heater induced protrusion (dashed) and transducer's FH (solid) as functions of time. An instability region where the slider experiences stronger vibrations exists at a certain protrusion range.

To show the slider's contact status with the disk during this process, we plotted the history of the contact force in Figure 5.4. The contact force remains at zero at the beginning time steps and then it becomes non-zero at around 1.2 ms. If we consider the occurrence of a positive contact force as the sign of touchdown and compare Figure 5.4

with Figure 5.3 we conclude that the instability occurs at the beginning of touchdown. Between 1.2 ms and 2.5 ms the contact force oscillates between positive values and zero, which means that the slider comes into contact and then bounces off the disk. Throughout the instability region the slider's motion is characterized by this intermittent slider-disk contact. Beyond 2.5 ms, the contact force is always above zero, indicating that the slider is continuously sliding on the disk. We also see that the slider's vibration amplitude at this stage is relatively small.

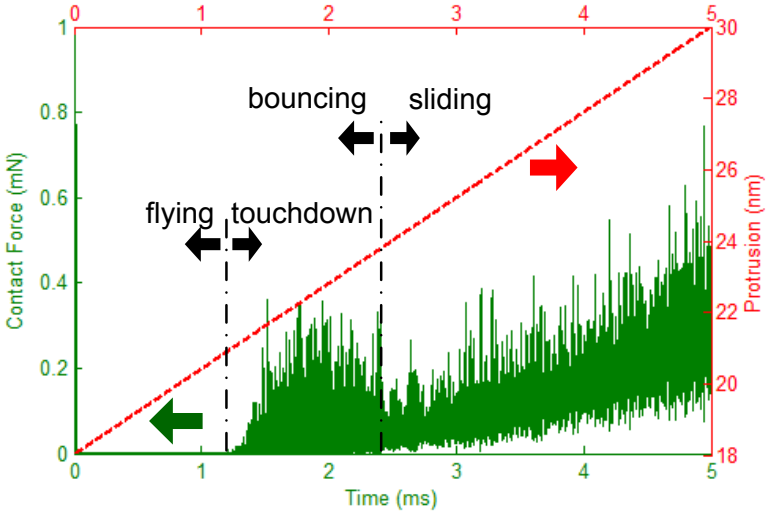

Figure 5.4 Heater induced protrusion (dashed) and contact force (solid) as functions of time. Three regions (flying, bouncing and sliding) can be identified from the contact force history curve. The slider's motion at instability is characterized by strong bouncing vibrations.

To examine the slider's dynamics in the frequency domain we conducted Fourier transforms of the data points over every 0.2 ms band, assuming that the slider's dynamics does not change abruptly within these time intervals. The power spectrum of the transducer's FH is shown in Figure 5.5. An obvious stripe indicating high vibration amplitude is observed at around 280 kHz when the actuation steps are between 20.5 nm and 24 nm. This stripe corresponds to the strong dynamics observed in the time domain (Figure 5.3) and the length of the stripe corresponds to the extent of the instability region. Higher harmonics of this excited mode are also observed at ~560 kHz. It is worth noting that similar frequency peaks have been discovered in touchdown experiments and reported in [96].

Figure 5.6 shows the spectrum of the slider dynamics at 4 actuation steps: 21 nm, 22 nm, 23 nm, and 24 nm. A small peak first appears at 249 kHz at 21 nm actuation, then it moves to 283 kHz at the 22 nm actuation with a much higher amplitude. The peak frequency then increases further to 298 kHz with the peak height substantially reduced at 23 nm actuation. At 24 nm, the peak frequency is even higher and the amplitude is further reduced.

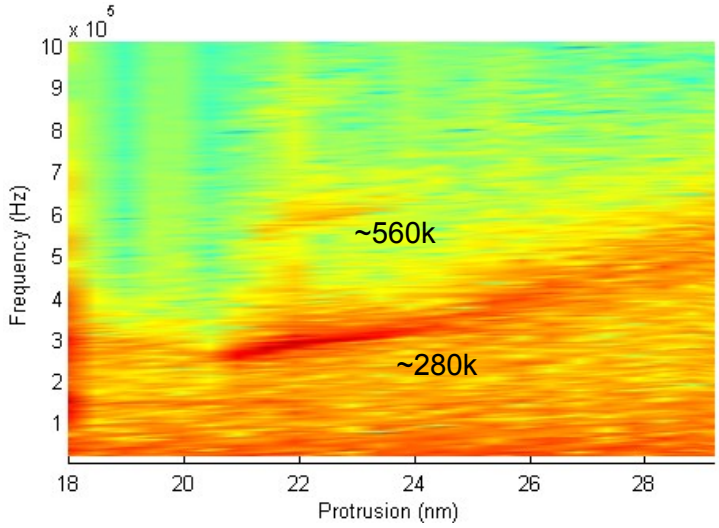

Figure 5.5 Power spectrum of the slider's dynamics during the touchdown process. A mode at ~280 kHz with higher harmonics is excited at instability.

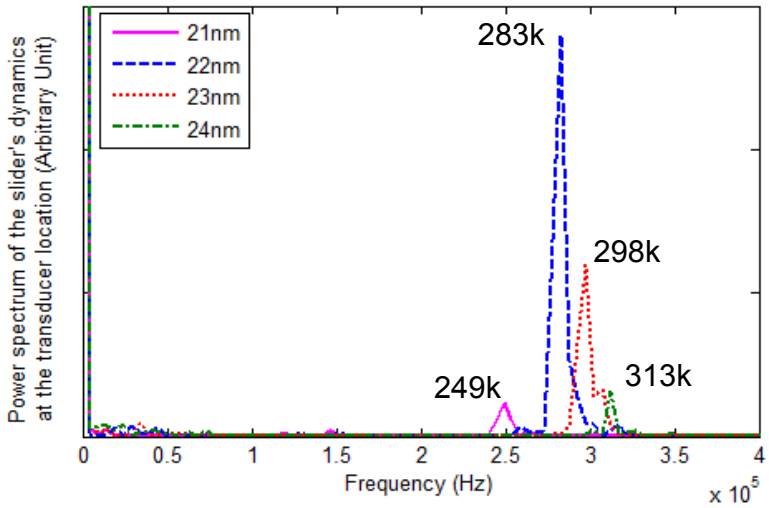

Figure 5.6 Power spectrum of the slider's dynamics at 4 actuation steps: 21 nm, 22 nm, 23 nm and 24 nm. The frequency of the excited mode keeps increasing while the amplitude first increases, then decreases.

To find out the nodal line of each excited mode observed from Figure 5.6, we employ the following approach. We first calculate the flying-height of points along a line, say the slider's y-centerline, and conduct a Fourier transform on the flying-height of each point. By the definition of a nodal line, the flying height of points on the nodal line should have zero amplitude at the frequency of this mode of interest. Thus by determining which point along the line has a minimum amplitude at the frequency of interest, we can identify the intersection point of the nodal line with the current line. By repeating this procedure along lines parallel to the slider's y-centerline, we are able to get a complete nodal line.

As shown in Figure 5.7, all nodal lines are located near the slider's leading edge, thus the excited mode is considered to be the second air bearing pitch mode. With increasing actuation the nodal line moves more toward the trailing edge and the frequency becomes higher. The increase in frequency with higher actuation is considered to be an effect of further compression of the air film at the trailing edge. In addition, assuming the pitch torque applied by the suspension remains essentially constant, to maintain the force balance of the slider, the nodal line has to move toward the trailing edge as the pressure at the trailing edge grows with increasing protrusion.

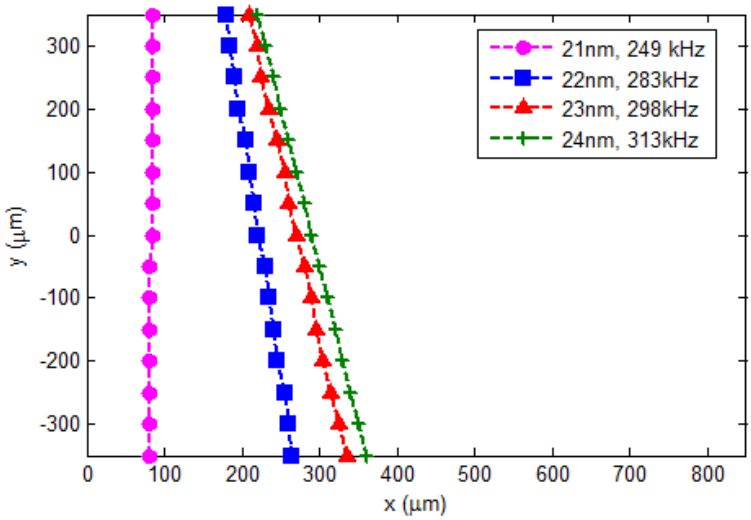

Figure 5.7 Nodal lines of the excited modes observed from Figure 5.6. All nodal lines are located near the leading edge of the slider.

As a summary of this section, the slider can experience several stages during the touchdown process, which are characterized by different dynamics and head-disk contact status. Right before touchdown occurs, the slider barely touches the disk and its dynamics has no obvious excited modes. At the beginning of touchdown, the slider dynamics is characterized by a strong excited mode at the second air bearing frequency and the slider is intermittently contacting the disk. This stage is considered as unstable because the trailing edge of the slider is vibrating severely thus a stable read/write spacing cannot be achieved. This instability is terminated when we over-push the slider using even higher protrusions. The excited second air bearing mode is damped out and the slider becomes continuously sliding on the disk.

5.4 Effects of suspension mass and stiffness on TFC slider touchdown dynamics

In the current simulation the FE model of the suspension with a rigid slider attached is reduced to a 250-DOF mass-spring system using the method described in [98], and the dynamics of this system is solved at each time step. In this way, the interaction between the suspension and slider can be captured while keeping the problem solvable within a reasonable amount of time. To show the effect of including the suspension mass and stiffness we solved a simplified dynamics equation with the suspension modeled as a massless spring having 3 DOFs in flying-height, pitch and roll directions under the same

actuation profile as used in section 5.3. The transducer's FH history obtained with this simplified procedure is shown in Figure 5.8, and it is compared with the results obtained in section 5.3 in Figure 5.9. An instability region can still be identified for the simpler case; however, the vibration amplitude at instability as well as the extent of the instability region is smaller compared with the 250-DOF case.

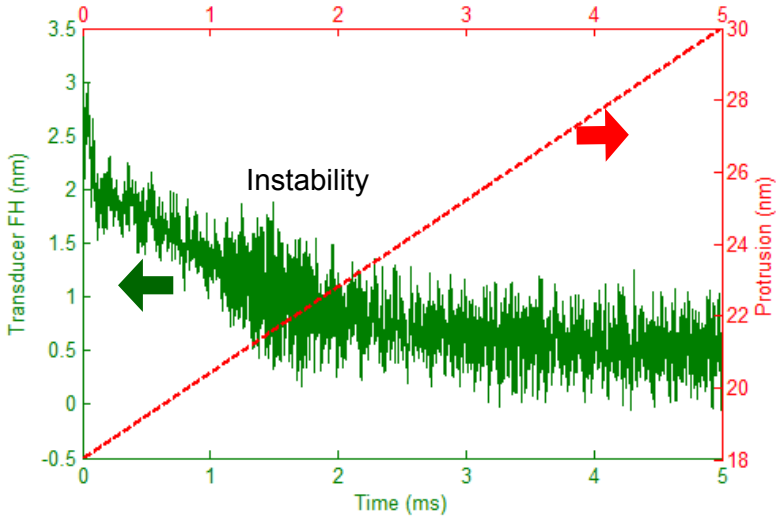

Figure 5.8 Heater induced protrusion (dashed) and transducer's FH (solid) as functions of time. The head-disk-assembly is modeled as a 3-DOF mass-spring system where the suspension is a massless 3-DOF spring. Instability still exists in this case.

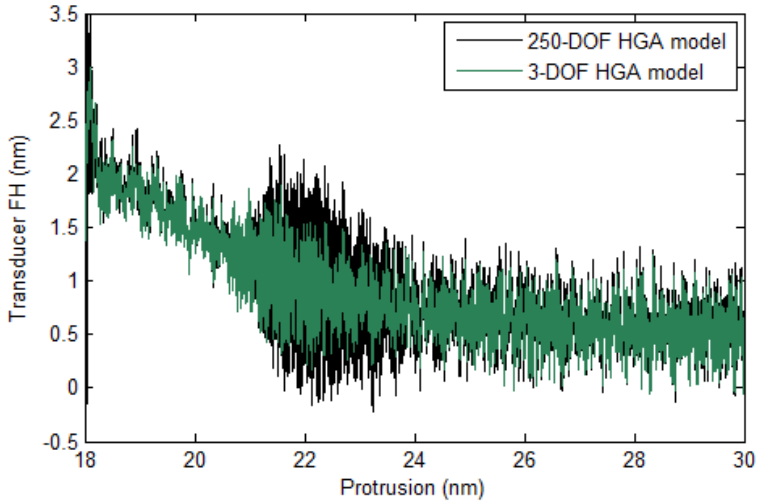

Figure 5.9 Comparing the transducer's FH when HGA is modeled as a 250-DOF and 3-DOF mass-spring system. Both cases have instabilities, but the extent of the instability region and the vibration amplitude at the instability region are greater for the 250-DOF case.

The power spectrum of the slider's dynamics is shown in Figure 5.10. Referring to Figure 5.5 and Figure 5.10 one observes in both the 3-DOF and 250-DOF cases a stripe indicating strong vibrations at certain actuation ranges. However, the vibration frequency for the 3-DOF case is ~370 kHz, much higher than the 250-DOF case, which is ~280 kHz.

The nodal line for the excited mode of 366.2 kHz at about 21nm actuation is shown in Figure 5.10. The location of the nodal line confirms that the excited mode is still the second air bearing pitch mode, although the frequency has increased substantially. Thus, the suspension is actively involved in the air bearing slider vibrations, resulting in a much reduced frequency of the second air bearing mode in the 250-DOF case. Furthermore, when we push the slider beyond the instability region the second air bearing frequency is further raised due to the growing pressure peak at the slider's trailing edge. It goes up to ~500 kHz for the 250-DOF case, much less than ~700 kHz for the 3-DOF case, a frequency much higher than what has been discovered in experiments [111, 114]. Therefore, the inclusion of suspension-slider dynamic coupling is very important for determining the active vibration modes at touchdown and correlating them with experimental results.

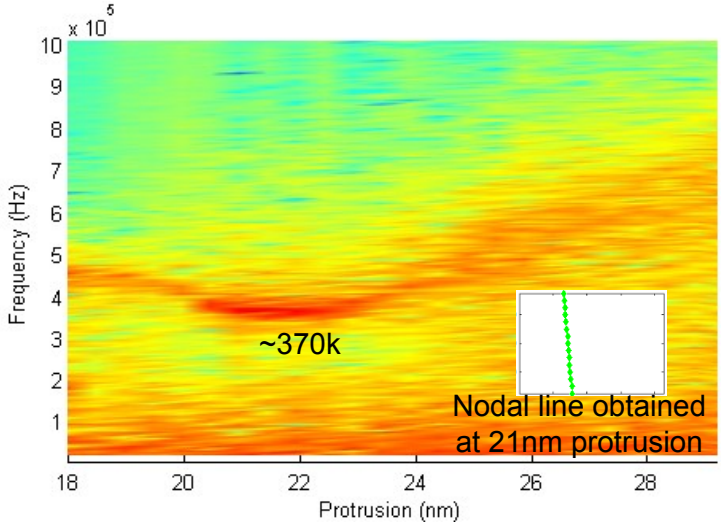

Figure 5.10 Power spectrum of the slider's dynamics for the 3-DOF case. A mode at ~370 kHz is excited at instability, the nodal line of which is located near the leading edge of the slider.

5.5 Effects of interfacial forces on TFC slider touchdown dynamics

The effect of each interfacial force on the slider's touchdown dynamics is investigated using a simplified approach: we set just one of the interfacial forces to zero and then conduct the simulation again by applying the same actuation signal; the results are then compared with those shown in section 5.3, which includes all interfacial forces. The object is to find out how the slider's dynamics differs with and without that force. Three interfacial forces are studied using this approach: adhesion, electrostatic and friction forces.

5.5.1 Adhesion force

The first set of results is obtained by setting the adhesion force equal to zero. In Figure 5.11, we compare the transducer's FH with increasing protrusions obtained with and without adhesion force. One major difference is that the instability region disappears when adhesion force is taken out of the simulation. The vibration amplitude of the slider does not experience any obvious changes throughout the touchdown process for this case. In addition, the FH at the transducer location is slightly higher when the adhesion force is

excluded due to the reduced attractive effect in this case. The power FFT result shown in Figure 5.12 further confirms that no obviously excited modes can be observed when the adhesion force is excluded. This result indicates that adhesion force plays an essential role in causing the touchdown instability.

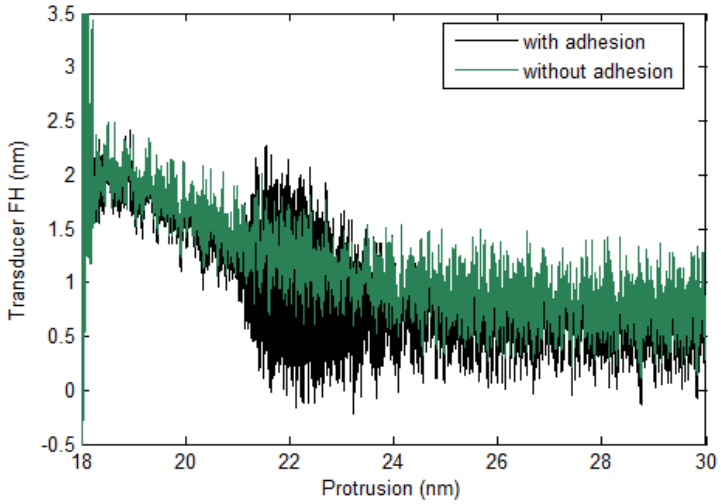

Figure 5.11 Comparing the transducer's FH when adhesion is included in or excluded from the simulation. Instability only occurs in the adhesion-included case.

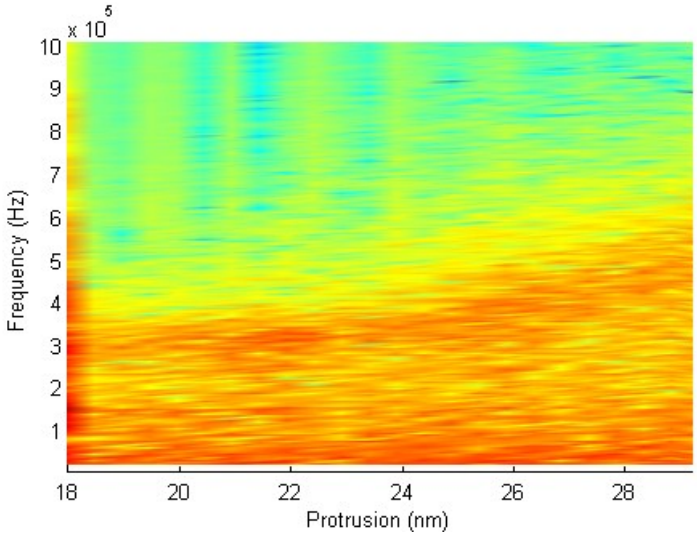

Figure 5.12 Power spectrum of the slider's dynamics for the adhesion-excluded case. No obviously excited modes are observed during touchdown.

5.5.2 Electrostatic force

Figure 5.13 shows the transducer's FH varying with protrusion when the electrical potential difference between the slider and disk is set to zero so that the electrostatic force equals zero in this case. For comparison, the same curve obtained in section 5.3 is also shown in Figure 5.13. An obvious instability region exists in both cases, although the extent of the instability region and the vibration amplitude at instability are greater for the

electrostatic-force-excluded case. Due to the attractive nature of the electrostatic force, at the same actuation, the slider flies at a larger FH when the electrostatic force is excluded, Thus touchdown occurs at a higher actuation value for this case, and so does the instability.

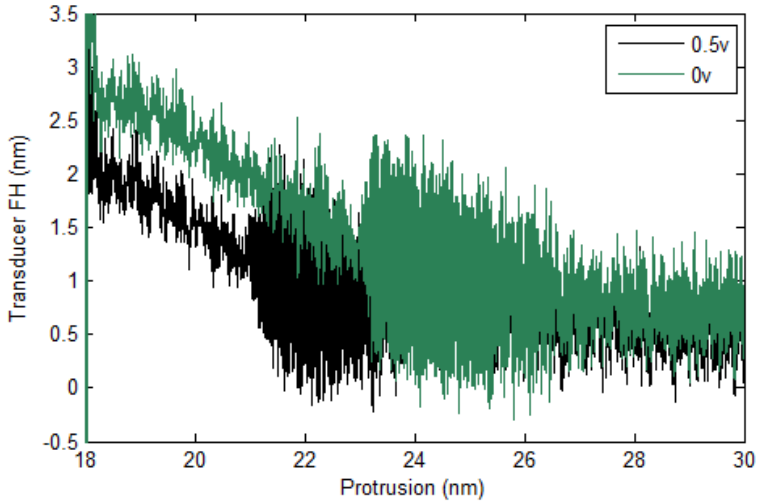

Figure 5.13 Comparing the transducer's FH when electrostatic force is included (the 0.5v case) or excluded (the 0v case). Both cases have instabilities, but the extent of the instability region and the vibration amplitude at the instability region are greater for the electrostatic-force-excluded case.

The power spectrum for the electrostatic-force-excluded case is shown in Figure 5.14, where a stripe is seen at around ~300 kHz. The frequency is slightly higher compared with the case shown in section 5.3, because taking out the electrostatic effect stiffens the head-disk interface. The instability region starts at about 22 nm and extends beyond 26 nm, which is obviously wider than the electrostatic-force-included case (Figure 5.5). The power FFT results for the 4 actuation steps (22 nm, 23 nm, 24 nm, 25 nm and 26 nm) presented in Figure 5.15 show a similar trend in the variation of the excited air bearing mode: the frequency increases monotonically while the amplitude first increases then decreases. It is interesting to note that although the electrostatic force and adhesion force are both attractive they have different and distinct effects on the slider's dynamics: adhesion force is essential in causing instability and exciting the second air bearing pitch mode, while electrostatic force does not determine whether or not instability occurs. Such a difference is attributed to the fact that electrostatic force does not increase as rapidly with spacing reduction as adhesion force at ultra-low clearances. Also, compared with the electrostatic force adhesion force is mostly concentrated at the trailing edge, and thus it is more likely to excite the second air bearing mode. In addition, because of the expanded instability region and increased amplitude at the second air bearing mode in the electrostatic-force-excluded case we conclude that the electrostatic force serves to suppress the slider's dynamics at the second air bearing mode in the studied case.

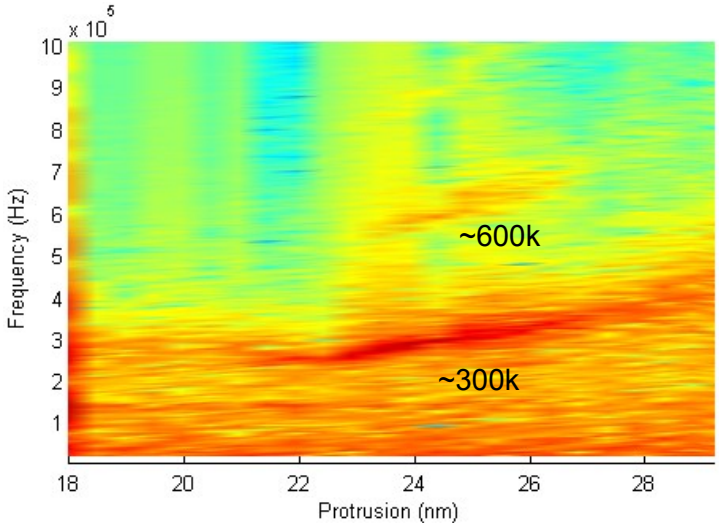

Figure 5.14 Power spectrum of the slider's dynamics for the electrostatic-force-excluded case. A mode at ~300 kHz and its higher harmonics are excited at instability.

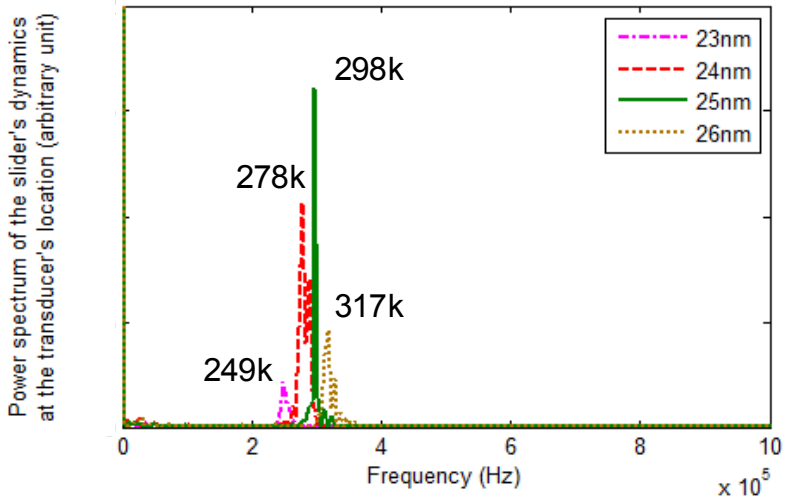

Figure 5.15 Power spectrum of the slider's dynamics at 4 actuation steps: 23 nm, 24 nm, 25 nm and 26 nm, for the electrostatic-force-excluded case. Similar to the electrostatic-force-included case (Figure 5.6), the frequency of the excited mode keeps increasing while the amplitude first increases, then decreases.

5.5.3 Friction force

Figure 5.16 shows plots of the transducer's FH as a function of protrusion when the friction force is turned off in the simulation, and the curve is compared with the one obtained in Section 5.3. Similar to the electrostatic force case, eliminating the friction force does not eliminate the instability. However, the slider actually has a stronger dynamics at the instability region and such instability continues for a wider actuation range. The result in the frequency domain is shown in Figure 5.17 where we observe a longer stripe at ~250 kHz. The spectrums at 21 nm, 22 nm, 23 nm, 24 nm and 25 nm are shown in Figure 5.18, and they show that the nature of the touchdown dynamics does not change: the second air bearing mode gets excited from a certain actuation step and gets

suppressed as the slider goes through even higher actuation. A major difference is that the excited second air bearing mode is stronger and is damped out more slowly, which shows that friction force also suppresses the unstable dynamics at the second air bearing mode. Another observation is that a mode gets excited at around 146.5 kHz, as can be seen from the light stripe in Figure 5.17, as well as the small peak in Figure 5.18. As shown by the nodal line at the slider's trailing edge (plotted in Figure 5.18), this peak is related to the first air bearing mode. This observation implies that the friction force makes contributions to the first air bearing mode, and in this case it suppresses its excitation.

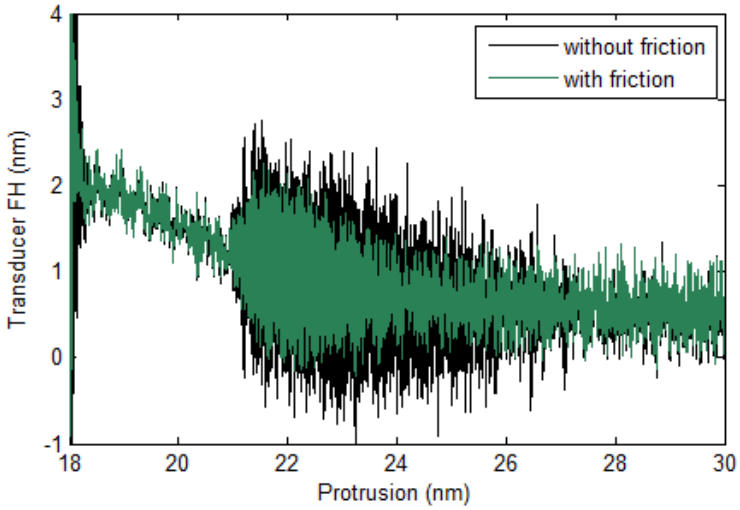

Figure 5.16 Comparing the transducer's FH when friction force is included or excluded. Both cases have instabilities, but the extent of the instability region and the vibration amplitude at the instability region are greater for the 250-DOF case.

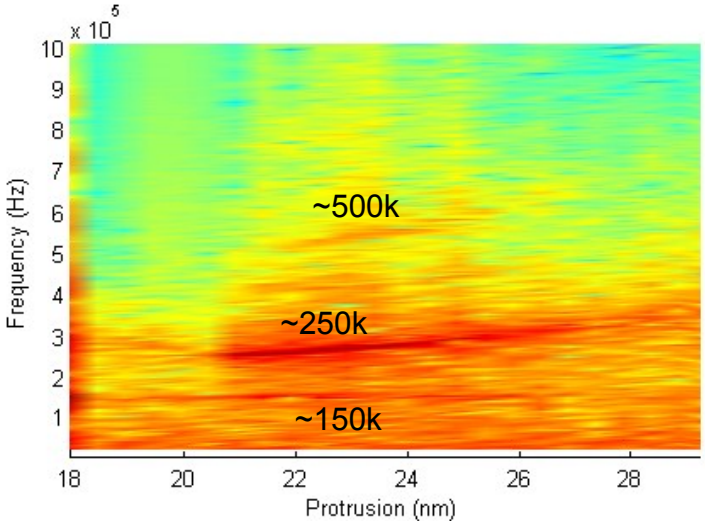

Figure 5.17 Power spectrum of the slider's dynamics for the electrostatic-force-excluded case. A mode at ~250 kHz and its higher harmonics are excited at instability. A mode at ~150 kHz is also excited.

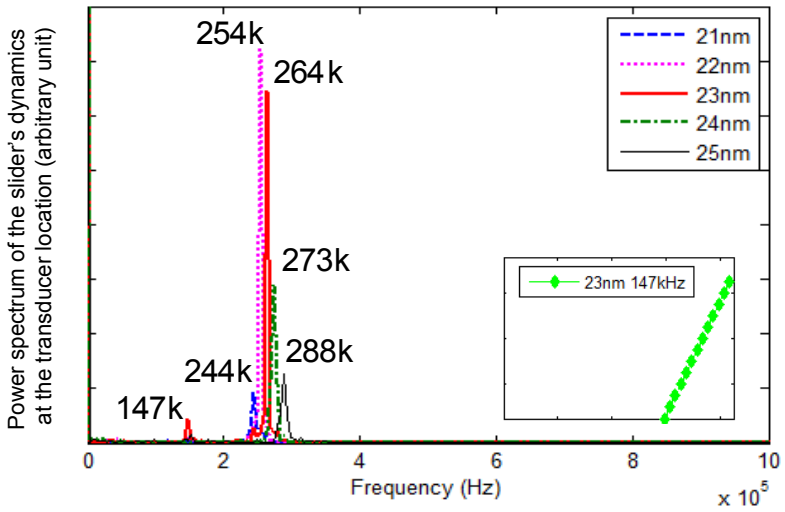

Figure 5.18 Power spectrum of the slider's dynamics at 5 actuation steps: 21 nm, 22 nm, 23 nm, 24 nm and 25 nm, for the friction-excluded case. Similar to the friction-included case (Figure 5.6), the frequency of the excited second air bearing mode keeps increasing while the amplitude first increases, then decreases. A 147 kHz mode with a nodal line located at the slider's trailing edge is also excited.

5.6 Summary and conclusion

In this chapter, we use the numerical approach developed in Chapter 4 to study the touchdown dynamics of TFC sliders. An actuation signal that ramps up with time is applied to bring the slider from flying to touchdown. The slider's flying-height modulation shows that an instability region exists at the beginning of touchdown, where the slider bounces on the disk at the second air bearing pitch frequency. This instability disappears as the slider is brought into even closer contact with the disk with higher actuation.

By simplifying the suspension as a massless, 3-D spring, we found that suspension mass and stiffness play an important role in determining the frequency of the excited second air bearing mode and correlating simulation results with experiments.

By removing from the model one interfacial force at a time, we found that each interfacial force plays a different role in affecting the slider's touchdown dynamics. Adhesion force is essential for causing touchdown instability and exciting the second air bearing mode, while electrostatic force and friction force only have minor effects in the slider's pattern of motion at instability. In this case study, both electrostatic force and friction force suppress the excited air bearing mode and enhance the termination of instability. Friction force also serves to suppress the excitation of the first air bearing mode.

Chapter 6

TFC dynamic touchdown patterns

6.1 Introduction

In the previous chapter we used numerical simulations to study different head disk interface factors and their individual contributions to a TFC slider's touchdown dynamics. It was found that different interfacial forces play quite different roles in affecting the slider's dynamics. Because interfacial forces are contingent upon specific interface properties, such as the roughness of the interface σ and the lubricant thickness *t*, it is expected that the slider's touchdown dynamic pattern varies under different interface conditions. Experimentally, even for the same design, the head can perform in very different ways when flying over disks of different roughness and lubricant thickness, which also suggests the importance of the interface design to the head's performance and reliability. Thus, optimizing the head disk interface is always among the most important design tasks in the modern hard disk drive industry [102, 117-124].

The numerical approach developed in Chapter 4 accommodates a complicated setup, which enables parametric study on different interface properties. Furthermore, it allows us to explore other possible touchdown dynamic patterns, by pushing the interface parameters to some certain limits, which may shed light on possible future recording schemes.

In this chapter, we use the numerical approach developed in Chapter 4 to explore the touchdown patterns of a thermal-flying-height-control (TFC) slider. Depending on the roughness of the head disk interface and thickness of the lubricant layer, we find that a TFC slider can experience different stages during touchdown. Three different touchdown patterns are shown. With a rougher interface profile the slider smoothly transfers from a flying stage to a sliding stage. With a medium roughness interface profile the slider experiences a flying-bouncing-sliding transition. With the smoothest interface the slider goes through a flying-bouncing-surfing-sliding transition. Different stages are characterized by different slider dynamics and slider-disk contact states. At the bouncing stage, the slider experiences strong vibrations at the 2nd air bearing frequency and intermittent hard contacts with the disk, while the sliding stage is characterized by limited vibration amplitude and continuous deep slider-disk contact. At the so-called surfing stage [78, 113], which can exist between the bouncing and sliding stages, the slider experiences small vibrations and intermittent light contacts with the disk. The different touchdown dynamic patterns shown here can result in significant differences in the successful touchdown detection. The general approach proposed here can also be used to investigate the effects of other important head disk interface factors, e.g., air bearing surface feature geometry, heater design and position, suspension design, etc. on the slider's touchdown dynamic behaviors.

Section 6.2 discusses different interface settings and their effects on the interfacial forces varying with spacing reduction. Section 6.3 shows and compares three representative touchdown dynamic patterns obtained with three different interface

settings. Section 6.4 compares the numerical results with experiments in terms of touchdown stages and excited dynamic modes. Section 6.5 uses a harmonic analysis on a full head gimbal assembly model including the air bearing as a supplementary study to explain the extra dynamic modes found in experiments but missed in the dynamic simulations.

6.2 Interface settings and the resultant interfacial forces

In Chapter 4, we developed an interfacial force model based on a multi-asperity approach, which shows that the relationship between interfacial forces and head disk separations are highly dependent on the interface profiles and lubricant thickness. In state-of-the-art hard disk drives, the lubricant thickness t has been reduced to ~1 nm and the root-mean-square roughness σ is now around 0.5 nm. Table 6.1 lists three sets of interface parameters, which as will be shown later lead to very different touchdown dynamic patterns. These parameters are carefully chosen based on recent literature on the slider and disk topography measurements [71-73, 125]. The product of ($\sigma R\eta$) is kept around ~0.04, as suggested by the original Greenwood-Williamson model, to make sure the surface is realistic. The lubricant thickness t is kept at 1.2 nm so that we can directly compare the flying height of the slider without considering the different pushback due to lubricant layers of different thicknesses. The value of σ is varied to realize different interface roughnesses and different ratios of t / σ. Other related interfacial parameters are listed in Table 6.2. The same disk profile as shown in Figure 5.2 is applied on the disk to account for the disturbance from the disk rotation.

Table 6.1 Three sets of interface parameters that produce different touchdown dynamic patterns

σ (nm)	R (μm)	η (μm^{-2})	t (nm)	$\sigma R\eta$	t/σ
0.6	0.5	133.33	1.2	0.04	2
0.501	0.5	159.68	1.2	0.04	2.4
0.35	0.5	200	1.2	0.035	3.4

Table 6.2 Other interfacial parameters for calculating the interfacial forces

Surface adhesion energy $\Delta\gamma$ (N/m)	0.055
Disk Young's modulus (GPa)	280
Slider Young's modulus (GPa)	280
Disk Poisson ratio	0.24
Slider Poisson ratio	0.24
Disk hardness (GPa)	13
Potential difference between the head and disk (v)	0.5

Figure 6.1 shows the normalized contact force $F_c / (EA_n)$ varying with the head disk spacing h. Here the spacing h instead of the normalized separation d / σ is used so that we can easily correlate with the flying height which will be shown later in this chapter. For a rougher interface profile (a larger σ), contact force takes off at a higher h. The contact force for a smoother interface profile (a smaller σ) takes off at a lower h, but its rate of change with the spacing reduction quickly exceeds that of a rougher interface with the

reduction in h. In Figure 6.2, the normalized adhesion force F_s / (EA_n) shows a similar trend where the adhesion force of a rougher interface takes off at a higher spacing h, however with the smallest σ, the maximum magnitude of the slope $d(F_s / (EA_n)) / dh$ is the greatest among all three cases.

Because electrostatic force varies much more slowly, compared with contact and adhesion forces, at extremely low spacing, the pull off force is mainly dependent on the contact and adhesion forces. In Figure 6.3 we neglect the effect of electrostatic force and plot the normalized pull off force ($F_s - F_c$) / (EA_n) against the head disk spacing h. All three curves have a region where the adhesion force dominates the contact force and thus inverts the sign of the slope and drives the pull off force to a negative value. The sign of the curve slope changes back when the spacing is further reduced so that the contact force becomes dominant.

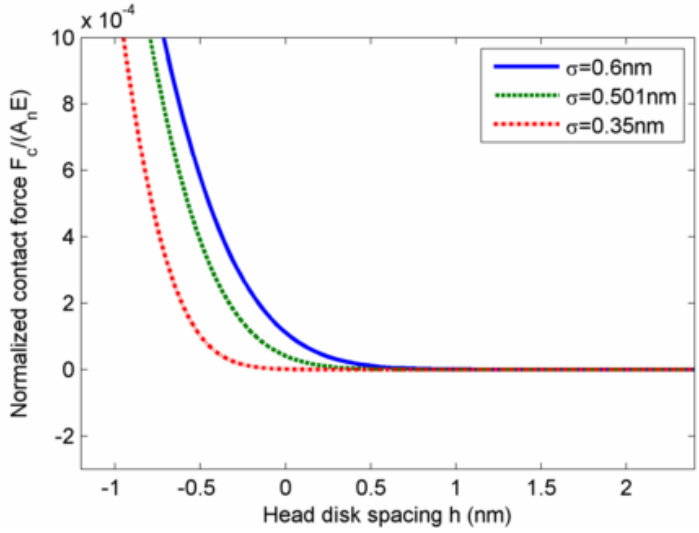

Figure 6.1 Normalized contact force F_c / (EA_n) as a function of the head disk spacing h for the three cases listed in Table 6.1.

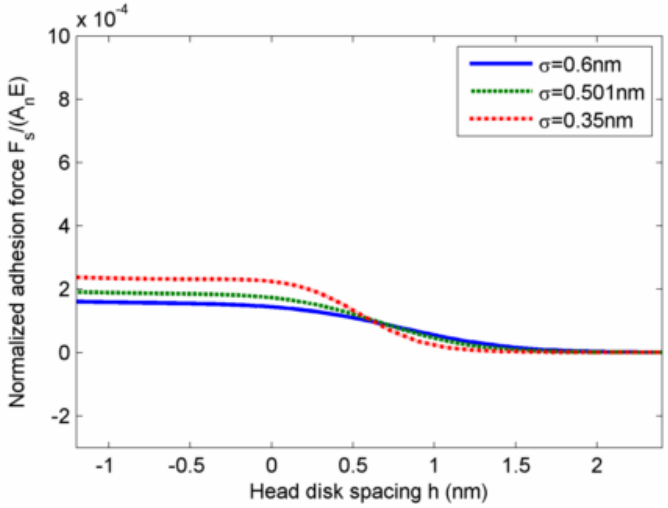

Figure 6.2 Normalized adhesion force F_s / (EA_n) as a function of the head disk spacing h for the three cases listed in Table 6.1.

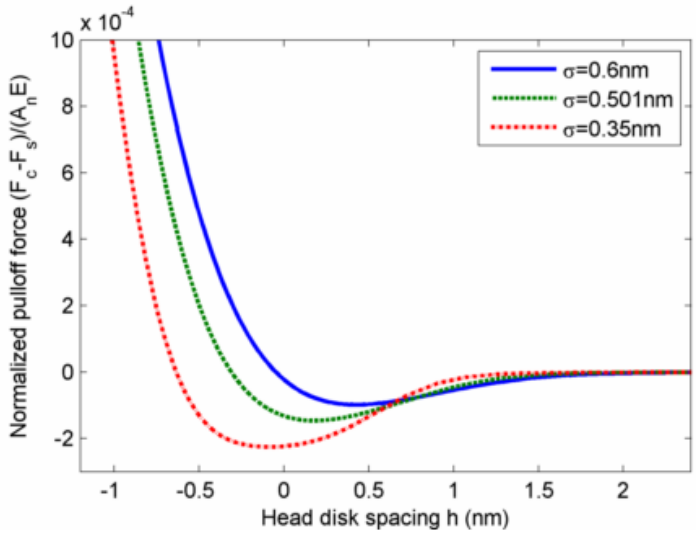

Figure 6.3 Normalized pull-off force $(F_c - F_s) / (EA_n)$ as a function of the head disk spacing h for the three cases listed in Table 6.1.

6.3 Different touchdown dynamic patterns

6.3.1 Touchdown pattern 1: flying – bouncing - sliding

The first touchdown pattern is obtained with an intermediate interface roughness (σ = 0.501 nm). As shown in Figure 6.4, the peak protrusion on the air bearing surface ramps up from 20 nm to 50 nm in a 10 ms time period to bring the slider from flying to touchdown. The corresponding flying height modulation at the transducer shows an instability region where the slider experiences obviously stronger dynamics. The time average of the transducer's FH shows that the slider keeps penetrating deeper into the disk during this process. The time average of the transducer's flying heights is obtained by taking an average on every 2500 points, assuming that the slider dynamics does not have abrupt changes within 0.25 ms.

Figure 6.5 shows the contact force as a function of the peak protrusion where, by the features of the contact force curve, we can roughly divide the touchdown process into three stages: the flying stage where the contact force is essentially zero, the bouncing stage where the contact force oscillates between zero and positive values, and the sliding stage where the contact force is always above zero. Comparing Figure 6.5 with Figure 6.4, we see that the bouncing stage corresponds to the instability region.

Figure 6.6 shows the flying height 3σ and the average contact force as functions of the peak protrusion applied on the slider. The flying height 3σ curve is obtained by calculating the standard deviation of every 2500 flying height data points. At the flying stage, the slider has a very limited modulation amplitude of ~0.5 nm, almost equal to the 3σ value of the disk profile, which means the slider is almost perfectly following the disk profile. When the slider is pushed to touchdown, strong bouncing vibrations occur which bring the 3σ value to as high as ~1.5 nm, roughly 3 times that of the flying stage. Correspondingly, the average contact force jumps from 0 to ~0.4 mN. When the bouncing vibrations are being damped and the slider gets out of the instability region, the

average contact force stays stable for some while. However, once the slider enters into the sliding stage, where its 3σ falls back to ~0.6 nm, the contact force starts increasing rapidly with the protrusion.

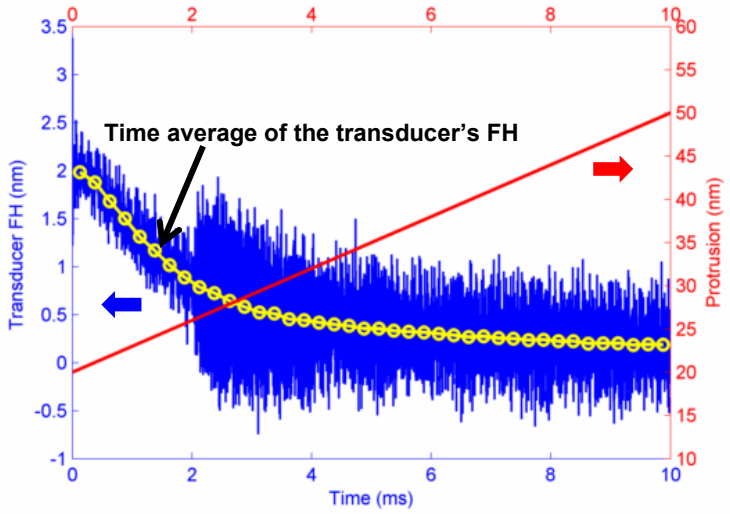

Figure 6.4 Peak protrusion and the transducer's flying height as a function of time. The time average of the transducer flying height is also shown.

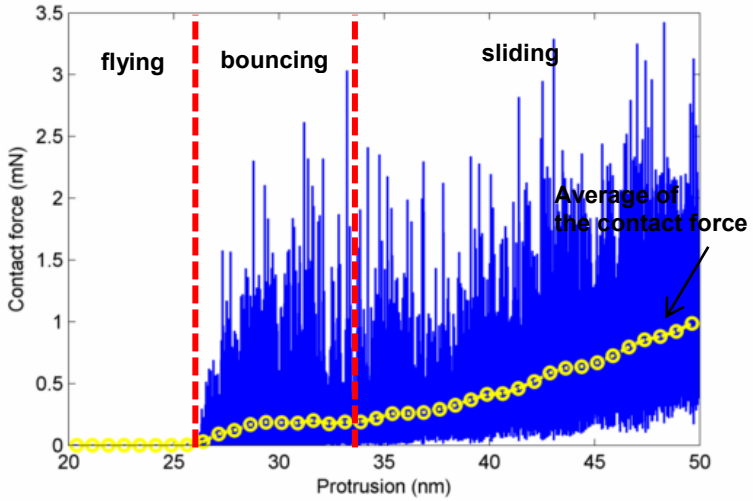

Figure 6.5 Contact force acting on the slider as a function of the peak protrusion. The average value of the contact force is also shown.

In Figure 6.7 we plot the flying height 3σ and the average contact force against the minimum flying height of the slider in order to have some idea about the head disk spacing at the different touchdown stages. Following the idea of the statistical approach presented in Chapter 4, by integrating the Gaussian function which describes how the

asperity heights are distributed, we can know the percentage of asperities in non-contact, lubricant-contact and solid-contact status at the minimum flying height point:

$$P_{non-contact} = \int_{-\infty}^{h_{\min}-y_s} \phi(u)du$$
$$P_{lubricant-contact} = \int_{h_{\min}-y_s}^{h_{\min}-y_s+t} \phi(u)du \quad (6.1)$$
$$P_{solid-contact} = \int_{h_{\min}-y_s+t}^{\infty} \phi(u)du$$

where $P_{non\text{-}contact}$, $P_{lubricant\text{-}contact}$, $P_{solid\text{-}contact}$ are percentages of asperities in non-contact, lubricant-contact and solid-contact status, respectively.

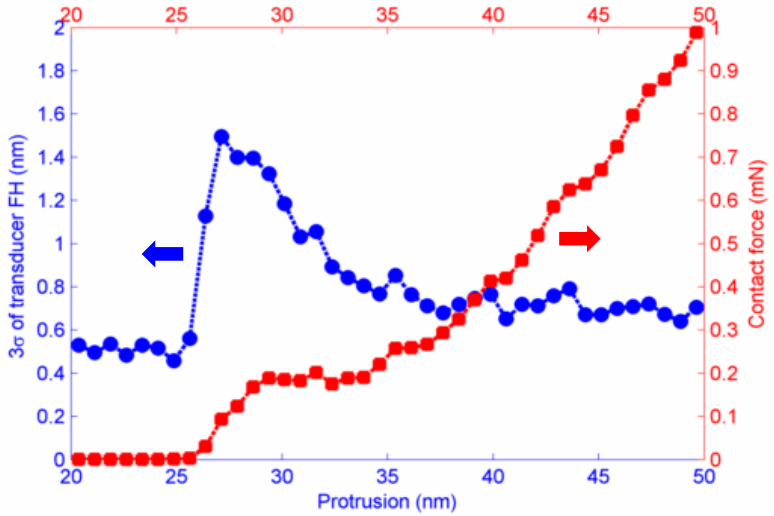

Figure 6.6 3σ of the transducer's FH and average contact force as functions of the peak protrusion on the slider.

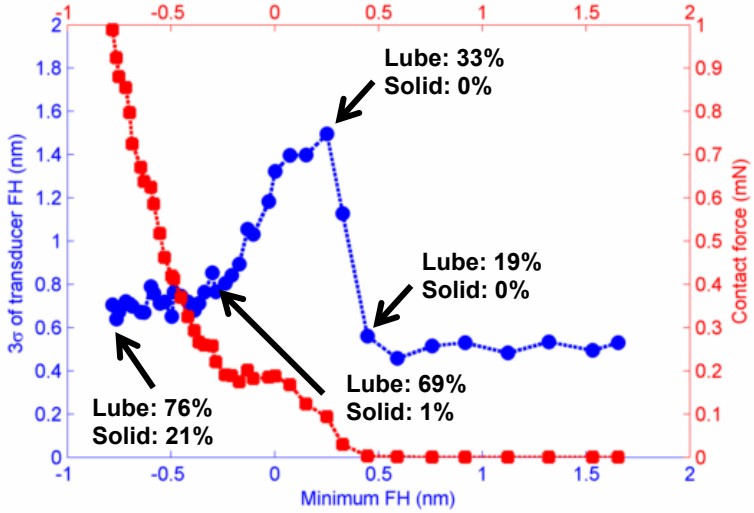

Figure 6.7 3σ of the transducer's FH and average contact force as functions of minimum flying height. The minimum flying height is lowest flying height on the air bearing surface, calculated from the mean plane of surface heights of the lubricant layer.

As can be seen from Figure 6.7, right before the bouncing stage, there is no solid contact and 19% of the asperities at the minimum flying height point are in the lubricant-contact status. As the slider goes through the bouncing stage, the lubricant-contact percentage increases to 69% but the solid-contact percentage remains unchanged. As the slider enters into the sliding stage, the solid-contact percentage rapidly increases from 0 to 21%.

6.3.2 Touchdown pattern 2: flying – sliding

The second touchdown pattern is obtained with the roughest case (σ = 0.6 nm). The same actuation profile is applied on the slider, as in 6.3.1. As shown in Figure 6.8, the slider's dynamics remains quite stable throughout the touchdown process. Comparing with Figure 6.9, which shows the history of the contact force, it is clearly seen that the touchdown process is divided into two stages: the flying stage and the sliding stage. The bouncing stage completely disappears.

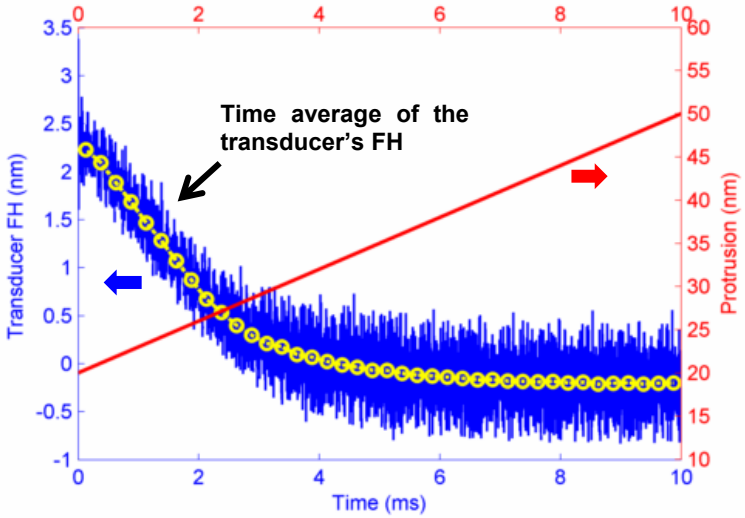

Figure 6.8 The peak protrusion applied on the slider and the transducer's flying height as functions of time. The average flying height at the transducer's location is also shown.

As shown in Figure 6.10, the 3σ of the transducer's flying height only increases from ~0.5 nm to ~ 0.6 nm after the slider touches down on the disk. The contact force increases rapidly with protrusion immediately after touchdown occurs. Figure 6.11 shows the 3σ of the transducer's flying height and the average contact force varying with the minimum flying height, where the contact status at the minimum flying height point is marked for each stage. It is interesting to note that after touchdown, the percentage of solid contact asperities first slowly increases to 14% at the initial sliding state and then rapidly increases to 52% with further reduction in flying height.

6.3.3 Touchdown pattern 3: flying – bouncing – surfing – sliding

The third touchdown pattern is obtained with the smoothest interface profile where σ equals 0.35 nm. As shown in Figure 6.12, the slider experiences an instability region, which is similar to the first touchdown pattern. However, the contact force history, which is shown in Figure 6.13 is different from the first case. Between the bouncing stage and

the sliding stage, a stage with stable dynamics as well as minimum contact force, especially at the very beginning, exists. We term this stage a "surfing" stage here [76, 78] because the flying height of the transducer is still going down as can be seen from Figure 6.12 but there is little solid contact. So the only possibility is that the slider is in contact with the lubricant layer but barely touches the solid asperities beneath the lubricant.

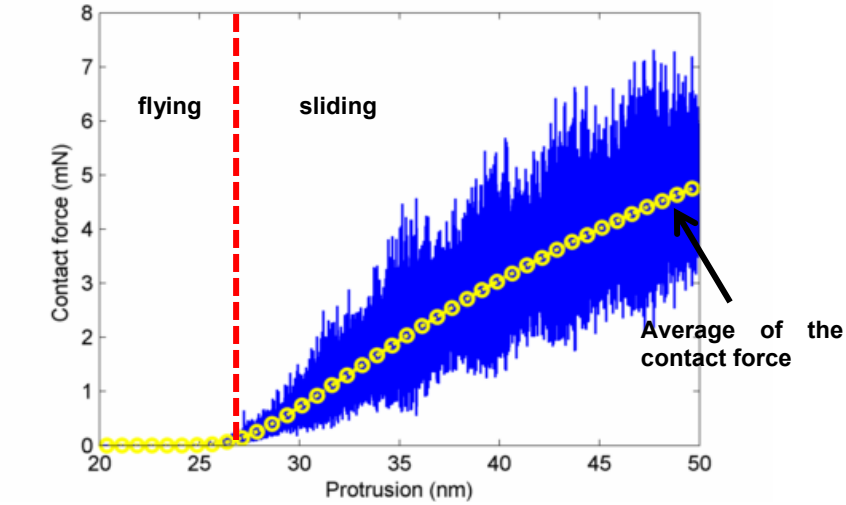

Figure 6.9 Contact force as a function of the peak protrusion during the touchdown process. The average of the contact force is also shown.

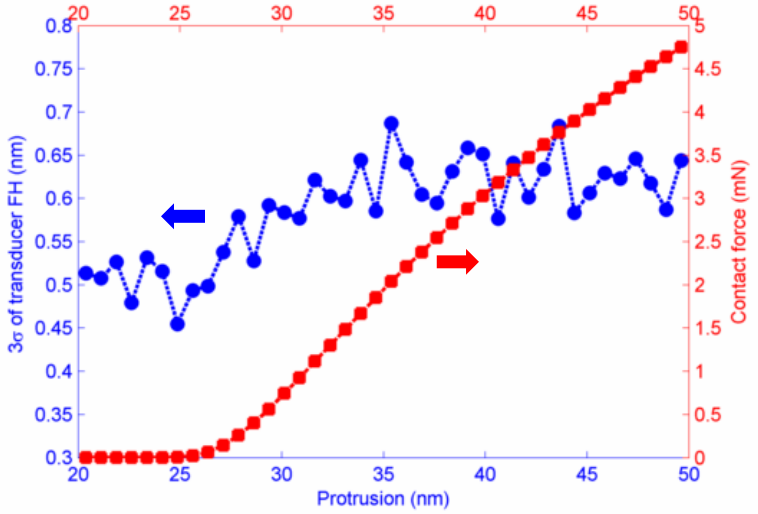

Figure 6.10 3σ of the transducer's FH and average contact force as functions of the peak protrusion on the slider.

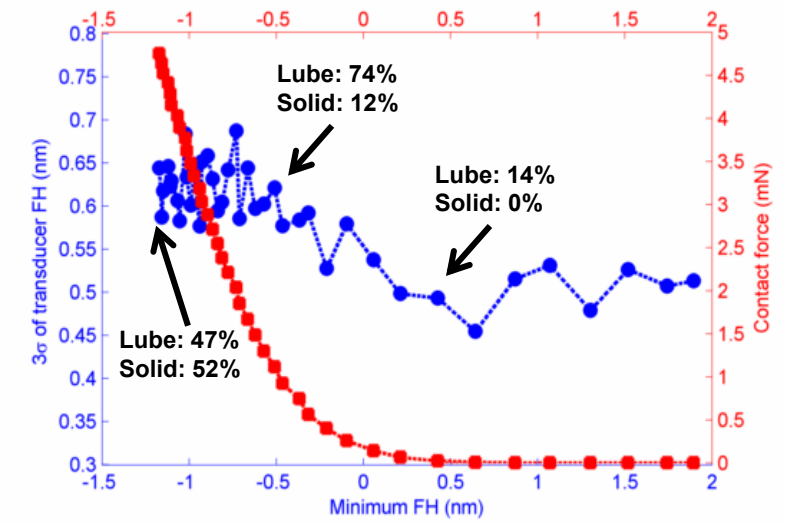

Figure 6.11 3σ of the transducer's FH and average contact force as functions of minimum flying height. The minimum flying height is lowest flying height on the air bearing surface, calculated from the mean plane of surface heights of the lubricant layer.

As shown in Figure 6.14, the average contact force steps up when the slider starts bouncing, however, as the slider comes out of the bouncing stage, the contact force falls back to zero and stays there before the slider enters the sliding stage, which causes the contact force to increase rapidly with increasing protrusion.

Referring to Figure 6.15, there is no sign of solid contact as the slider touches down, starts bouncing and comes out of the bouncing stage, at the minimum flying height point. It is worth noting that between the minimum flying height 0 and ~ -0.5 nm, although the slider is getting closer to the disk, the solid contact asperities only increase by one percent. However, once the slider goes below ~ -0.5 nm, the solid contact asperities quickly increase to 17%, and accordingly, the contact force increases quickly with the decreasing flying height.

Figure 6.16 shows a comparison of 3σ of the transducer's FH for the three cases shown above. With a rougher interface profile, there is more stable dynamics of the slider, and for the roughest case, there is no instability region. Because the variation in the dynamics of the slider is commonly used in experiments to detect the occurrence of touchdown, this result also indicates that it is more difficult to detect touchdown in rougher interfaces.

From the spacing point of view, all three interfaces can maintain the slider at a stable read/write spacing for a flying height greater than ~ 0.5 nm. But the slider in the two smoother cases loses the stable read/write spacing once the minimum flying height goes below ~ 0.5 nm. However, the slider comes back to a stable state when the minimum flying height is further reduced to less than ~ -0.5 nm. But as can be seen from Figure 6.17 the contact status between the slider and disk are very different for the three cases at this low flying height. The slider experiences a much stronger contact force in the roughest interface but essentially zero contact force in the smoothest interface. This

suggests that there may be a potential for ultra-low operating flying height with the smoothest interface, at which the slider achieves a stable read/write spacing while contacting only with the lubricant layer. It should be noted that although the numerical model here predicts a stable state of the slider at the surfing stage, the feasibility of recording at the surfing stage is still questionable because the interaction between the slider and the disk lubricant can cause other issues, like disturbances to the lubricant surface profiles, contamination on the air bearing surface, etc. These problems can prevent the slider from maintaining a stable read/write spacing.

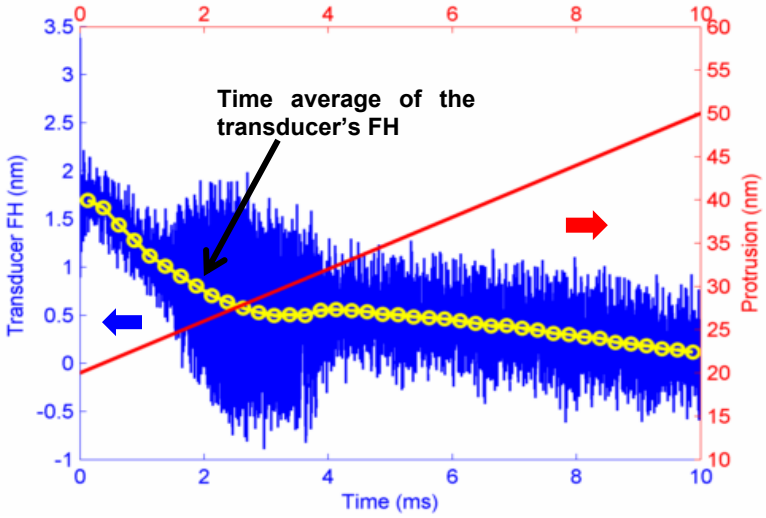

Figure 6.12 The peak protrusion applied on the slider and the transducer's flying height as functions of time. The average flying height at the transducer's location is also shown.

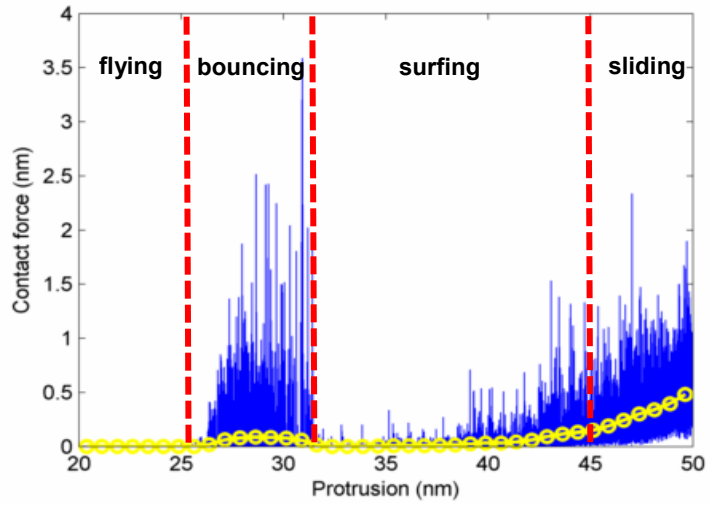

Figure 6.13 Contact force as a function of the peak protrusion during the touchdown process. The average of the contact force is also shown.

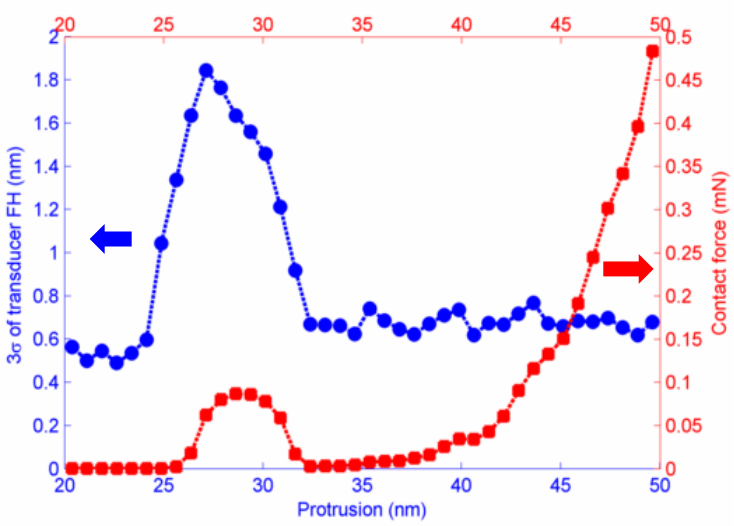

Figure 6.14 3σ of the transducer's FH and average contact force as functions of the peak protrusion on the slider.

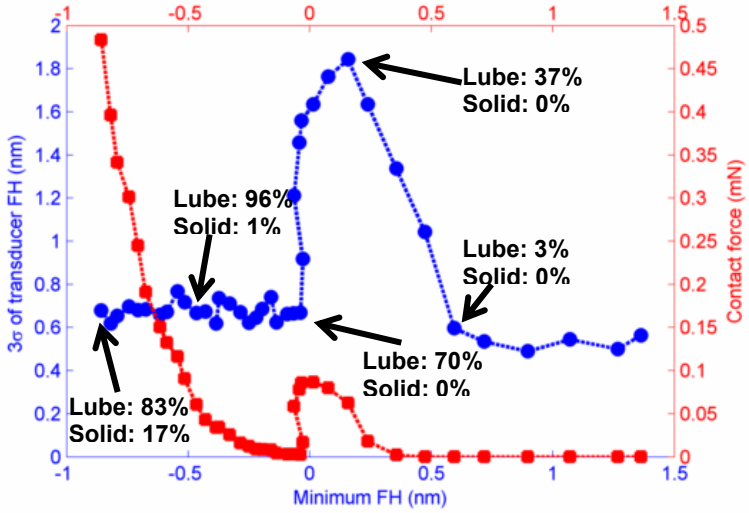

Figure 6.15 3σ of the transducer's FH and average contact force as functions of minimum flying height. The minimum flying height is lowest flying height on the air bearing surface, calculated from the mean plane of surface heights of the lubricant layer.

Referring back to Chapter 5, where we show that the adhesion force is a potential source of inducing bouncing vibrations at touchdown, here we can interpret the touchdown patterns obtained with different interface roughnesses from the behaviors of adhesion forces for the three investigated cases. Figure 6.18 shows the asperity height distribution function $\phi(u)$ for two interface profiles: the one on the first row represents a rough interface where $\phi(u)$ spreads in a wider range of asperity heights, the one on the second row represents a smooth interface where $\phi(u)$ is concentrated in a narrow range of asperity heights. For a given head disk separation d, asperities higher than d are in solid-contact status, asperities higher than d-t but lower than d are in lubricant-contact status, and the rest of the asperities are in non-contact status.

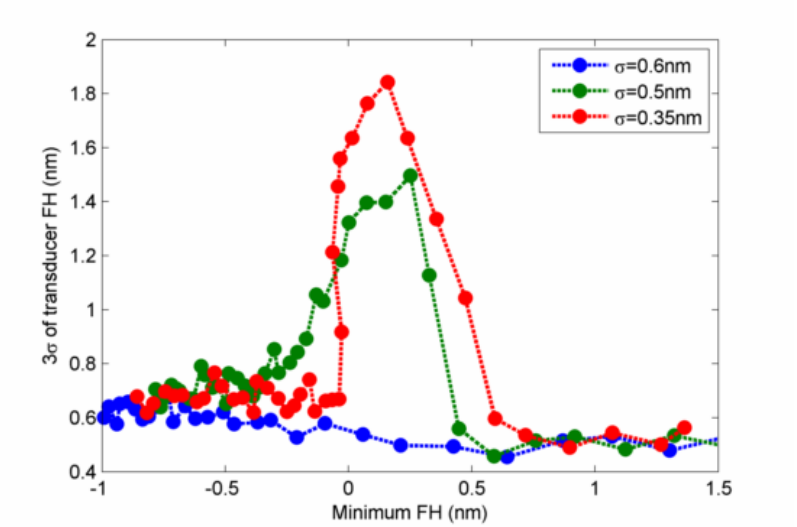

Figure 6.16 3σ of the transducer's FH as a function of the minimum flying height. The minimum flying height is lowest flying height on the air bearing surface, calculated from the mean plane of surface heights of the lubricant layer.

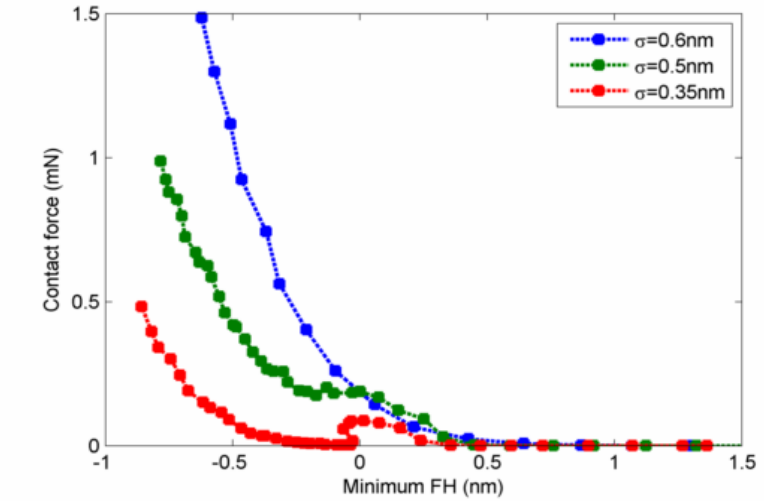

Figure 6.17 Average contact force as a function of the minimum flying height.

Referring to the first column in Figure 6.18, at a higher separation d_1, which corresponds to a higher flying height, due to the existence of high asperities in the rough interface, some adhesion is generated at the high asperities. But this adhesive effect is weak because of the limited number of high asperities. On the other hand, almost all asperities in the smooth interface are too far away to cause any significant adhesive effect on the slider.

As the separation reduces from d_1 to d_2 (the second column in Figure 6.18), for the rough case, the number of lubricant-contact asperities quickly increases and occupy a large area beneath $\phi(u)$ and causes a strong adhesion force. But solid contact bonds are

also created at some high asperities, resulting in supportive force that adds to the air bearing lift and offsets the adhesive effect. For the smooth interface, the adhesion force quickly increases to a maximum because most asperities are at approximately the same height and are close enough to generate strong adhesive effects. As a result, a slider in a smooth interface is likely to experience large bouncing vibrations caused by this rapidly increasing adhesion force.

As the separation further reduces to d_3 (the third column in Figure 6.18), it is seen that the percentage of solid-contact asperities quickly increases in the rough case that further suppresses the effects by adhesion. However, because of the high ratio of t/σ, the percentage of asperities causing adhesion barely changes from the separation d_2 to d_3, for the smooth case. On the other hand, the percentage of solid-contacting asperities is still too small to cause any significant contact force. Thus the slider is likely to get back to stable dynamics and this may result in a surfing stage as we see in Section 6.3.3.

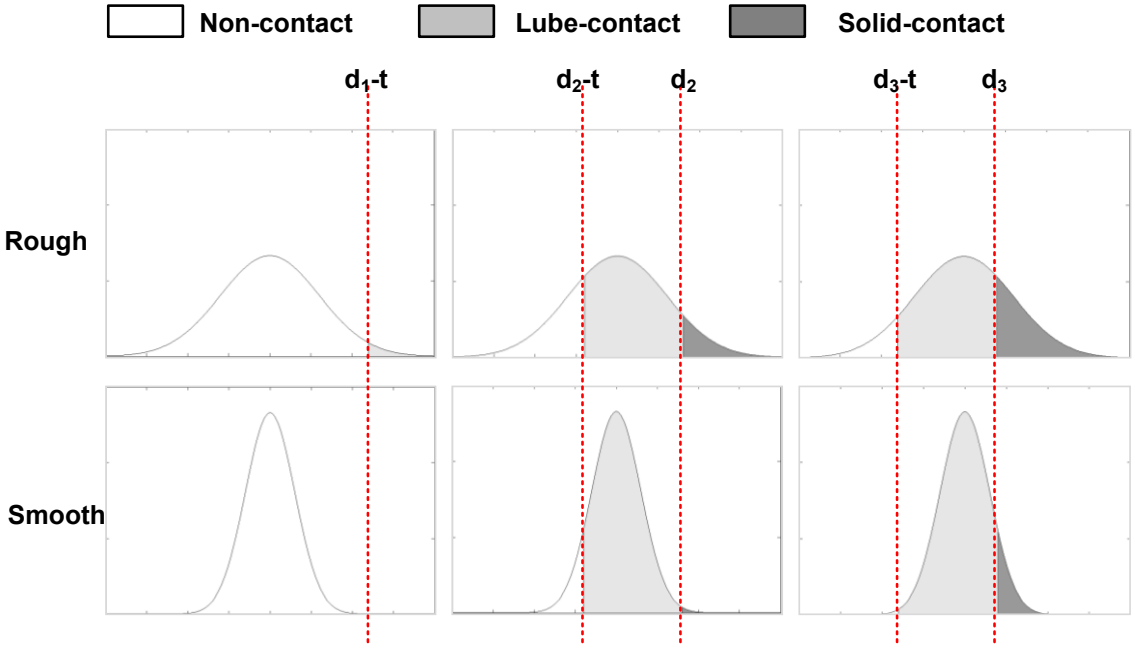

Figure 6.18 Illustration of contact status for rough and smooth interfaces. The Gaussian function $\phi(u)$ in the first row corresponds to a rough surface profile. The Gaussian function $\phi(u)$ in the second row corresponds to a smooth surface profile. The dark, grey and white areas correspond to the percentage of solid-contact, lube-contact and non-contact asperities, respectively.

6.4 Correlations with experiments

This work is completed jointly with Yung-Kan Chen, who has completed the experimental part here.

The experiments are performed on a stage capable of making in-situ measurements using an acoustic emission (AE) sensor and a laser Doppler vibrometer (LDV). The AE sensor detects the elastic-stress waves in the slider and suspension caused by slider-disk contacts and the LDV measures the vertical velocity of the slider at the center of its

trailing edge (TEC). The head parts subject to the experimental study have the same air bearing and suspension design as the numerical study shown in Section 6.3.

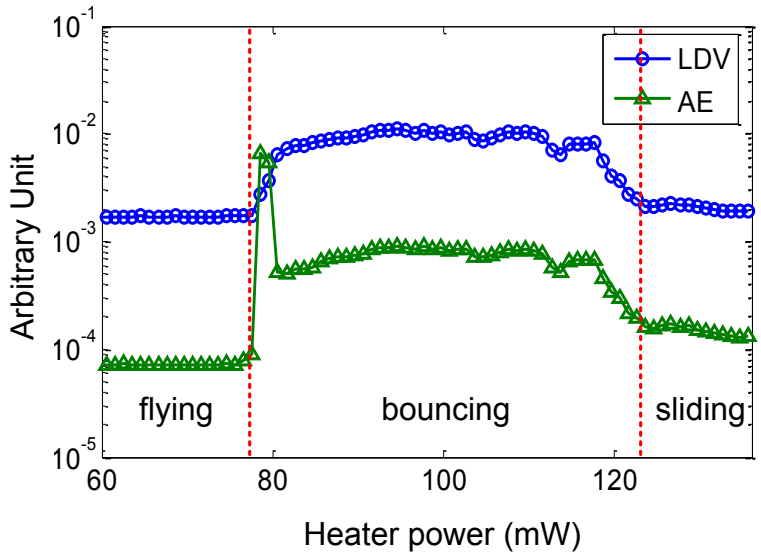

Figure 6.19 The slider's velocity 3σ at the trailing edge center measured by LDV and AE as a function of the applied heater power.

A total of three touchdown stages can be identified from Figure 6.19. The first stage features a very limited 3σ value, showing the slider maintains a stable flying height at the trailing edge center, as well as a relatively low AE signal, showing little interactions between the slider and disk. Thus the first stage is considered to be a flying stage. The second stage starts at a heater power of ~78 mW, where both LDV and AE signals jump up significantly. The big LDV signal suggests that the slider is vibrating violently at the trailing edge center, and this leads to strong interactions between the slider and disk which are picked up by the AE sensor. Therefore this stage is considered to be the bouncing stage. It is noted that the AE signal has a spike at the very beginning of the bouncing stage but such a spike is not seen in the LDV curve. We do not currently have a good explanation for this spike. As the slider is further pushed with even higher heating powers, the slider enters into a third stage where it experiences much weaker dynamics and head-disk interactions, compared with the bouncing stage. However, the LDV and AE signals are still higher compared with the flying stage. These phenomena are consistent with the characteristics of the surfing stage shown in the numerical studies conducted in Section 6.3.3, where the slider is back to stable dynamics and only in contact with the lubricant layer when it is being over pushed out of the bouncing stage.

Figure 6.20 shows the spectrum of the slider's dynamics at the trailing edge center using the simulation data presented in Section 6.3.3 where the slider is experiencing a flying – bouncing – surfing – sliding transition during touchdown. Figure 6.21 shows the spectra obtained from the experiments. In both simulations and experiments, we find a strong excited mode at around ~ 400 kHz at the bouncing stage, though the simulated frequency is slightly higher and tends to have a more obvious slope with increasing protrusion. In addition, the frequency content in the measured data is richer than the simulated data. There is a slightly excited mode at ~133 kHz at the very beginning of the

bouncing stage. A mode at ~234 kHz is also slightly excited during the bouncing stage. Considering the approach we used in our numerical study, there are two possible reasons for the absence of these modes from the simulation data. One is the reduction process conducted on the finite element HGA model where we reduced a much larger system into a 250-DOF mass-spring system. Another possible source is the interfacial force models. The excited modes are highly dependent on the type and magnitude of excitation forces. Although the interfacial force model captures the general trend correctly, for instance, it correctly captures the strongest excited mode at touchdown, it might miss some details of force variations which leads to the absence of some less obvious frequency components.

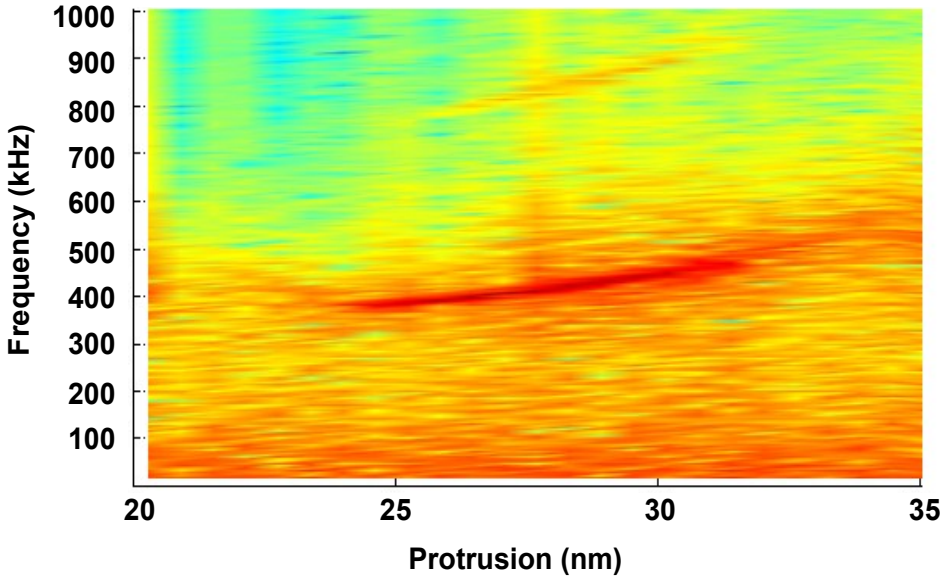

Figure 6.20 Spectrum of the slider's dynamics at the trailing edge center obtained by conducting Fourier analysis on the data presented in Section 6.3.3.

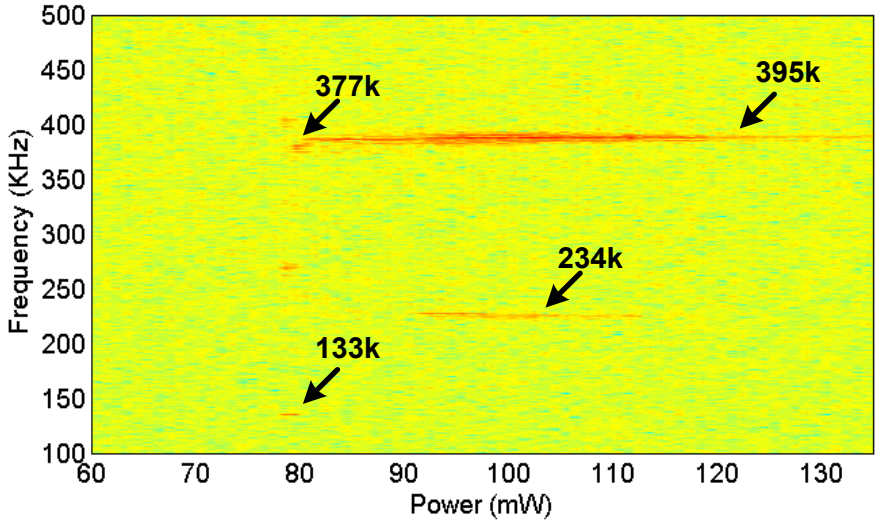

Figure 6.21 Spectrum of the slider's dynamics at the trailing edge center obtained by conducting Fourier analysis on the LDV measured flying height at the trailing edge center.

6.5 Harmonic analysis on a full HGA model including the air bearing

Based on the comparison made between the measured and simulated data in Section 6.4, here we use a different numerical approach and try to recover the missing frequency components in the simulated data.

In previous chapters, we simplify the HGA model and then combine the reduced model with a full air bearing to conduct the dynamic simulations. In this section, instead of reducing the HGA model, we simplify the air bearing model as a 3-by-3 stiffness matrix and combine it with a full finite element HGA model. This model is then subject to harmonic analysis in order to obtain its frequency responses under different excitation conditions.

Figure 6.22 shows a schematic of the HGA model subject to harmonic analysis. We first follow the procedures in [96] to obtain the 3-by-3 stiffness matrix representing the air bearing. The stiffness matrix is obtained by applying the 18 nm protrusion geometry on the air bearing surface, at which protrusion the slider is still flying. The reason is that the stiffness matrix is a linear approximation of the complicated air bearing system and such a linear approximation is very suspect at touchdown conditions because of the existence of non-linear forces at touchdown. Then we incorporate the air bearing into the original HGA model by modeling it as an elastic element defined by the stiffness matrix. One end of the element is connected to the slider's mass center and the other end is connected to the disk. For simplicity, the slider is represented by a mass element defined by a 3-by-3 mass matrix and connected to the flexure using rigid beams, as shown in Figure 6.23. The air bearing is modeled by an elastic element, which does not have a definite shape but can be defined by two nodes and the stiffness matrix. One node of this elastic element is the slider's mass node and the other is the disk node, which is fixed in all six degrees of freedoms.

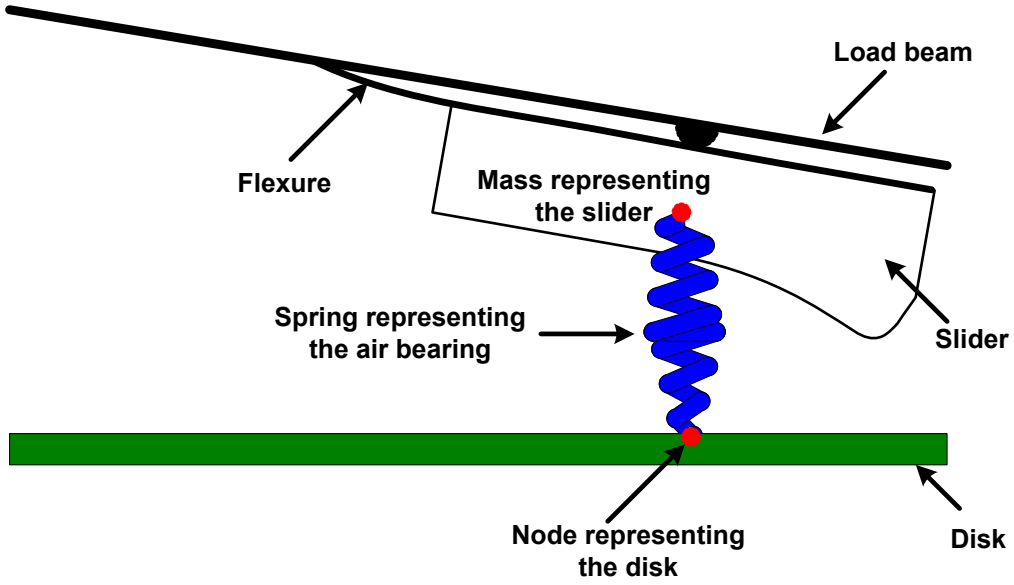

Figure 6.22 Schematic of the HGA model with the air bearing included. The air bearing is represented by a spring element defined by a 3-by-3 stiffness matrix with one end connected to the slider's mass center and the other end connected to the disk.

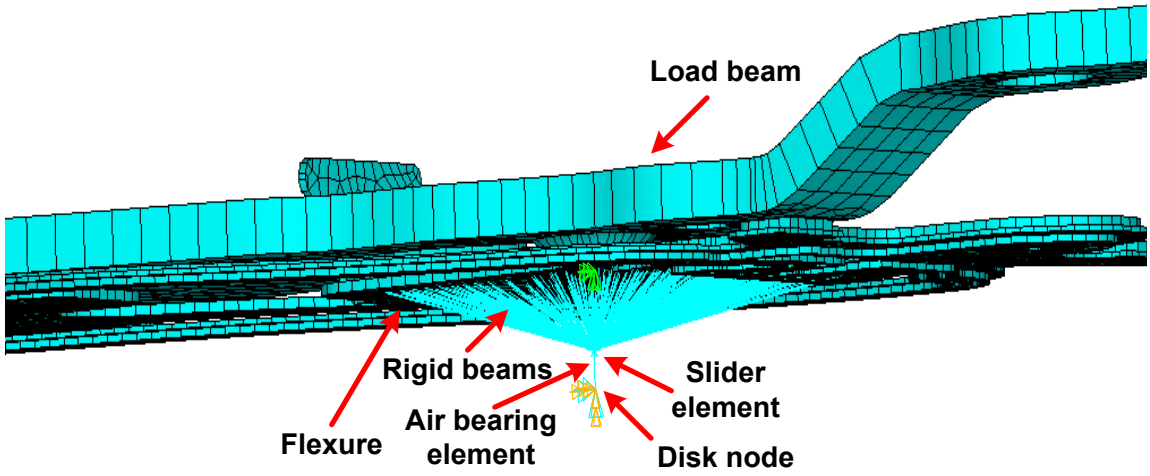

Figure 6.23 The finite element model in ANSYS of the HGA with air bearing included. The slider is connected to the flexure by rigid beams. The slider is represented by a mass element defined by a 3-by-3 mass matrix. The air bearing is represented by a single elastic element defined by the 3-by-3 stiffness matrix with one end connected to the slider mass node and the other end connected to the disk node, which is fixed in all six degree of freedoms.

Two types of excitation are applied using this model. In one case, we apply a 10 mN force along the track (in the *x* direction) at the slider's trailing edge center. 10 mN is chosen because most interfacial forces are on the order of mN, as shown in previous simulations. Such an excitation force can be, for example, the friction force, which is in-plane and concentrated around the slider's trailing edge center. In the other case, we apply a 10 mN along the flying height direction (in the *z* direction) at the slider's trailing edge center, which could represent an out-of-plane force such as the contact and adhesion forces.

We sweep the frequency of the excitation force from 1 kHz to 400 kHz with a step size of 1 kHz and the results are shown in Figure 6.24. It is interesting to notice that different modes become dominant at different excitation conditions and this helps to explain why the slider has different dominant modes at different touchdown stages, as seen from Figure 6.21. With an in-plane excitation, the dominant modes are concentrated at the frequency range from 120 kHz to 150 kHz, and as shown in Figure 6.25, these modes have nodal lines located near the trailing edge of the slider so they are related to the slider's first air bearing pitch mode. This is consistent with our numerical analysis in Section 5.5 where we show an in-plane force such as the friction force is associated with the excitation of the 1st air bearing mode. Comparing with the experimental results shown in Figure 6.21, we conclude that the peaks at 122 kHz and 152 kHz are associated with the 133 kHz mode observed in experiments.

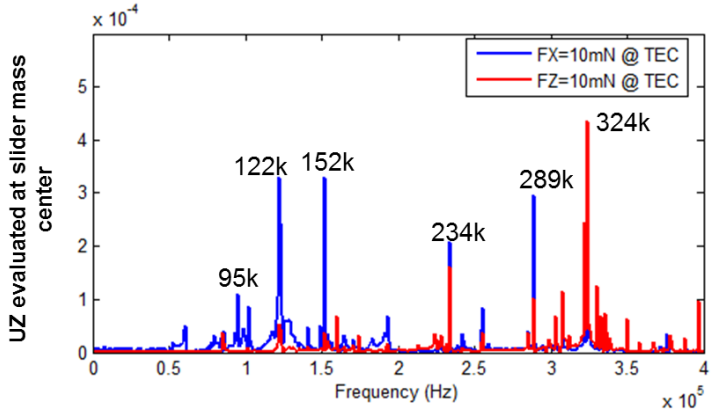

Figure 6.24 The slider's frequency response observed at the mass center under two types of excitation sweeping from 1 kHz to 400 kHz. The first case is obtained by applying a 10 mN excitation force along the *x* direction at the slider's trailing edge center. The second case is obtained by applying a 10 mN excitation force along the *z* direction at the slider's trailing edge center.

With an out-of-plane excitation, the dominant mode changes to the 324 kHz mode, which has a nodal line located at the leading edge of the slider and is considered to be related to the second air bearing pitch mode, as can be seen from Figure 6.26. This is also consistent with our previous analysis which shows an out-of-plane force such as the adhesion force is likely to excite the slider's second air bearing pitch mode. Comparing with Figure 6.20 and Figure 6.21, we conclude that the 324 kHz is related to the strong mode at ~ 400 kHz. The value of the frequency is different from the previously measured and simulated data, and the reason is probably due to the evaluation of the air bearing stiffness at a flying state. As the slider is pushed to the touchdown state, the pressure peak at its trailing edge should grow significantly and increase this frequency by tens of kilo Hertz [126, 127]. It is also worth noting that the 234 kHz mode observed in Figure 6.21 and missed from Figure 6.20 is recovered in the harmonic analysis, which proves the possibility of exciting this air bearing – suspension coupled mode with appropriate excitation force combinations.

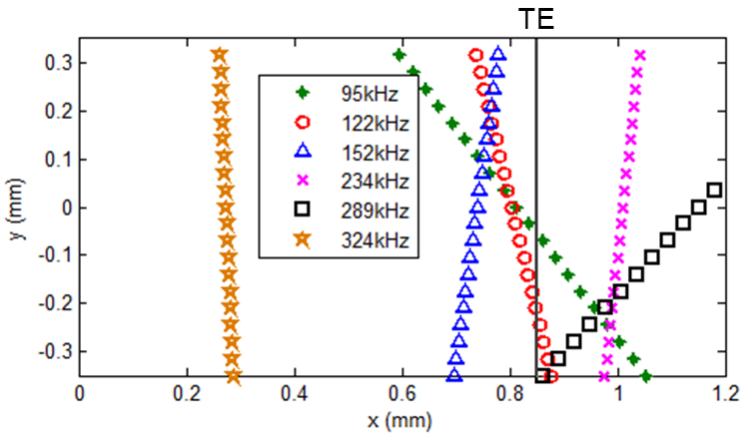

Figure 6.25 Nodal lines corresponding to frequency peaks observed in the in-plane excitation case in Figure 6.24. The line TE stands for the location of the trailing edge. 324 kHz mode is the only mode that has a nodal line located at the leading edge. All other modes have nodal lines near the trailing edge.

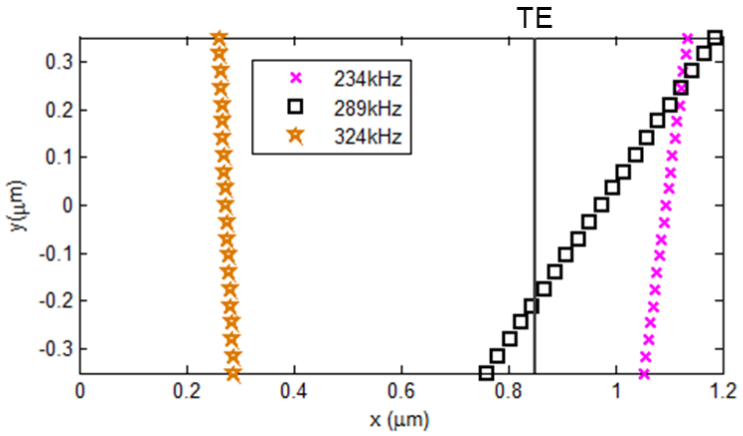

Figure 6.26 Nodal lines corresponding to frequency peaks observed in the out-of-plane excitation case in Figure 6.24. The straight line TE stands for the location of the trailing edge. 324 kHz mode has a nodal line located at the leading edge. All other modes have nodal lines near the trailing edge.

6.6 Summary and conclusion

In this chapter we explored possible touchdown dynamic patterns of a TFC slider with different interface conditions. Three different touchdown patterns are shown where the slider experiences different touchdown stages. With a rougher interface profile the slider experiences a flying-sliding transition where it maintains stable dynamics throughout the touchdown process. With a smoother interface profile a bouncing stage emerges between the flying and sliding stages, where the slider gets excited at the second air bearing pitch mode. With a smooth profile and an appropriate lubricant thickness, a bouncing state can exist between the bouncing and sliding stages, where the slider has stable dynamics as well as little solid contact.

The numerical results were correlated with experiments, in which we also discovered the flying, bouncing and surfing stages. The frequency of the excited second air bearing pitch mode at the bouncing stage obtained from experiments agrees well with the numerical studies. Further, the experiments show richer frequency components in the slider's spectrum. To recover the missed frequency components in the numerical study, we conducted a harmonic analysis on a full HGA model with the air bearing included and showed that different air-bearing-suspension coupled modes can get excited under different excitations. Some modes missed in the simulations were recovered in this harmonic analysis. In addition, this harmonic analysis further verifies the relationships between different interfacial forces and the slider's touchdown dynamics. An in-plane force at the trailing edge, such as the friction force, is proved to contribute to the excitation of the first air bearing pitch mode. An out-of-plane force, such as the adhesion force, is shown to contribute to the excitation of the second air bearing pitch mode.

Chapter 7

Summary and Conclusions

Thermal flying-height control (TFC) technology is now widely used in state-of-the-art hard disk drives as an effective method to reduce the head-disk spacing and improve the drive performance and reliability. Accurate predictions of a TFC head's static and dynamic performance are now a key factor in building a reliable head disk interface and maintain a stable nanometer read/write spacing. However, the complicated structures of the TFC slider and the head disk interface prohibit the usage of analytical methods to solve the full problem. Alternatively numerical schemes provide an efficient and accurate approach to investigate a TFC slider's performance. The research presented here provides efficient numerical approaches to study a TFC slider's steady-state and dynamic performance. The numerical models are applied to investigate the dependence of a TFC slider's performance on various environmental and internal factors, which are the key factors in designing the mechanical part of a magnetic head. The results presented here can be directly correlated with experimental data. In addition, by the convenience of simulation studies we are able to disclose mechanisms that cause these phenomena and give general guidelines for hard disk drive engineers to improve product performance and reliability.

A numerical TFC solver dedicated to solving the steady-state flying attitude of a TFC slider is developed and implemented in Chapter 2. This solver employs the CML air bearing static solver to solve the generalized Reynolds equation to obtain the pressure and spacing fields in the head disk interface together with the commercial ANSYS coupled-field solver to obtain the stress and strain fields due to internal heating. The air bearing cooling effect is incorporated by prescribing the thermal boundary conditions in the coupled-field analysis with the spacing and pressure solutions from the air bearing static solver. An iterative procedure is adopted to treat the coupling between the air bearing solution and the heater-induced protrusion solution. This solver avoids manual switches between different solvers, repeated GUI operations and mapping solutions on different meshes, thus it significantly facilitates designs of the slider air bearing geometry as well as wafer structure. Drive-level magnetic tests on several combinations of air bearing and heater designs show that this solver gives accurate predictions of a TFC slider's steady-state flying height.

Based on the TFC solver, we studied the effects of ambient conditions on a TFC slider's static performance in Chapter 3. It is found that TFC sliders show higher thermal actuation efficiency at a raised altitude, due to weakened cooling as well as less pushback at the transducer area. In addition, a TFC slider is capable of maintaining a more consistent read/write spacing compared with an ordinary slider due to the fact that thermal actuation has the capability of compensating flying height loss caused by water condensation. We also propose a general approach to study a TFC slider's performance in an air-helium mixture, by using which we are able to show the slider's flying height is a highly nonlinear function of the fraction of helium in the gas mixture for a given heater power due to the combined effects of the gas mean free path, viscosity and heat

conductivity. These results are of practical importance for heater and ABS designers to reduce the sliders' sensitivities to ambient conditions and improve product reliability.

The TFC slider's numerical model is extended to the slider's dynamics at touchdown and over-pushed conditions in Chapter 4 by modeling various interfacial forces which contribute significantly to the slider's dynamics at extremely small clearances and extending the solution of the generalized Reynolds equation to the touchdown conditions using a multi-asperity approach. The touchdown dynamics simulator developed therefrom makes it possible to correlate numerical results with a touchdown experimental study, which is a key study to guarantee today's magnetic heads' performance at nanometer clearance. In addition, it provides the flexibility and convenience of parametric studies on various head disk interface factors.

Chapters 5 and 6 used the touchdown simulator to examine the contributions of different head disk interface factors to the slider's dynamics at touchdown and explored possible touchdown dynamic patterns at different interfacial conditions. It was shown that adhesion force can cause large bouncing vibrations and excite the slider's second air bearing pitch mode. By making the interface rougher, it is possible to suppress or even eliminate the bouncing stage existing between flying and sliding stages. By making the interface smoother, it is possible to achieve a surfing stage between bouncing and sliding stages where the slider maintains stable dynamics and barely contacts solid asperities on the disk.

The numerical results from the touchdown simulation program were correlated with experiments in terms of touchdown stages and excited modes. With the usage of the same air bearing and suspension design, flying, bouncing and sliding stages can be identified in experiments and the frequency of the excited second air bearing mode, which is the strongest mode at the bouncing stage, agrees well with the numerical predictions. Though experiments show more frequency components in the slider's spectrum, some frequency components missed from the numerical study can be recovered from a harmonic analysis on a full HGA model with the air bearing included. This analysis also showed that different air-bearing-suspension coupled modes can get excited under different excitations, which provides an explanation of the complicated spectrum obtained in touchdown experiments. Furthermore, both the touchdown dynamic simulation and harmonic analysis reveal the relationships of the in-plane force with the excitation of the first air bearing pitch mode, and the out-of-plane force with excitation of the second air bearing pitch mode. These results provide general guidelines for hard disk drive engineers to design preferable interfaces and achieve desirable slider touchdown dynamics.

Appendix A CML TFC Code User's manual

A.1 Introduction

The CML TFC code includes a set of macro files written in APDL (ANSYS Parametric Design Language), which can be directly executed in the commercial finite element software, ANSYS. These macros use an iterative approach to solve the flying-attitude and thermal deformation of a slider with micro-heaters built within (Thermal Flying-height Control or TFC slider). Figure A.1 shows the flowchart of this solution procedure. This process starts from solving the generalized Reynolds equation to obtain the pressure profile in the air bearing and the spacing in the head-disk interface (HDI). The heat transfer coefficients on the air bearing surface (ABS) are calculated and input to the finite element model of the slider. A coupled-field analysis is then conducted to calculate the deformation of the slider. Considering the effects of the ABS deformation on the flying-attitude, the original ABS shape is updated according to this deformation and used for a new round of spacing and pressure calculations. This procedure continues until the flying-attitudes obtained from two consecutive iterations have a difference less than some specified value. In this procedure, the CML quick4 solver is adopted to solve the generalized Reynolds equation using the finite volume method. The commercial finite element software, ANSYS, is used to execute the electro-thermal-structural analysis. The CML TFC code runs on a windows-platform computer with certain ANSYS products (modules for electric, thermal and structural analysis) installed.

A.2 Related files and structure

A.2.1 File structure

Figure A.2 shows a complete list of files and the relationships between them in the CML TFC code.

The left block contains input files that define the problem to be solved. The files on the first row define the geometry of the air bearing surface, the suspension load, initial flying attitudes, etc. The **.db* on the second row is an ANSYS database file defining the geometry of the slider. *TFCrun.dat* on the third row defines parameters associated with the thermal flying height control.

The middle block contains all of the program files responsible for executing the TFC calculations.

The right block contains 3 groups of output files. The first row includes standard output files generated by the quick4 solver. TFCresult.dat on the second row records the converging process of this iterative procedure. *CMLTFC.db* on the third row is the solved FE model with the geometry, loads and solutions all saved. *CMLTFC.** (*CMLTFC.log*, *CMLTFC.err*, etc.) on the fourth row include the standard files created by ANSYS for each job executed.

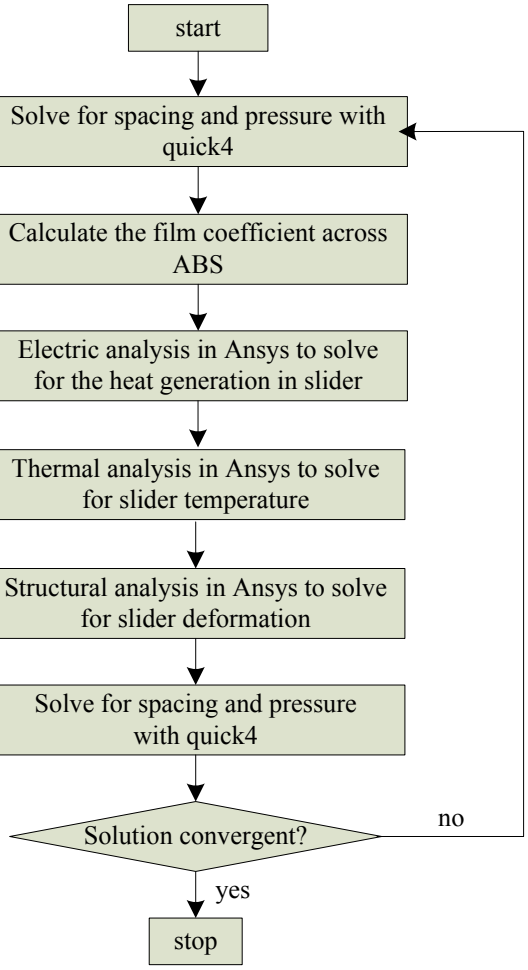

Figure A.1 Flowchart of the TFC solution procedure

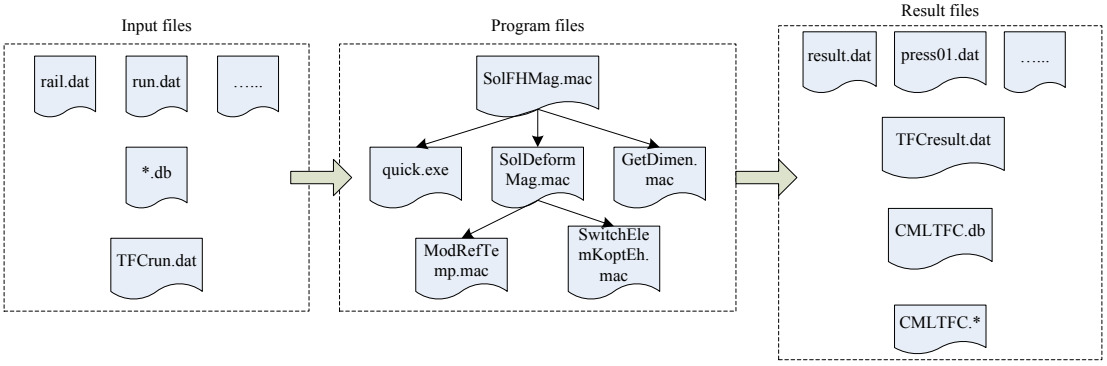

Figure A.2 File structure of the TFC code

A.2.2 Input files

1. TFCrun.dat

```
db file name
************************************
MyModel

thermal model
************************************
ModelType
2

ansys model
************************************
unit    orient
2       1
pad1    pad2
16      15
refTemp(C)
25

heater
************************************
power(mW)  res(ohms)
5           5

mapping
************************************
xmin       xmax
0.75       1
ymin       ymax
0.33       0.67
nx         ny
201        201
```

```
constraints
************************************
backfixed
1


loads
************************************
pres
0


cooling
************************************
back     side          (W/(m.m.k))
100         100



convergence
************************************
criterion   limit(nm)
1           0.01
Max. num. of Iteration
10


air parameters
************************************
Kair(W/(m.K))     gamma        Pr        sigma_T
```

Figure A.3 A Sample TFCrun.dat

A sample file of TFCrun.dat is shown in Figure A.3. This file defines the TFC problem to be solved. The meanings of parameters defined in this file are explained as follows.

db file name: this line defines the name of the .db file that contains the 3-D slider model. The program will load the model according to the file name defined here. You can use any valid names for your model **other than *CMLTFC*** since this name is reserved for the output .db file of the program. **Do not include the file extension (.db) on this line.**

Thermal model - model type: this line defines the type of thermal models to be used to describe the heat transfer on the air bearing surface. Currently, two thermal models are provided in the TFC code.

***1*:** Heat transfer model proposed by Zhang et. al. in [16] is used.

***2*:** Heat transfer model proposed by Chen et. al. in [19] is used.

The difference between these two models is mainly in the definition of the mean free path of air molecules in the air bearing. Please refer to the two references listed above for more details.

ANSYS model - unit:

1: MKS units are used

2: μMKSV units are used

Refer to ANSYS Coupled-Field Guide [29] to see the specific units used in each unit system.

ANSYS model - orient: this parameter defines the orientation of the model. **Currently, it should always be set to *1*.**

ANSYS model - pad1, pad2: area number of the heater pads. VOLT constraints are applied on these two areas using the ANSYS command *DA*.

ANSYS model - refTemp: the reference temperature of materials used in the thermal strain calculations in ANSYS. To be consistent with *run.dat*, the unit is set to be ^{o}C.

Heater - power: power applied to the heater in mW.

Heater - res: heater resistance in ohm. The voltage is calculated using $(res \cdot power)^{0.5}$ and applied on *pad1*. Accordingly, *0* is applied on *pad 2*.

Mapping - xmin, xmax, ymin, ymax: these four parameters define an area on the air bearing surface on which you apply the deformation calculated from ANSYS to modify the shape of the ABS. Using these parameters, you are allowed to modify a portion of the ABS where the protrusion profile caused by heating has significant effects on the slider's flying-attitude. The following example shows how to use this set of parameters.

For a *0.85mm×0.7mm* slider, suppose the desired mapping area is *0.2mm×0.3mm,* and it is located at the trailing edge center as shown in Figure A.4, Then, *xmin=(0.85-0.2)/0.85=0.76*, which is the x-coordinate of the left edge of this area normalized by the slider's length. Similarly, *xmax=0.85/0.85=1*, which is the x-coordinate of the right edge of this area normalized by the slider's length; *ymin=0.2/0.7=0.29*, which is the y-coordinate of the inner edge of this area normalized by the slider's width; *ymax=(0.2+0.3)/0.7=0.71*, which is the y-coordinate of the outer edge of this area normalized by the slider's width.

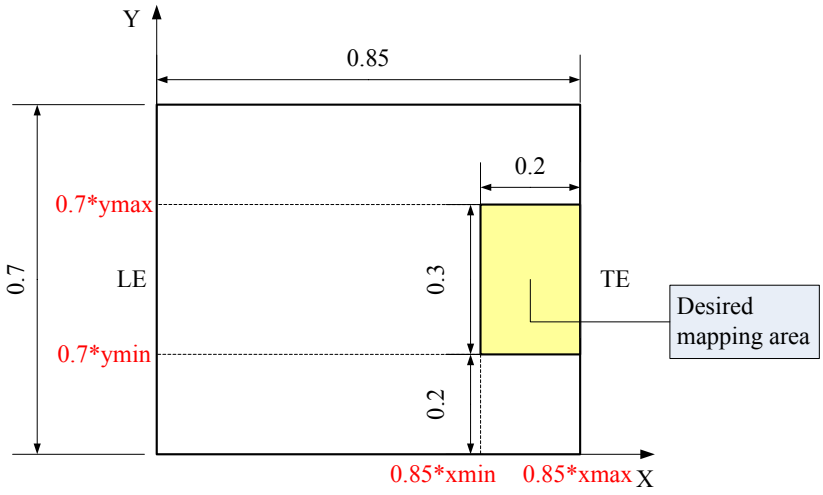

Figure A.4 Definition of *xmin, xmax, ymin,* and *ymax*

Mapping - nx, ny: these two parameters define the density of the grid in the mapping area. *nx* is the total number of grid points in the mapping area along the x-axis, *ny* is the total number of grid points in the mapping area along the y-axis. Once *nx* and *ny* are defined, a uniform rectangular grid will be imposed onto the mapping area. The solved displacements *UZ* on the nodes in the FE model are linearly interpolated to obtain the displacements on this uniform rectangular grid, as shown in Figure A.5.

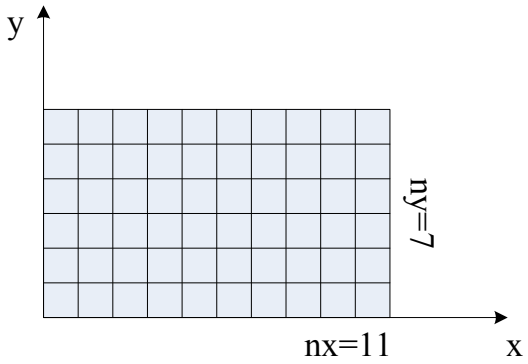

Figure A.5 Uniform grid to map UZ to

Constraints - backfixed: this parameters defines whether or not to apply the back-fixed structural constraints for the structural analysis in ANSYS.

0: No structural constraints will be applied by the program. In this case, you need to define your own structural constraints in the **.db* file. The program will use this set of constraints for structural analysis.

1: A set of structural constraints as shown in Figure A.6 are to be applied on the FE model for structural analysis. The two corners at the leading edge on the back of the slider will be fixed. The back of the slider will be constrained in the height direction. The deformation added to the ABS will be the original displacement at each grid point minus

the minimum displacement in the mapping area. This option is suitable for models without any structural constraints.

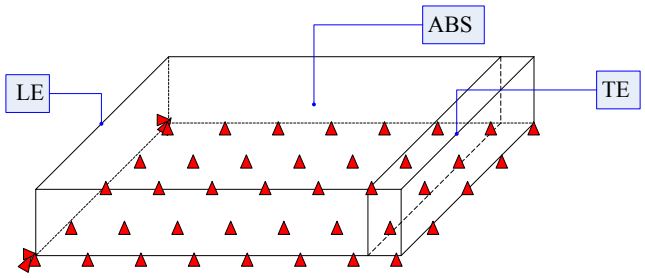

Figure A.6 Back-fixed constraints

Loads – pres: determines whether or not to apply the air bearing pressure as pressure loads in the FE model.

0: No pressure loads are applied.

1: The air bearing pressure calculated by the quick4 solver will be applied to the air bearing surface in the FE model as pressure loads. In this case, the deformation caused by the air bearing pressure is accounted for in the structural analysis.

Cooling - back: a uniform convection coefficient with the value defined here will be applied at the back of the slider in the FE model.

Cooling – side: a uniform convection coefficient with the value defined here will be applied at the four sides of the slider in the FE model.

Convergence – criterion: You can choose nominal flying-height or either of the flying-heights of four interested points as the criterion for convergence. When the specified flying-height calculated from two iterations has a difference less than or equal to the parameter *convergence-limit*, the program will have converged and will exit.

0: nominal flying-height is chosen as the criterion

1: flying-height of the first interested point is chosen as the criterion

2: flying-height of the second interested point is chosen as the criterion

3: flying-height of the third interested point is chosen as the criterion

4: flying-height of the fourth interested point is chosen as the criterion

Convergence – limit: When the flying-height specified by *convergence –criterion* calculated from two iterations has a difference less than or equal to this value, the program will have converged and will exit. The unit for this parameter is *nm*.

Convergence – Max Num. of Iteration: When the total number of iterations is greater than this value, the program will exit regardless of convergence.

air parameters – Kair: This parameter defines thermal conductivity of the air bearing used in the heat transfer coefficient calculations. It applies when *use_standard_air* defined in *run.dat* is set to be 0. The unit is *W/(m·K)*.

air parameters – gamma: This parameter defines specific heat ratio of the air bearing used in heat transfer coefficient calculations. It applies when *use_standard_air* defined in *run.dat* is set to be 0.

air parameters – Pr: This parameter defines Prandtl number of the air bearing used in heat transfer coefficient calculations. It applies when *use_standard_air* defined in *run.dat* is set to be 0.

air parameters – sigma_T: This parameter defines the thermal accommodation coefficient used in heat transfer coefficient calculations. It applies when *use_standard_air* defined in *run.dat* is set to be 0.

2. rail.dat

This file contains information of the air bearing geometry. Refer to the *CMLair User's Manual* for a detailed description of this file. *Rail.dat* can be directly generated from the *CMLair* user interface. **The overall size (length and width) of the air bearing design should match with the size of the FE model built in ANSYS.**

3. run.dat

This file contains information on the suspension load, initial flying-attitudes, radii, etc. Refer to *CMLair User Manual* for a detailed description of this file [128]. Although run.dat allows multiple radii, altitudes and RPMs, only the first case defined in *run.dat* will be used for TFC calculations. The temperature and pressure defined in *run.dat* are used as ambient temperature and pressure in the TFC simulation. *Run.dat* can be directly generated from *CMLair* user interface.

In most cases, *rail.dat* and *run.dat* contain all information necessary for the quick4 solver. However, extra input files may be needed under certain circumstances. For example, if the *ioldg* option is set to be 1, *x.dat* and *y.dat* will also be needed as input files. **Since the CML TFC code incorporates the quick4 solver within, make sure you have all requested files by quick4 as input files.**

4. *.db

This is a database file created in ANSYS defining the slider's geometry. Do not name it as ***CMLTFC.db*** so that it won't be overwritten by the output files of this program. Certain requirements should be satisfied for the CML TFC code to be compatible.

(1) The model contains a block-shaped slider. **The overall size of the model (length and width) should match with the size of the air bearing design.**

(2) The material properties are well defined for the steady-state electro-thermal-structural analysis.

(3) The model is oriented as shown in Figure A.7 **in the global Cartesian coordinate system**, i.e., the ABS is oriented upward along the z-axis, and, the slider length direction should be arranged along the x-axis, with the x-coordinate increasing from the leading edge to the trailing edge.

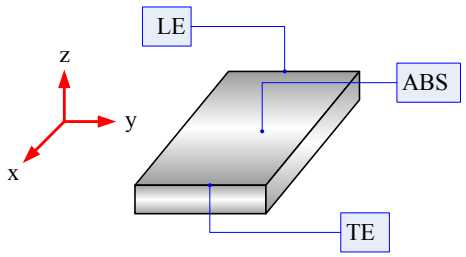

Figure A.7 Required orientation of the FE model

(4) The model should be meshed. A 3-step sequential coupled-field analysis is executed (refer to Fig. 8) in ANSYS, hence, the degrees of freedom (DOFs) of every element type are modified by calling ***KEYOPT*** at the beginning of each stage. The allowed element types include: (i) coupled-field elements: SOLID5, SOLID98; (ii) contact elements: TARGE170, CONTA173, CONTA174, CONTA175. The element types listed above are dealt with according to their definitions of key options.

For most air bearing designs, the heat transfer coefficient on the ABS may vary sharply in a small area, especially at the trailing edge. A properly meshed model is essential for a successful solution in ANSYS.

A.2.3 Program files

1. *SolFHMag.mac*

This macro serves as the main program for the CML TFC code. It first exits the current ANSYS processor, and starts a new job titled CMLTFC. This macro iteratively calls *quick.exe* and the ANSYS coupled-field analysis defined in *SolDeformMag.mac*. It also decides when to exit the solving process. The flowchart of this macro is shown in Figure A.8.

2. *quick.exe*

This compiled executable file solves for the stead-state flying attitude of a slider with a certain ABS design. It is essentially the quick4 solver of CMLair. Besides the standard output files of the quick4 solver, *quick.exe* also creates a formatted file containing the film coefficients across the air bearing surface, which is ready to be imported and loaded into the FE model.

3. *SolDeormMag.mac*

This macro defines a coupled-field analysis in ANSYS using the sequential method. Basically, it starts by applying voltages across the heater pads and calculates the Joule heating, then it carries out a thermal analysis to obtain the temperature over the slider body, and it ends up with a structural analysis for the deformation of the slider body. It also does a linear interpolation to convert the solved *UZ* on the finite element mesh onto a quick-solver-accepted rectangular grid. The details of this macro and essential commands used to apply the loads and constraints are briefly described in Figure A.9.

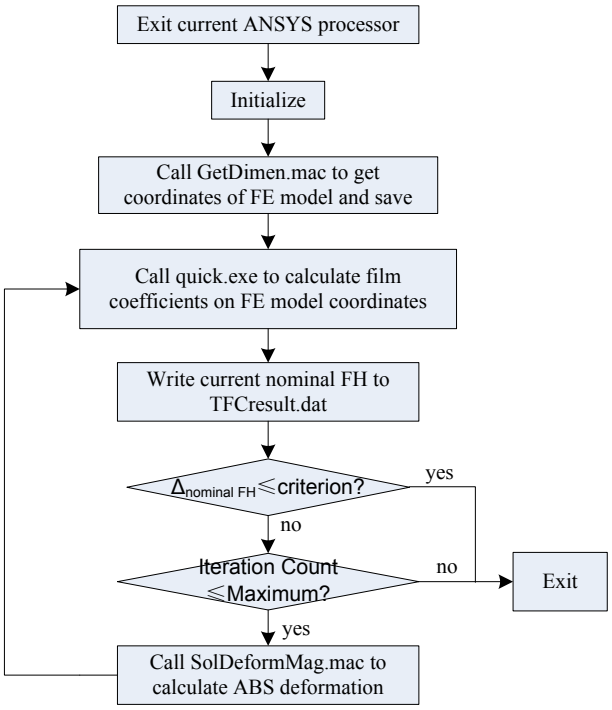

Figure A.8 Flowchart for *SolFHMag.mac*

4. GetDimen.mac

This macro is called by *SolFHMag.mac* at the beginning of the program to obtain the coordinate definitions in the FE model so that *quick.exe* is able to produce the film coefficients on consistent coordinates. You don't need to call this macro directly.

5. ModRefTemp.mac

This macro is called by *SolDeformMag.mac* at the beginning of the coupled-field analysis to modify the reference temperature used to calculate the thermal strains. It is to make sure the reference temperature of each material is consistent with the value defined in *TFCrun.dat*. You don't need to call this macro directly.

6. SwitchElemKoptEh.mac

This macro is called by *SolDeformMag.mac* at the beginning of each stage of the coupled-field analysis. It is to make sure the elements have the right DOFs at each stage of the analysis.

A.2.4 Output files

1. Output files from *quick.exe*

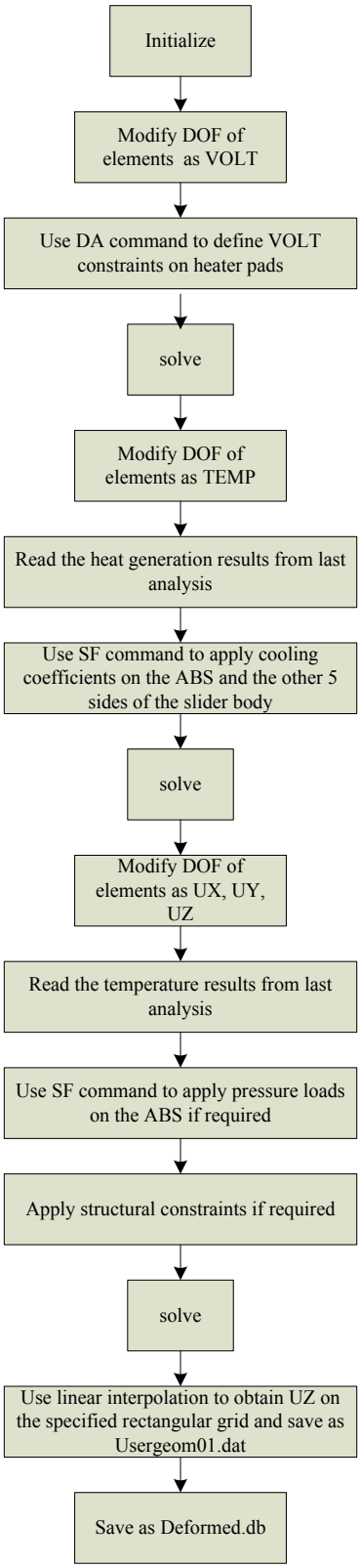

Figure A.9 Flowchart of *SolDeformMag.mac*

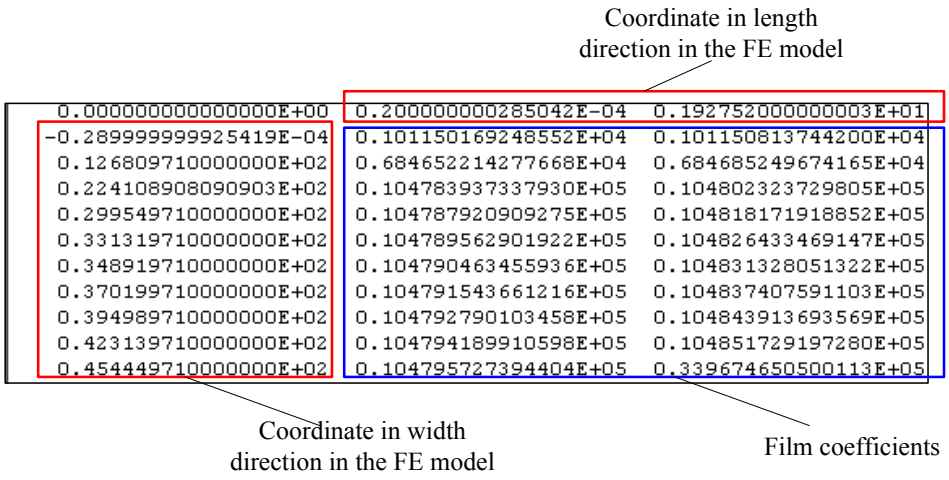

Figure A.10 Sample *FilmCoefficient01.dat*

quick.exe produces all of the standard output files of the CMLair quick4 solver, such as *result.dat, press01.dat,* etc. For information contained in these files, refer to the user's manual for *CMLair* [128]. In addition, the file named *FilmCoefficient01.dat* tabulates the air bearing cooling coefficients applied into the FE model. Figure A.10 gives a sample of this file. The first row of *FilmCoefficient01.dat* gives the coordinates in the FE model along the slider's length direction, and the first column lists the coordinates in the FE model along the slider's width direction.

2. *CMLTFC.db*

This file is the originally input **.db* file with all loads applied and solution saved. Therefore, you can obtain all post-processing results provided by ANSYS through this file, including the displacements, temperature, stress, heat flux, etc.

3. *TFCresult.dat*

This file contains information regarding the TFC iterations. **It is updated at the end of each TFC iteration.** You can access this file throughout the running process to learn the progress of the solution. The file is comprised of two parts: information of the converging process and a summary of results, as shown in Figure A.11. The first part lists the nominal FH calculated from iterations that are finished. The second part contains information about the total number of iterations, the difference in the nominal FH of the last two iterations, whether the solution is considered to be converged and the UZ at the reference point if you set the *Constraints – backfixed* option to be *1*. Here, if the solution converges in the specified maximum iteration number, a message of *solution converged* will be written in this file. Otherwise, a message of *solution not converged* will be given in this file.

4. *CMLTFC.**

CMLTFC is used as the job name for the TFC analysis in ANSYS. Thus ANSYS creates a series of files titled *CMLTFC* containing the essential running information. For example, you may want to check *CMLTFC.err* for any warning and error messages

generated during the TFC analysis in ANSYS. Refer to ANSYS help for details of these files.

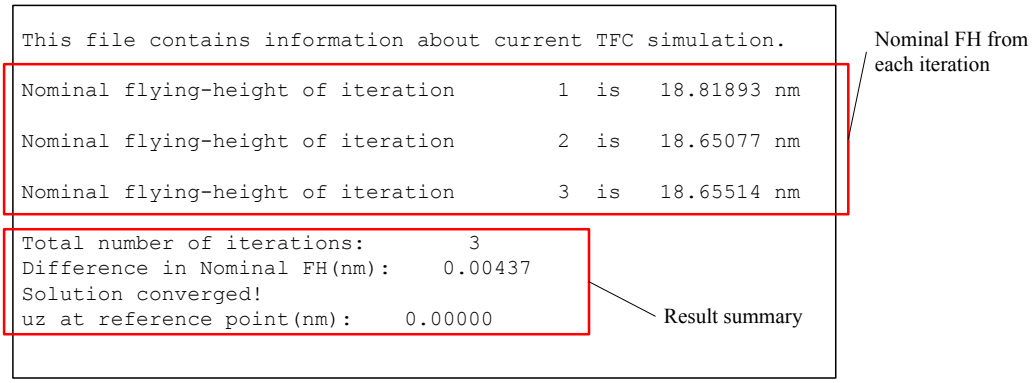

Figure A.11 Sample *TFCresult.dat*

5. *Usergeom01.dat*

This file contains information about the deformation at the mapping area specified in *TFCrun.dat*. It is of the same format as *User Defined Geometry* defined in *CMLair*. Refer to *CMLair User Manual* for the format of this file.

A.3 Installation and Setup

The CMLTFC code is written in APDL (ANSYS Parametric Design Language). It is a series of commands packaged in macros which can be directly called from ANSYS. The execution of CMLTFC code requires no more than executing a macro in ANSYS. The following steps should be taken for setting up a TFC analysis:

(1) Copy all program files to the current working directory of your ANSYS. A complete set of program files includes: *SolFHMag.mac*, *quick.exe, SolDeformMag.mac, GetDimen.mac, ModRefTemp.mac, SwitchElemKoptEh.mac.* The functions of these files and the relationships between them were introduced in Section A.2.3**.**

(2) Copy all input files to the current working directory of your ANSYS. Necessary input files are stated in Section A.2.2.

(3) Modify *TFCrun.dat* to define the parameters for the TFC analysis. The meanings of all parameters defined in *TFCrun.dat* are stated in Section A.2.2. While modifying the parameters, make sure the format of this file is well maintained so that the program can read this file without difficulties.

(4) Launch your ANSYS to the current ANSYS working directory and run the main program, *SolFHMag.mac*. GUI (Graphic User Interface) operations and commands are provided in ANSYS for running a macro. You can use either of the methods listed below to start a TFC analysis:

(i) Using command lines: type

**USE, SolFHMag.mac*

in the single line input window provided by the ANSYS User Interface.

(ii) Using GUI operations: Go to the utility menu and choose *Macro->Execute macro*. In the edit box for *name of macro to be executed*, type *SolFHMag* and then click *OK*.

(5) All output files are exported to the current ANSYS working directory. Refer to Section A.2.4 for an introduction to the output files. Save these files properly before running a new analysis in the same folder.

A.4 Example TFC analysis

This section contains an example of a TFC analysis with the FE model and ABS design provided in the package. The FE model named MyModel.db only contains the substrate, overcoat and a small block-shaped heater for simplicity. Yet it is effective for illustrating the usage of the CML TFC code.

A.4.1 Running the example

You can run a TFC analysis on the provided design by copying the program files and input files to your ANSYS working directory as shown in section 3. You can keep the settings of the provided *TFCrun.dat* unchanged. In the example *TFCrun.dat,*

(1) The field *db file name* is set to be *MyModel* which is the name for the provided FE model.
(2) The field *unit* is set to be *2*, which means μMKSV units are being used.
(3) Fields *pad1* and *pad2* are set to be *16* and *15*, which means constant voltage constraints will be applied on area *16* and *15*.
(4) The field *RefTemp* is set to be *25*, which is the same as the ambient temperature setting in the *run.dat.* The thermal strain will be calculated with 25^oC as the reference temperature.
(5) The field *power* and *res* are set to be 5 and *5,* respectively, which means a voltage of *0.158v* will be applied on *pad1* and *0v* will be applied on *pad2*.
(6) The mapping parameters set the area for the mapped protrusion to be the last *1/4* in the ABS length and the middle *1/3* in the ABS width. The density of grid points will be 2*01* by *201*.
(7) The field *backfixed* is set to be *1* so that the structural constraints in Fig. 6 are applied. The slider will have no global bending in this case.
(8) The field *pres* is set to be 0, such that the pressure-induced deformation on the air bearing surface is not considered.
(9) The fields *cooling-back* and *cooling-side* are set to be *100,* which means a uniform convection coefficient of $100W/(k{\cdot}m^2)$ will be applied on the other five sides of the slider.
(10) The field *convergence-criterion* is set to be *1* and the field *convergence-limit* is set to be *0.01*. Thus, a difference of less than *0.01nm* in flying-height of the first interested point will be considered as a sign of convergence.
(11) The field *Max. num. of Iteration* is set to be *10*, which means the program will stop when the total of iterations reaches *10*, regardless of convergence.

Values defined in the *air parameters* section are not applied in calculations of heat transfer coefficients since the option *use_standard_air* defined in given *run.dat* is set to be 1, that is, standard air properties are adopted while calculating heat transfer coefficients.

A.4.2 Convergence of the solution

The CML TFC code is tested here with the provided slider design. The solution converges in four cycles. Figure A.12 shows the protrusion profiles from the second, third and fourth iterations. Figure A.13 is the generated *TFCresult.dat*, which shows the convergence of the nominal FH.

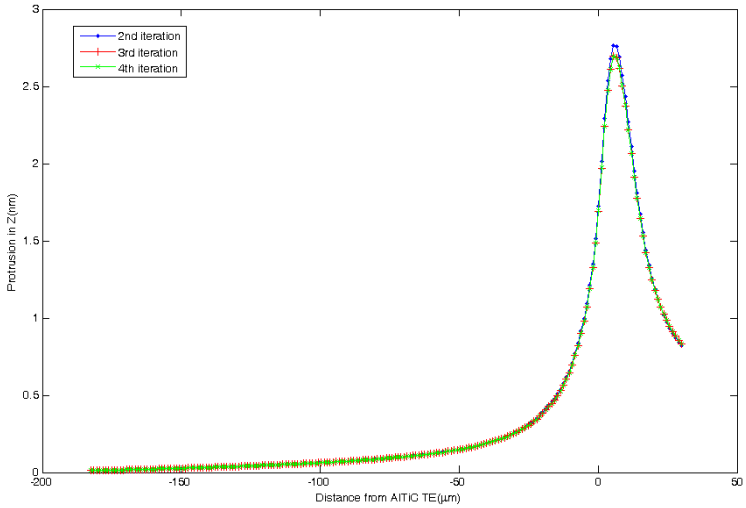

Figure A.12 Convergence of protrusion profile

```
This file contains information about current TFC simulation.

Flying-height of iteration        1  is    2.83886 nm

Flying-height of iteration        2  is    1.02545 nm

Flying-height of iteration        3  is    1.06549 nm

Flying-height of iteration        4  is    1.06453 nm

Total number of iterations:        4
Difference in FH(nm):    0.00096
Solution converged!
```

Figure A.13 TFCresult.dat of the example problem

A.4.3 Plotting the ABS cooling coefficient with FilmCoefficient01.dat

You can use the generated file *FilmCoeffcient01.dat* to plot the applied film coefficient on the air bearing surface (Figure A.14).

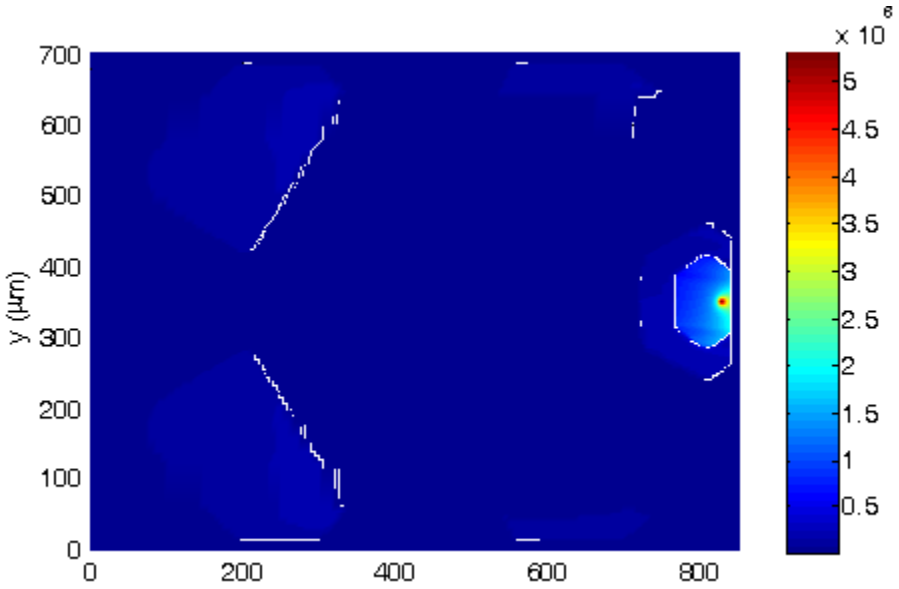

Figure A.14 Display using *Filmcoefficient.txt*

A.4.4 Plotting the protrusion profile with Usergeom01.dat

You can directly use the provided file *Usergeom01.dat* to display the deformation around the transducer (as shown in Figure A.15).

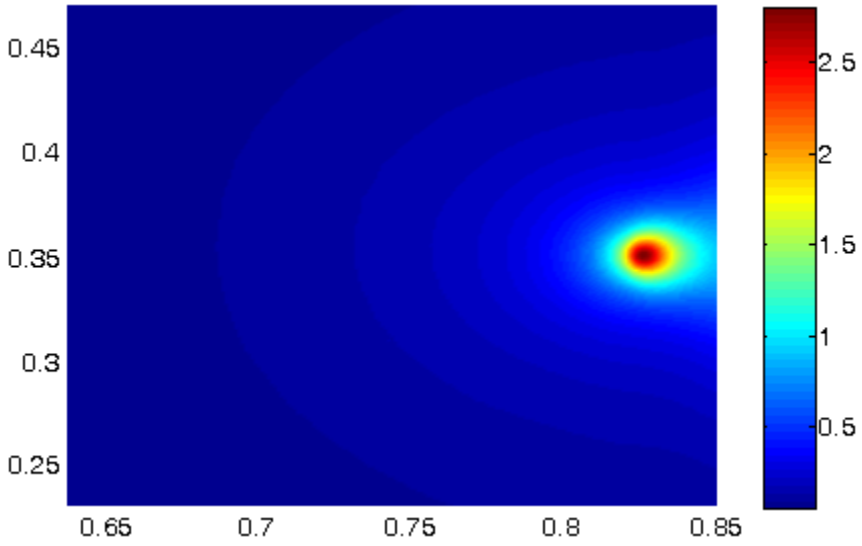

Figure A.15 Plot deformation with *Usergeom01.dat*

A.4.5 Displaying various results with CMLTFC.db

Since ANSYS has a large set of post processing functions, it may be more convenient to view and analyze the results in ANSYS. Figs. 16 and 17 show the body temperature and displacement *UZ* over the slider body created by ANSYS using *CMLTFC.db*.

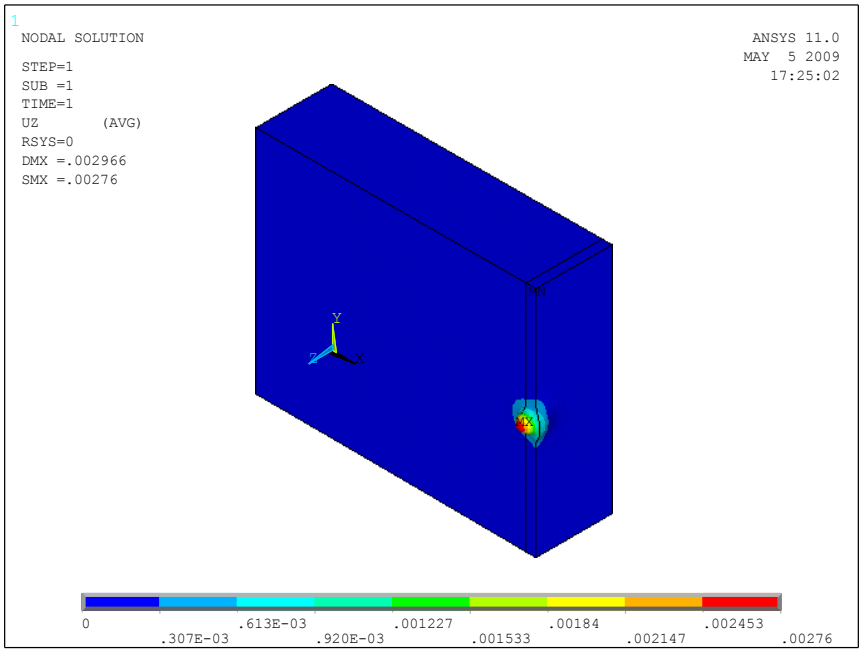

Figure A.16 UZ plot in ANSYS

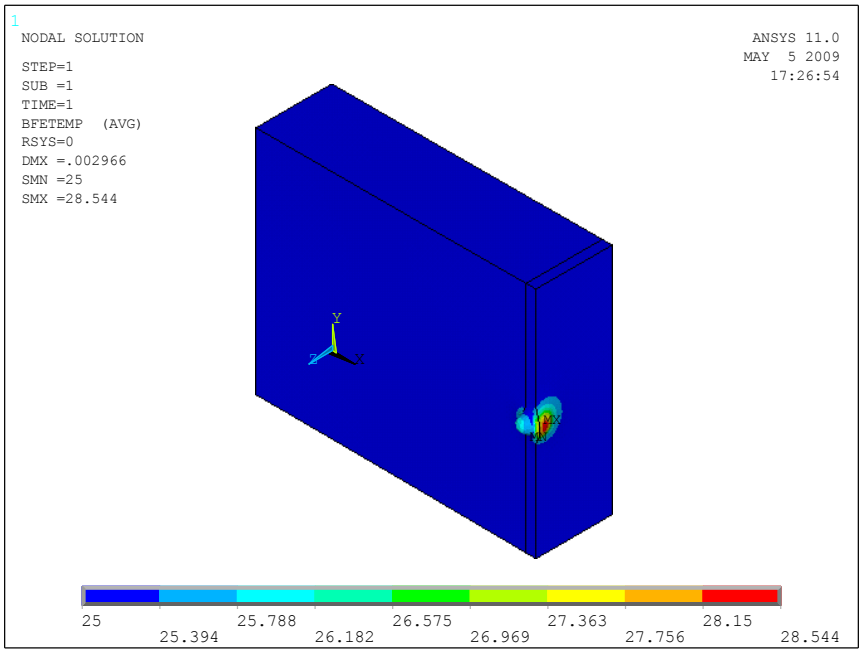

Figure A.17 Temperature distribution plotted by ANSYS

Bibliography

[1] wikipedia. (2007). *hard disk drive*. Available: http://en.wikipedia.org/wiki/Hard_disk_drive

[2] R. Wood, "Future hard disk drive systems," *Journal of Magnetism and Magnetic Materials,* vol. 321, pp. 555-561, Mar 2009.

[3] P. E. K. Dallas W. Meyer, Joseph C. Liu, "Slider with temperature responsive transducer positioning," United States Patent, 1999.

[4] B. E. Schultz. (2007, Thermal flying-height (TFC) Technology in Hitachi Hard Disk Drives. Available: http://www.hitachigst.com/tech/techlib.nsf/techdocs/98EE13311A54CAC886257171005E0F16

[5] H. Li, *et al.*, "Thermal insulator design for optimizing the efficiency of thermal flying height control sliders," *Journal of Applied Physics,* vol. 105, Apr 1 2009.

[6] M. Kurita, *et al.*, "Active flying-height control slider using MEMS thermal actuator," *Microsystem Technologies-Micro-and Nanosystems-Information Storage and Processing Systems,* vol. 12, pp. 369-375, Mar 2006.

[7] K. Miyake, *et al.*, "Optimized design of heaters for flying height a ustment to preserve performance and reliability," *IEEE Transactions on Magnetics,* vol. 43, pp. 2235-2237, Jun 2007.

[8] T. Shiramatsu, *et al.*, "Dynamically Controlled Thermal Flying-Height Control Slider," *IEEE Transactions on Magnetics,* vol. 44, pp. 3695-3697, Nov 2008.

[9] T. Shiramatsu, *et al.*, "Drive-integration of active flying-height control slider with micro thermal actuator," *IEEE Transactions on Magnetics,* vol. 42, pp. 2513-2515, Oct 2006.

[10] M. Suk, *et al.*, "Verification of thermally induced nanometer actuation of magnetic recording transducer to overcome mechanical and magnetic spacing challenges," *IEEE Transactions on Magnetics,* vol. 41, pp. 4350-4352, Nov 2005.

[11] J. Y. Juang and D. B. Bogy, "Air-bearing effects on actuated thermal pole-tip protrusion for hard disk drives," *Journal of Tribology-Transactions of the Asme,* vol. 129, pp. 570-578, Jul 2007.

[12] J. Y. Juang, *et al.*, "Alternate air bearing slider designs for areal density of 1 Tb/in(2)," *IEEE Transactions on Magnetics,* vol. 42, pp. 241-246, Feb 2006.

[13] J. Y. Juang, *et al.*, "Numerical and Experimental Analyses of Nanometer-Scale Flying Height Control of Magnetic Head With Heating Element," *IEEE Transactions on Magnetics,* vol. 44, pp. 3679-3682, Nov 2008.

[14] N. Liu, *et al.*, "Predicting the flying performance of thermal flying-height control sliders in hard disk drives," *Journal of Applied Physics,* vol. 108, Jul 2010.

[15] H. Zheng, *et al.*, "Numerical Simulation of a Thermal Flying Height Control Slider With Dual Heater and Insulator Elements," *IEEE Transactions on Magnetics,* vol. 45, pp. 3628-3631, Oct 2009.

[16] S. Zhang and D. B. Bogy, "A heat transfer model for thermal fluctuations in a thin slider/disk air bearing," *International Journal of Heat and Mass Transfer,* vol. 42, pp. 1791-1800, May 1999.

[17] L. Chen*, et al.*, "Thermal dependence of MR signal on slider flying state," *IEEE Transactions on Magnetics,* vol. 36, pp. 2486-2489, Sep 2000.

[18] H. Zheng*, et al.*, "The Effect of Thermal Radiation on Thermal Flying Height Control Sliders," *IEEE Transactions on Magnetics,* vol. 46, pp. 2376-2378, Jun 2010.

[19] D. Chen*, et al.*, "A phenomenological heat transfer model for the molecular gas lubrication system in hard disk drives," *Journal of Applied Physics,* vol. 105, Apr 15 2009.

[20] O. J. Ruiz and D. B. Bogy, "A Numerical-Simulation of the Head-Disk Assembly in Magnetic Hard Disk Files .1. Component Models," *Journal of Tribology-Transactions of the Asme,* vol. 112, pp. 593-602, Oct 1990.

[21] O. J. Ruiz and D. B. Bogy, "A Numerical-Simulation of the Head-Disk Assembly in Magnetic Hard Disk Files .2. Solution of the Coupled System," *Journal of Tribology-Transactions of the Asme,* vol. 112, pp. 603-613, Oct 1990.

[22] S. Fukui and R. Kaneko, "Analysis of Ultra-Thin Gas Film Lubrication Based on Linearized Boltzmann-Equation .1. Derivation of a Generalized Lubrication Equation Including Thermal Creep Flow," *Journal of Tribology-Transactions of the Asme,* vol. 110, pp. 253-262, Apr 1988.

[23] S. Fukui and R. Kaneko, "A Database for Interpolation of Poiseuille Flow-Rates for High Knudsen Number Lubrication Problems," *Journal of Tribology-Transactions of the Asme,* vol. 112, pp. 78-83, Jan 1990.

[24] F. J. Alexander*, et al.*, "Direct Simulation Monte-Carlo for Thin-Film Bearings," *Physics of Fluids,* vol. 6, pp. 3854-3860, Dec 1994.

[25] S. V. Patankar, *Numerical heater transfer and fluid flow*: McGraw-Ridge, 1980.

[26] S. Lu, "Numerical simulation of slider air bearings," Ph. D., department of mechanical engineering University of California at Berkeley, 1997.

[27] E. Cha and D. B. Bogy, "A Numerical Scheme for Static and Dynamic Simulation of Subambient Pressure Shaped Rail Sliders," *Journal of Tribology-Transactions of the Asme,* vol. 117, pp. 36-46, Jan 1995.

[28] Y. Q. Peng*, et al.*, "Nanoscale effect on ultrathin gas film lubrication in Hard Disk Drive," *Journal of Tribology-Transactions of the Asme,* vol. 126, pp. 347-352, Apr 2004.

[29] ANSYS. (2009). *Coupled-field analysis guide*. Available: www1.ansys.com/customer/content/documentation/120/ans_cou.pdf

[30] R. L. Wallace, "The Reproduction of Magnetically Recorded Signals," *Bell System Technical Journal,* vol. 30, pp. 1145-1173, 1951.

[31] W. K. Shi, *et al.*, "Use of Readback Signal Modulation to Measure Head Disk Spacing Variations in Magnetic Disk Files," *IEEE Transactions on Magnetics,* vol. 23, pp. 233-240, Jan 1987.

[32] E. Cha, *et al.*, "Effect of temperature and altitude on flying height," *IEEE Transactions on Magnetics,* vol. 32, pp. 3729-3731, Sep 1996.

[33] B. D. Strom, *et al.*, "Effects of humid air on air-bearing flying height," *IEEE Transactions on Magnetics,* vol. 43, pp. 3301-3304, Jul 2007.

[34] S. Zhang, *et al.*, "Simulating the air bearing pressure and flying height in a humid environment," *Journal of Tribology-Transactions of the Asme,* vol. 130, Jan 2008.

[35] K. Aruga, *et al.*, "A study on positioning error caused by flow induced vibration using helium-filled hard disk drives," *IEEE Transactions on Magnetics,* vol. 43, pp. 3750-3755, Sep 2007.

[36] N. Liu, *et al.*, "Thermal flying-height control sliders in hard disk drives filled with air-helium gas mixtures," *Applied Physics Letters,* vol. 95, Nov 23 2009.

[37] N. Liu, *et al.*, "Thermal Flying-Height Control Sliders in Air-Helium Gas Mixtures," *IEEE Transactions on Magnetics,* vol. 47, pp. 100-104, Jan 2011.

[38] I. Sato, *et al.*, "Characteristics of Heat-Transfer in a Helium-Filled Disk Enclosure," *IEEE Transactions on Components Hybrids and Manufacturing Technology,* vol. 11, pp. 571-575, Dec 1988.

[39] COESA, "U.S. standard atmosphere," ed: U.S. Government Printing Office, 1976.

[40] J. L. Zheng, *et al.*, "Effects of Altitude on Thermal Flying-Height Control Actuation," *Tribology Letters,* vol. 40, pp. 295-299, Dec 2010.

[41] S. Y. Zhang, *et al.*, "Air bearing surface designs in consideration of thermomechanical actuation efficiency," *Journal of Tribology-Transactions of the Asme,* vol. 130, Oct 2008.

[42] J. A. Goff and S. Gratch, "Low-Pressure properties of water from -160 to 212 F," *Transactions of the American Society of Heating and Ventilating Engineers,* vol. 52, pp. 95-122, 1946.

[43] G. A. Bird, *Molecular Gas Dynamics and the Direct Simulation of Gas Flows*. New York: Oxford Univ. Press, 1994.

[44] J. M. P. B. E. Poling, J. O'Connell, *The Properties of Gases and Liquids*. New York: McGraw-Hill, 2001.

[45] J. Carper, "The CRC Handbook of Chemistry and Physics," *Library Journal,* vol. 124, pp. 192-+, Jun 1 1999.

[46] E. W. Lemmon, *et al.*, "Thermodynamic properties of air and mixtures of nitrogen, argon, and oxygen from 60 to 2000 K at pressures to 2000 MPa," *Journal of Physical and Chemical Reference Data,* vol. 29, pp. 331-385, May-Jun 2000.

[47] S. N. Piramanayagam, "Perpendicular recording media for hard disk drives," *Journal of Applied Physics,* vol. 102, Jul 1 2007.

[48] I. R. McFadyen, *et al.*, "State-of-the-art magnetic hard disk drives," *Mrs Bulletin,* vol. 31, pp. 379-383, May 2006.

[49] B. Marchon and T. Olson, "Magnetic Spacing Trends: From LMR to PMR and Beyond," *IEEE Transactions on Magnetics,* vol. 45, pp. 3608-3611, Oct 2009.

[50] R. Wood, "The feasibility of magnetic recording at 1 Terabit per square inch," *IEEE Transactions on Magnetics,* vol. 36, pp. 36-42, Jan 2000.

[51] D. Weller and A. Moser, "Thermal effect limits in ultrahigh-density magnetic recording," *IEEE Transactions on Magnetics,* vol. 35, pp. 4423-4439, Nov 1999.

[52] A. Khurshudov and R. J. Waltman, "Tribology challenges of modem magnetic hard disk drives," *Wear,* vol. 251, pp. 1124-1132, Oct 2001.

[53] L. Wu and D. B. Bogy, "Effect of the intermolecular forces on the flying attitude of sub-5 NM flying height air bearing sliders in hard disk drives," *Journal of Tribology-Transactions of the Asme,* vol. 124, pp. 562-567, Jul 2002.

[54] B. H. Thornton and D. B. Bogy, "Nonlinear aspects of air-bearing modeling and dynamic spacing modulation in sub-5-nm air bearings for hard disk drives," *IEEE Transactions on Magnetics,* vol. 39, pp. 722-728, Mar 2003.

[55] D. B. Bogy, *et al.*, "Some tribology and mechanics issues for 100-Gb/in(2) hard disk drive," *IEEE Transactions on Magnetics,* vol. 38, pp. 1879-1885, Sep 2002.

[56] R. Ambekar, *et al.*, "Experimental and numerical investigation of dynamic instability in the head disk interface at proximity," *Journal of Tribology-Transactions of the Asme,* vol. 127, pp. 530-536, Jul 2005.

[57] V. Gupta and D. B. Bogy, "Dynamics of sub-5-nm air-bearing sliders in the presence of electrostatic and intermolecular forces at the head-disk interface," *IEEE Transactions on Magnetics,* vol. 41, pp. 610-615, Feb 2005.

[58] V. Gupta and D. B. Bogy, "Effect of intermolecular forces on the static and dynamic performance of air bearing sliders: Part I - Effect of initial excitations and slider form factor on the stability," *Journal of Tribology-Transactions of the Asme,* vol. 128, pp. 197-202, Jan 2006.

[59] V. Gupta and D. B. Bogy, "Effect of intermolecular forces on the static and dynamic performance of air bearing sliders: Part II - Dependence of the stability on hamaker constant, suspension preload and pitch angle," *Journal of Tribology-Transactions of the Asme,* vol. 128, pp. 203-208, Jan 2006.

[60] V. Gupta and D. B. Bogy, "Optimal slider-disk surface topography for head-disk interface stability in hard disk drives," *IEEE Transactions on Magnetics,* vol. 44, pp. 138-144, Jan 2008.

[61] J. L. Zheng and D. B. Bogy, "Investigation of Flying-Height Stability of Thermal Fly-Height Control Sliders in Lubricant or Solid Contact with Roughness," *Tribology Letters,* vol. 38, pp. 283-289, Jun 2010.

[62] B. H. Thornton and D. B. Bogy, "Head-disk interface dynamic instability due to intermolecular forces," *IEEE Transactions on Magnetics,* vol. 39, pp. 2420-2422, Sep 2003.

[63] N. Tagawa*, et al.*, "Effects of molecularly thin liquid lubricant films on slider hysteresis behavior in hard disk drives," *Journal of Tribology-Transactions of the Asme,* vol. 129, pp. 579-585, Jul 2007.

[64] R. P. Ambekar and D. B. Bogy, "Effect of slider lubricant pickup on stability at the head-disk interface," *IEEE Transactions on Magnetics,* vol. 41, pp. 3028-3030, Oct 2005.

[65] K. Ono*, et al.*, "Experimental and analytical study of bouncing vibrations of a flying head slider in a near-contact regime," *Journal of Tribology-Transactions of the Asme,* vol. 127, pp. 376-386, Apr 2005.

[66] K. Ono and M. Yamane, "Improved Analysis of Unstable Bouncing Vibration and Stabilizing Design of Flying Head Slider in Near-Contact Region (vol 129, pg 65, 2007)," *Journal of Tribology-Transactions of the Asme,* vol. 131, Jul 2009.

[67] K. Ono and M. Yamane, "Improved analysis of unstable bouncing vibration and stabilizing design of flying head slider in near-contact region," *Journal of Tribology-Transactions of the Asme,* vol. 129, pp. 65-74, Jan 2007.

[68] Y. Shimizu*, et al.*, "Study of a spherical-pad head slider for stable low-clearance recording in near-contact regime," *Tribology Letters,* vol. 30, pp. 161-167, Jun 2008.

[69] A. Y. Suh*, et al.*, "Adhesion and friction evaluation of textured slider surfaces in ultra-low flying head-disk interfaces," *Tribology Letters,* vol. 17, pp. 739-749, Nov 2004.

[70] A. Y. Suh and A. A. Polycarpou, "Adhesive contact modeling for sub-5-nm ultralow flying magnetic storage head-disk interfaces including roughness effects," *Journal of Applied Physics,* vol. 97, May 15 2005.

[71] A. I. Vakis*, et al.*, "Dynamic Head-Disk Interface Instabilities With Friction for Light Contact (Surfing) Recording," *IEEE Transactions on Magnetics,* vol. 45, pp. 4966-4971, Nov 2009.

[72] A. I. Vakis and A. A. Polycarpou, "Head-disk interface nanotribology for Tbit/inch(2) recording densities: near-contact and contact recording," *Journal of Physics D-Applied Physics,* vol. 43, Jun 9 2010.

[73] A. I. Vakis and A. A. Polycarpou, "Optimization of thermal fly-height control slider geometry for Tbit/in(2) recording," *Microsystem Technologies-Micro-and Nanosystems-Information Storage and Processing Systems,* vol. 16, pp. 1021-1034, Jun 2010.

[74] A. Y. Suh and A. A. Polycarpou, "Dynamic Adhesive Instability of Sub-Five Nanometer Head-Disk Interfaces," in *the 13th Mediterranean Conference on Control and Automation*, 2005, pp. 139-146.

[75] W. Hua, *et al.*, "Probability model and its application on the interaction of nano-spaced slider/disk interface," *Ieice Transactions on Electronics,* vol. E82c, pp. 2139-2147, Dec 1999.

[76] W. Hua, *et al.*, "Nanoscale roughness contact in a slider-disk interface," *Nanotechnology,* vol. 20, Jul 15 2009.

[77] W. Hua, *et al.*, "Energy Analysis on Flying Stability of Sub-5-nm Air Bearing Slider," *IEEE Transactions on Magnetics,* vol. 45, pp. 4998-5001, Nov 2009.

[78] S. K. Yu, *et al.*, "Dynamic Stability Analysis for Surfing Head-Disk Interface," *IEEE Transactions on Magnetics,* vol. 45, pp. 4979-4983, Nov 2009.

[79] D. T. F. P. Bowden, *the Friction and Lubrication of Solids*: Oxford University Press, 1950.

[80] B. V. Deryagin and V. V. Karasev, "Study of Boundary Viscosity of Organic Liquids by the Blow-Off Method," *Uspekhi Khimii,* vol. 57, pp. 1110-1130, 1988.

[81] H. M. Stanley, *et al.*, "Adhesion of Contacting Rough Surfaces in the Presence of Subboundary Lubrication," *Journal of Tribology-Transactions of the Asme,* vol. 112, pp. 98-104, Jan 1990.

[82] D. Chen and D. B. Bogy, "Intermolecular force and surface roughness models for air bearing simulations for sub-5 nm flying height sliders," *Microsystem Technologies-Micro-and Nanosystems-Information Storage and Processing Systems,* vol. 13, pp. 1211-1217, May 2007.

[83] D. Chen, "Partial-Contact Head Disk Interface for Ultrahigh Density Magnetic Recording," Ph. D., Mechanical Engineering, University of California at Berkeley, 2008.

[84] J. A. Greenwood and J. B. P. Williamson, "Contact of Nominally Flat Surfaces," *Proceedings of the Royal Society of London Series a-Mathematical and Physical Sciences,* vol. 295, pp. 300-&, 1966.

[85] J. A. Greenwood and J. H. Tripp, "The contact of two nominally flat rough surfaces," *Proc. Instn. Mech. Engrs.,* vol. 185, pp. 625-633, 1971.

[86] J. I. Mccool, "Relating Profile Instrument Measurements to the Functional Performance of Rough Surfaces," *Journal of Tribology-Transactions of the Asme,* vol. 109, pp. 264-270, Apr 1987.

[87] W. R. Chang, *et al.*, "An Elastic-Plastic Model for the Contact of Rough Surfaces," *Journal of Tribology-Transactions of the Asme,* vol. 109, pp. 257-263, Apr 1987.

[88] W. R. Chang, *et al.*, "Adhesion Model for Metallic Rough Surfaces," *Journal of Tribology-Transactions of the Asme,* vol. 110, pp. 50-56, Jan 1988.

[89] W. R. Chang, *et al.*, "Static Friction Coefficient Model for Metallic Rough Surfaces," *Journal of Tribology-Transactions of the Asme,* vol. 110, pp. 57-63, Jan 1988.

[90] J. N. Israelachvili, *Intermolecular and surface forces*, 3rd ed. Burlington, MA: Academic Press, 2011.

[91] M. D. Pashley, "Further Consideration of the Dmt Model for Elastic Contact," *Colloids and Surfaces,* vol. 12, pp. 69-77, 1984.

[92] Z. Feng*, et al.*, "A study of electrical charge at head-disk interface," *Tribology Letters,* vol. 18, pp. 53-57, Jan 2005.

[93] B. E. Knigge*, et al.*, "Influence of contact potential on slider-disk spacing: Simulation and experiment," *IEEE Transactions on Magnetics,* vol. 40, pp. 3165-3167, Jul 2004.

[94] Y. Hu, "Head-disk-suspension dynamics," Ph.D., Mechanical Engineering, University of California at Berkeley, 1996.

[95] L. Z. Su*, et al.*, "Tribological and Dynamic Study of Head Disk Interface at Sub-1-nm Clearance," *IEEE Transactions on Magnetics,* vol. 47, pp. 111-116, Jan 2011.

[96] Q. H. Zeng*, et al.*, "An Experimental and Simulation Study of Touchdown Dynamics," *IEEE Transactions on Magnetics,* vol. 47, pp. 3433-3436, Oct 2011.

[97] J. Zheng and D. B. Bogy, "Dynamic instability of thermal-flying-height-control sliders at touchdown," in *the 21th ASME Annual Conference on Information Storage and Processing systems*, Santa Clara University, Santa Clara, California, USA, 2011.

[98] V. Gupta, "Air bearing slider dynamics and stability in hard disk drives," Ph.D., Mechanical Engineering, University of California at Berkeley, Berkeley, 2007.

[99] N. M. Newmark, *A method of computation for structural dynamics*. Urbana,: University of Illinois, 1959.

[100] D. Chen and D. B. Bogy, "Dynamics of partial contact head disk interface," *IEEE Transactions on Magnetics,* vol. 43, pp. 2220-2222, Jun 2007.

[101] A. Khurshudov and P. Ivett, "Head-disk contact detection in the hard-disk drives," *Wear,* vol. 255, pp. 1314-1322, Aug-Sep 2003.

[102] J. Xu and R. Tsuchiyama, "Ultra-low-flying-height design from the viewpoint of contact vibration," *Tribology International,* vol. 36, pp. 459-466, Apr-Jun 2003.

[103] C. M. Mate*, et al.*, "Lubricant-Induced Spacing Increases at Slider-Disk Interfaces in Disk Drives," *Tribology Letters,* vol. 37, pp. 581-590, Mar 2010.

[104] B. Knigge*, et al.*, "Friction, heat, and slider dynamics during thermal protrusion touchdown," *IEEE Transactions on Magnetics,* vol. 42, pp. 2510-2512, Oct 2006.

[105] N. Li*, et al.*, "Experimental Study of Head-Disk Interface Flyability and Durability at Sub-1-nm Clearance," *IEEE Transactions on Magnetics,* vol. 45, pp. 3624-3627, Oct 2009.

[106] B. Liu*, et al.*, "Towards fly- and lubricant-contact recording," *Journal of Magnetism and Magnetic Materials,* vol. 320, pp. 3183-3188, Nov 2008.

[107] Z. F. Li, *et al.*, "Study of head-disk interference at low-flying height," *IEEE Transactions on Magnetics,* vol. 39, pp. 2462-2464, Sep 2003.

[108] S. C. Lee and A. A. Polycarpou, "Microtribodynamics of pseudo-contacting head-disk interfaces intended for 1 Tbit/in(2)," *IEEE Transactions on Magnetics,* vol. 41, pp. 812-818, Feb 2005.

[109] W. Hua, *et al.*, "Contact recording review," *Microsystem Technologies-Micro-and Nanosystems-Information Storage and Processing Systems,* vol. 16, pp. 493-503, Apr 2010.

[110] F. E. Talke, "A review of 'contact recording' technologies," *Wear,* vol. 207, pp. 118-121, Jun 1997.

[111] S. V. Canchi and D. B. Bogy, "Slider Dynamics in the Lubricant-Contact Regime," *IEEE Transactions on Magnetics,* vol. 46, pp. 764-769, Mar 2010.

[112] S. V. Canchi and D. B. Bogy, "Thermal Fly-Height Control Slider Instability and Dynamics at Touchdown: Explanations Using Nonlinear Systems Theory," *Journal of Tribology-Transactions of the Asme,* vol. 133, Apr 2011.

[113] B. Liu, *et al.*, "Lube-Surfing Recording and Its Feasibility Exploration," *IEEE Transactions on Magnetics,* vol. 45, pp. 899-904, Feb 2009.

[114] Y. Shimizu, *et al.*, "Experimental study on slider dynamics during touchdown by using thermal flying-height control," *Microsystem Technologies-Micro-and Nanosystems-Information Storage and Processing Systems,* vol. 17, pp. 897-902, Jun 2011.

[115] G. Sheng and J. F. Xu, "A parameter identification method for thermal flying-height control sliders," *Microsystem Technologies-Micro-and Nanosystems-Information Storage and Processing Systems,* vol. 17, pp. 1409-1415, Sep 2011.

[116] D. Chen and D. B. Bogy, "Numerical Investigation of Bouncing Vibrations of an Air Bearing Slider in Near or Partial Contact," *Journal of Tribology-Transactions of the Asme,* vol. 132, Jan 2010.

[117] R. Ranjan, *et al.*, "Laser Texturing for Low-Flying-Height Media," *Journal of Applied Physics,* vol. 69, pp. 5745-5747, Apr 15 1991.

[118] R. Pit, *et al.*, "Formation of lubricant "moguls" at the head/disk interface," *Tribology Letters,* vol. 10, pp. 133-142, Apr 2001.

[119] F. E. Talke, "On tribological problems in magnetic disk recording technology," *Wear,* vol. 190, pp. 232-238, Dec 1995.

[120] S. C. Lee and A. A. Polycarpou, "Adhesion forces for sub-10 nm flying-height magnetic storage Head Disk Interfaces," *Journal of Tribology-Transactions of the Asme,* vol. 126, pp. 334-341, Apr 2004.

[121] L. Zhou, *et al.*, "Nanometre scale island-type texture with controllable height and area ratio formed by ion-beam etching on hard-disk head sliders," *Nanotechnology,* vol. 10, pp. 363-372, Dec 1999.

[122] P. Baumgart*, et al.*, "A New Laser Texturing Technique for High-Performance Magnetic Disk Drives," *IEEE Transactions on Magnetics,* vol. 31, pp. 2946-2951, Nov 1995.

[123] Q. H. Zeng*, et al.*, "Flyability and flying height modulation measurement of sliders with sub-10 nm flying heights," *IEEE Transactions on Magnetics,* vol. 37, pp. 894-899, Mar 2001.

[124] M. Suk*, et al.*, "Role of Disk Surface-Roughness on Slider Flying Height and Air-Bearing Frequency," *IEEE Transactions on Magnetics,* vol. 26, pp. 2493-2495, Sep 1990.

[125] K. Ono, "NUMERICAL METHOD OF ANALYZING CONTACT MECHANICS BETWEEN A SPHERE AND A FLAT CONSIDERING LENNARD-JONES SURFACE FORCES OF CONTACTING ASPERITIES AND MEAN HEIGHT SURFACES," in *the STLE/ASME 2010 International Joint Tribology Conference*, October 17-20, 2010, San Francisco, California, USA, 2010.

[126] W. Hua*, et al.*, "Thermal protrusion induced air bearing frequency variations," *Microsystem Technologies-Micro-and Nanosystems-Information Storage and Processing Systems,* vol. 17, pp. 891-896, Jun 2011.

[127] J. ZHENG and D. B. Bogy, "Numerical Simulation of Touchdown Dynamics of Thermal-Flying-Height-Control Sliders," presented at the ASME/STLE 2011 International Joint Tribology Conference, Los Angeles, California, USA, 2011.

[128] B. J. Cox and D. B. Bogy, "The CML Air Bearing Design program (CMLAir), Version 7 User Manual," University of California at Berkeley2007.